2023

Combustion Characteristics of Methane, Ethane, Propane, and Butane Blends Under Conditions Relevant of a Dual-Fuel Diesel and Natural Gas Engine

Christopher Joseph Ulishney
West Virginia University

Combustion Characteristics of Methane, Ethane, Propane, and Butane Blends Under Conditions Relevant of a Dual-Fuel Diesel and Natural Gas Engine

Christopher J. Ulishney

Dissertation submitted

to the Benjamin M. Statler College of Engineering and Mineral Resources

at West Virginia University

In partial fulfillment of the requirements for the degree of

Doctor of Philosophy in

Mechanical Engineering

Cosmin Dumitrescu, Ph.D., Chair

Derek Johnson, Ph.D.

Dr. V'yacheslav Akkerman, Ph.D.

Dr. John Hu, Ph.D.

Dr. Mahdi Darzi, Ph.D.

Department of Mechanical and Aerospace Engineering

Morgantown, West Virginia

2023

Keywords: Diesel-Natural Gas Dual-Fuel, Optical Engine, Fuel Composition, Fuel Utilization

Abstract

Combustion Characteristics of Methane, Ethane, Propane, and Butane Blends Under Conditions Relevant of a Dual-Fuel Diesel and Natural Gas Engine

Christopher J. Ulishney

As natural gas production infrastructure is already in place in most of the world and will continue expanding for the foreseeable future, natural gas is an alternative to traditional liquid petroleum fuels in heavy-duty engines. Dedicated natural gas or dual-fuel diesel-natural gas heavy-duty engines are alternatives to diesel-only power generation equipment. One challenge is the large variation in the natural gas composition available for such applications, which is known to significantly affect engine's combustion characteristics and the emissions composition. As the literature on dual-fuel combustion under low load engine operating conditions that use more realistic natural gas mixtures (i.e., mixtures that, in addition of methane (C_1; the most abundant natural gas component), also contain ethane (C_2), propane (C_3), and butane (C_4)) is limited, this study evaluated the combustion characteristics of a variety of C_1-C_4 mixtures using three different experimental platforms: a 4.5-L 4-cylinder heavy-duty production diesel engine modified for dual-fuel diesel-natural gas engine operation, a prototype 1.125-L single-cylinder engine with extended optical access that was based on the same production diesel engine, and a laminar flame burner.

Experiments in the heavy-duty production engine under low load dual-fuel diesel-natural gas operating conditions (6 bar break mean effective pressure at 1000 RPM, 1000 bar diesel injection pressure, and 40% diesel substitution ratio) showed that gas composition affected the diesel fuel ignition delay and combustion phasing, which are known to affect both engine performance and emissions. As in-cylinder pressure correlated with the autoignition temperature of the gaseous mixture, mixtures with higher C_2-C_4 content produced the best engine performance and emissions compared to using 100% C_1, suggesting that the addition of C_2-C_4 content benefits low load dual-fuel combustion. For example, brake specific carbon dioxide and nitrogen oxides emissions reduced up to 6.6% and 20%, respectively. In addition, gas mixtures containing C_3 and C_4 reduced the brake specific carbon dioxide equivalent by up to 50 g/kWh compared to the C_1-only case.

Experiments in the prototype single cylinder optical engine employed imaging diagnostics to better understand the C_1-C_4 effects observed in the production engine experiments. High boost and high intake temperature were used to create in-cylinder conditions similar to those in the production engine at the start of combustion. To enhance the visual differences between the natural gas components, only one component was used at a time instead of a multicomponent mixture as in the production engine experiments, and difficulties in accurately controlling the C_4 flow resulted in using only C_1-C_3. Experiments were performed at similar low load dual fuel operating conditions (~ 6.6 bar indicated mean effective pressure at 1000 RPM, 500 bar diesel injection pressure, and ~ 63% diesel substitution ratio), using both traditional and advanced diesel injection timing (i.e., conventional mixing-controlled compression ignition or MCCI compared to reactivity-controlled compression ignition or RCCI). Natural luminosity data showed that C_3 RCCI had a more advanced combustion phasing despite an increased ignition delay and higher spatially-integrated natural luminosity compared to C_1 RCCI and C_2 RCCI. An earlier premixed combustion and a smaller phasing difference between the apparent heat release and spatially-integrated natural luminosity was seen for MCCI compared to RCCI. The results suggested that the C_1-C_3 content

indeed affected the diesel gas mixing and stratification of the low load dual-fuel operation, hence the differences in engine performance and emissions observed in the production engine experiments. As a result, the findings in this study can be used for modeling the dual-fuel combustion of C_1-C_4 blends and can help industry in utilizing more efficiently natural gas with higher C_2-C_4 content.

Acknowledgements

I would like to thank Dr. Cosmin Dumitrescu for making this work possible and guiding my studies. His continuous personal support has helped me develop in my profession. The Advanced Combustion Laboratory research facility at West Virginia University provided a means of conducting such extensive experiments. I would also like to thank my MS advisor Dr. Derek Johnson for his continued support and sharing of important equipment (most importantly the MKS 2030 FTIR emission analyzer). The material is based upon work funded by the WV Higher Education Policy Commission under grant number HEPC.dsr.18.7. The authors gratefully acknowledge WVU's Center for Innovation in Gas Research and Utilization (CIGRU) , Dr. Hu of the CHE department, and the MAE department for their support (especially Kelsey Crawford, and Dr. Derek Johnson). A special *thank you* to Jinlong Liu and Lorenzo Gasbarro for their contribution on the experimental setup during their time as graduate students at WVU.

Table of Contents

List of Figures

List of Tables

Nomenclature

Definitions / Abbreviations

Acronym	
AFR	Air-Fuel Ratio
ATDC	After Top Dead Center
BSFC	Brake Specific Fuel Consumption
BTDC	Before Top Dead Center
°C	Degrees Celsius
CAD	Crank Angle in Degrees
CFR	Code of Federal Regulation
CH_4 , C_1	Methane
C_2H_6, C_2	Ethane
C_3H_8, C_3	Propane
C_4H_{10}, C_4	Butane
C_5H_{12}, C_5	Pentane
CNG	Compressed Natural Gas
CO	Carbon Monoxide
CO_2	Carbon Dioxide
$CO_{2,eq}$	Carbon Dioxide Equivalent
COV	Coefficient of Variation
CR	Compression Ratio
DI	Direct Injection
ECU	Engine Control Unit
EPA	Environmental Protection Agency
EOI_{NG}	End of Injection Natural Gas
ESR	Energy Substitution Rate
FTIR	Fourier Transform Infrared Spectroscopy Analyzer
g	Grams
g/kW-hr	Grams Per Kilowatt Hour
GHG	Greenhouse Gas
GWP	Global Warming Potential
HC	Hydrocarbon
IMEP	Indicated Mean Effective Pressure
J	Joules
kW	Kilowatts
LFE	Laminar Flow Element
LHV	Lower Heating Value
mm	Millimeter
MBT	Maximum Brake Torque
MJ/kg	Mega Joules per Kilogram
MN	Methane Number
NG	Natural Gas

NMHC	Non-Methane Hydrocarbons
NO_x	Nitrogen Oxides
PFI	Port Fuel Injection
RCCI	Reactivity Controlled Compression Ignition
RPM	Revolutions per Minute
SI	Spark Ignition
SLPM	Standard Liters Per Minute
SOI	Start of Injection
SOI_{DIESEL}	Start of Diesel Injection
TDC	Top Dead Center
THC	Total Hydrocarbon
Variables	
B	Bore
d	diameter
$\dot{E}_{in}$	Fuel Energy Input
K_h	NO_x correction factor
L	Stroke Length
M	Molar Mass
$\dot{m}$	Mass Flow Rate
N	Operating Speed (in RPM)
$\dot{n}_{exh}$	Exhaust Molar Flow Rate
P_b	Brake Power
P_i	Indicated Power
P_{cyl}	Cylinder Pressure
P_{inj}	Injection Pressure
r_c	Geometric Compression Ratio
R	Connecting rod to crank rod length ratio
R_i	Ideal gas constant
S_L	Laminar Flame Speed
T	Temperature
T	Torque
V	Volume
V_c	Clearance Volume
V_d	Displacement Volume
v_i	Component Mole Fraction
x_i	Component Mass Fraction
ϕ	Equivalence Ratio
γ	Gamma
ρ	Density
θ	Crank Angle in Degrees
°	Degrees
$\eta_{th,brake}$	Brake Thermal Efficiency
$\eta_{th,ind}$	Indicated Thermal Efficiency

1 Introduction

1.1 Background

Natural gas (NG) is a prominent energy source utilized in the United States (U.S.) and around the world. The gradual expansion of NG infrastructure increased its availability across the U.S. and decreased its cost [1]. For example, NG has been the dominant energy source for electricity generation since 2015, surpassing coal fired electrical generation [2]. Its low carbon to hydrogen ratio means that NG will release only 55% of the carbon dioxide (CO_2) that an equal energy content of coal would produce [3]. As NG continues to account for an increasing fraction of total energy production, the supply of less demanded ethane, propane, and butane components will also increase.

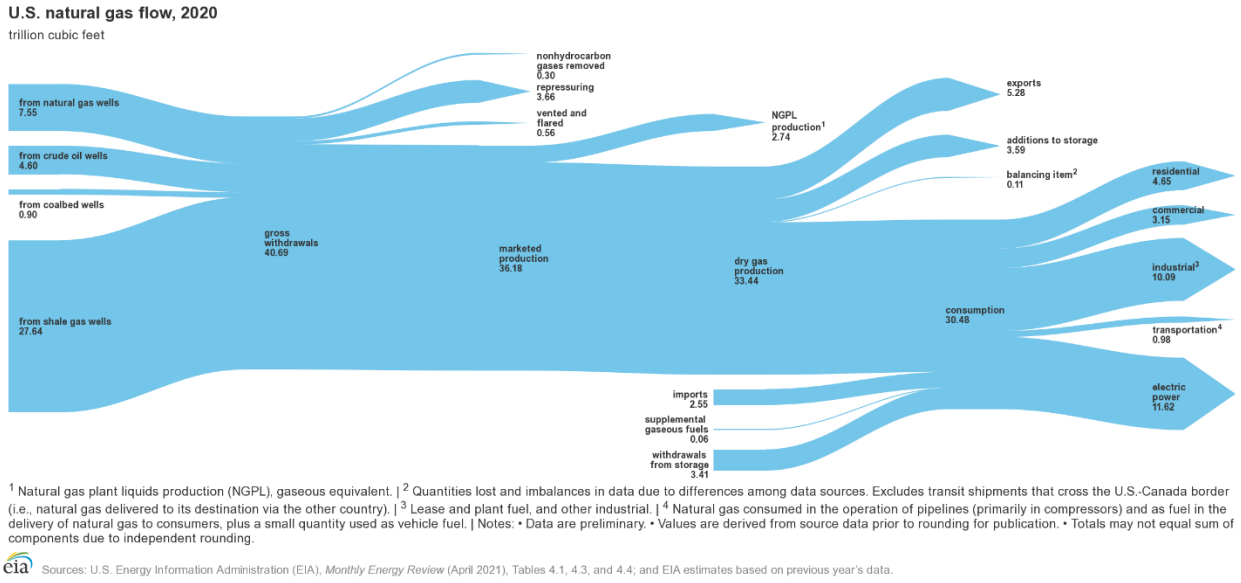

***Figure 1- Natural Gas Production and Usage Pathways** [4]*

Currently, the transportation sector (including pipeline pumping stations) uses a very limited amount of NG, less than double of what is flared during production [4]. With diesel fuel costs reaching an all-time high in 2022 [5], the prospect of using the flared portion in a diesel-NG dual-fuel engine to create power would benefit the producers, local consumers, and the environment.

Pipeline NG is primarily composed of methane (CH_4 or C_1 in this study) with variable amounts of other naturally occurring hydrocarbons such as ethane (C_2H_6 or C_2) or propane (C_3H_8 C_3), plus CO_2, nitrogen (N_2), and other trace gases [6]. The pipeline composition derives from the raw NG,

which, after being pulled from the ground, is processed to remove water, solids, acids, natural gas liquids (NGL) such as C_2, C_3, butane (C_4H_{10} or C_4) and pentane (C_5H_{12} or C_5), and any other undesirable non-hydrocarbon species. The refined gas is then odorized for safety purposes before being distributed to customers for domestic household usage. Pipeline NG is only allowed limited amounts of C_2-C_5 components. Therefore, C_2-C_5 components are typically used in other chemical refining processes but their demand can vary drastically with time and region. Generally, when C_2-C_5 market demand is low, gas companies store the excess until demand increases again. But NG production is continuous and storage space can quickly become an issue. Consequently, gas companies can be forced to flare excess C_2-C_5 when storage reaches maximum capacity. On the other hand, recent oil production and transportation issues have caused large disruptions in diesel fuel supply in the U.S. [7]. A solution to reduce both diesel demand and pollution is to increase the utilization of C_2-C_5 components in diesel applications, such as the partial replacement of the diesel fuel used to power various equipment associated with NG production, filtering, and distribution.

This study is based on the hypothesis that minimally processing of the raw NG would be required at the production site to obtain a C_1-C_4 gas composition that can be safely utilized for power production at the local gas extraction and processing site. This would save on diesel fuel costs as well on the wasted energy exerted for pumping the undesired products off to be flared elsewhere in the case of limited storage. To better understand the C_1-C_4 composition effects on the efficiency and emissions of a power generation device similar to ones used in the gas industry, this study investigated the combustion characteristics of various C_1-C_4 gaseous mixture at engine relevant conditions. Experiments consisted of fundamental flame experiments using gas burners as well as dynamometer testing using conventional (or “base” engine) and optical diesel engines converted to dual-fuel diesel-NG operation. The combination of these different experimental platforms means that the engine performance and emissions measurements from the base engine experiments was complemented by the visualization of in-cylinder combustion phenomena via the optical engine experiment and the measurement of fundamental flame properties via the gas burner experiments. Engine experiments kept constant the total fuel energy of the C_1-C_4 mixtures so any changes in combustion characteristics could be directly attributed to changes in physical and chemical properties of the mixture. A literature review identified as an area of interest for engine development the lower load operating condition, when the dual-fuel engine operation was shown

to be very sensitive to actual NG composition [8]. For example, previous dual-fuel diesel-NG research has highlighted a limitation in the NG substitution rates at lower engine load to a maximum of 40-45% of the total energy, due to unacceptable methane emissions [9]. Methane equivalence ratio (ϕ) at low load and low substitution rates is very low (ϕ = 0.2-0.25), hence the primary flame initialization occurs and is sustained via the autoignition of diesel [10]. The literature review also showed that, with respect to engine out emissions, ultra-lean conditions usually lead to poor methane oxidation and high carbon monoxide (CO) concentrations in the exhaust.

Research on the combustion characteristics of various fuels or fuel mixtures under typical atmospheric conditions is historically significant. For example, the laminar flame speeds of premixed fuels are well documented in literature and are used to predict how a specific fuel would react under engine relevant conditions. Flame speed experiments are mainly conducted in burners, shock tubes, and pressurized combustion vessels. Burner experiments can provide detailed combustion characteristics such as laminar flame speed, diffusion rates, and flame temperature. Experiments in pressurized combustion vessel investigate the effects of fuel composition, temperature, pressure, and equivalence ratio on flame inception and propagation; however, they lack the turbulent environment relevant to in-cylinder engine conditions.

Depending on the specific composition of the NG mixture, the combustion characteristics change under different utilizations. Also, depending on the environmental conditions, C_4-C_5 fractions in the gas may be in a liquid phase before their utilization, which would require specialized fueling methods. Then, the higher hydrogen-to-carbon ratio of methane means that its combustion reduces the carbon release rate compared to traditional gasoline or diesel for the same energy release, making it a desirable fuel source for internal combustion engines (ICE). Methane also exhibits a high knock resistance, allowing it to be used under higher compression ratio (CR), hence higher possible efficiencies. Lean operation allows for reductions in both CO and nitrogen oxides (NO_x) emissions [11-12]. NG combustion also benefits from the low particulate matter concentrations in the exhaust due to the absence of fuel rich pockets and strong carbon bonds [12]. Particulate matter observed under single-fuel NG operation mostly comes from the burning of lubrication oil films on the cylinder wall.

2 Literature Review

2.1 Heavy-Duty IC Engines

Diesel engines dominate the commercial transportation and off-road sector and provide the best fuel conversion efficiencies of modern ICE's [13]. Considering current limitations in renewable energy production, electric vehicle battery production, recycling and recharging infrastructure, and large energy demand at continuous high load operation it is likely that diesel engines will still be used in the foreseeable future.

The engine control unit (ECU) in modern diesel engines monitors the fueling rate based on numerous engine sensors and accurately calculates the amount of fuel needed for optimal operation at any given condition. Modern aftertreatment devices and low-sulfur fuel have greatly lowered the NO_x and oxides of sulfur (SO_x) emission levels. However, the rate of CO_2 emissions from any diesel engine depends solely on the fueling rate. The amount of CO_2 released from diesel engines could be reduced by substituting partially or completely the diesel fuel with NG. This technology is widely referred to as dual-fuel combustion and is especially useful wherever pollution is a major concern. While hydrogen dual-fuel operation is potentially an even cleaner option regarding CO_2 emissions [14], the supply of "green" hydrogen is extremely limited as compared to NG supply.

New technologies such as DFI (Ducted Fuel Injection) diesel engines have shown potential for reducing soot and HC emissions while also keeping NO_x to a low level [15]. The DFI strategy promotes fuel-air premixing to allow for leaner mixtures at the autoignition zones [15]. DFI has been shown to be effective at reducing soot over all load ranges and allows for low soot and NO_x at low load conditions [16]. Ultra-high rail pressure of 3000 bar with exhaust gas recirculation (EGR) has been shown to reduce NO_x by 25% and fuel consumption by 2.5% as well [17-18]. Other means of reducing emissions from diesel engines include fuel blending to change the combustion characteristics. Studies have shown oxygenated fuels tend to reduce soot emissions from traditional diesel injectors by leaning the equivalence ratio at the lift-off-length of the spray [19]. These novel technologies or fuels will be required for diesel engines to meet more stringent emission reductions of the future.

Primary engine control parameters include engine temperature, lubricant temperature, fuel pressure, engine noise from knocking, boost pressure, intake pressure, volumetric efficiency,

ambient air temperature, ambient air humidity, fuel temperature, fuel type or quality, fuel mass used per cycle, fuel delivery timing, fuel consumption, porting or valve configuration, exhaust gas treatment, output torque, mechanical efficiency, and misfires [20]. Typical original equipment manufacturer (OEM) ECU configurations do not allow for tampering of the controls without OEM special software and is discouraged due to changes in emission characteristics that differ from the rated emission standard compliance. Moreover, the use of a diesel engine under a dual-fuel mode would require access to the engine control parameters mentioned above to compensate for the second fuel, which is unknown to the ECU. Dual-fuel conversion kits are available for aftermarket installation which require no engine modifications; however, the ECU update is proprietary to the conversion kit company [21].

2.2 Natural Gas

2.2.1- Physical and Chemical Properties of C_1-C_4 Mixtures

Methane, the primary component of NG, has good anti-knock characteristics when used in high compression engines (methane autoignites at temperatures above 900 K [22]). On the other hand, propane is more likely to auto-ignite under the same conditions. In general, alkane fuels autoignition temperatures decrease with an increased number of carbon molecules with autoignition temperatures of 595°C, 515°C, 470°C, 365°C for methane, ethane, propane, and butane, respectively [23]. In addition to autoignition, the NG composition determines the mixture's physical properties such as its density, viscosity, heating value, and flame speed. Chemical reactions rates are more independent of the blending, with each fuel following its own reaction pathway. Literature on combustion characteristics of pure fuels is widely available [24-27], yet comprehensive data on fuel mixtures is quite limited. Furthermore, laminar flame speed (S_L) data from low quality gas with high inert content has never been an area of interest to researchers. This data would be critical for determining stability limits and combustion strategies in the case of using minimally processed NG at the source.

Methane contributes the most energy in NG blends and has a dominant role on the mixture's overall laminar flame speed. The laminar flame speed of a fuel varies with equivalence ratio, temperature, and pressure. At standard temperature and pressure, the laminar flame speed of methane varies between 15 cm/s to 36 cm/s, with a bell distribution centered around an equivalence ratio of 1.1 [28]. Ethane follows the same bell distribution with slightly higher flame speed values

of 20 cm/s to 40 cm/s. Propane also has the same bell distribution with the highest laminar flame speed of the C_1-C_3 gases, with a small increase over ethane flame speed at 21 cm/s to 42 cm/s. Butane and pentane have nearly an identical flame speed distribution, ranging from 10 cm/s to 40 cm/s [28]. The laminar flame speed of methane decreases with increased pressure, and at 20 atm reaches a maximum value of 10 cm/s near stoichiometry [28]. Laminar flame speed is much more sensitive to temperature of the premixed fuel and air than pressure. Methane burned at stoichiometry has an increase in laminar flame speed from roughly 40 cm/s at 300 K to approximately 130 cm/s at 600 Kelvin [28]. For comparison, at 1000 revolutions per minute (RPM) the instantaneous piston speed (for this research) varies from 0 cm/s at top dead center (TDC) to 700 cm/s during mid-stroke. Regarding methane's laminar flame speed, the piston speed is only below its stoichiometric maximum for about 5 crank angle degrees (CAD). Another important parameter related to laminar flame speed is laminar burning flux. Laminar burning flux does not follow the same relation as flame speed, but rather increases from 0.08 to 0.22 g/cm^2-s when pressure varies from 1 to 20 atm. The burning flux only increases from about 0.04 to 0.07 g/cm^2-s when temperature varies from 300 to 600 Kelvin [28]. Clearly the atmospheric flame speed value does not show direct relevance under the turbulent, high pressure and high temperature in-cylinder conditions; however, many models rely on extrapolation of the laminar flame speed to compensate for temperature and pressure, and turbulence intensity [28].

2.2.2 Minimal NG Treatment for Engine Use

Costs associated with NG shipping and transportation are higher than those for petroleum liquid fuels due the NG's lower density. It is thus more economical to use the gas locally near the source or to liquify the gas into liquified natural gas (LNG) for shipping overseas [29]. Similar to the treatment of petroleum, acidic gases and sulfur containing compounds should be removed for environmental reasons and to avoid corrosion of piping infrastructure [29]. In liquid petroleum fuels, sulfur compounds accelerate the corrosion of engine parts and increase engine deposit formation. Mercaptans in the fuel cause corrosion of copper and brass. In petroleum-based lube oil, high sulfur content increases oil oxidation rate and solid deposits. Traditional NG pre-treatment uses monoethylene glycol (MEG), triethylene glycol (TEG), and a molecular sieve for water removal. It is then followed by a cooling process to remove heavy hydrocarbons and a solid bed, non-regenerable adsorption for H_2S removal [30]. This would constitute a minimal treatment process for the gas to safely be used inside an engine at a production site.

2.2.3 NG Flaring Alternatives

Recently, BP announced a goal of zero flaring on the U.S. mainland by 2025 [31]. Traditionally, NG companies were forced to flare excess products due to storage limitations during periods of low demand and continuous production. Flaring excess gas produces zero useful work, which could be recovered from a heavy-duty engine under both stoichiometric and lean burn spark ignition (SI) configurations, or diesel pilot ignited compression ignition (CI) engine configuration. Further utilization of the wasted energy could be realized from adding waste heat recovery technology to the engine or using a low temperature combustion boiler Rankine system when fuel properties are outside of engine operating limits. Utilization of C_1-C_4 excess gas in diesel-NG dual-fuel engines is the primary research focus here because it could be less affected to large changes in gas composition. In the worst-case scenario, the diesel substitution rate may be lowered as needed to compensate for poor combustion characteristics of specific C_1-C_4 compositions.

There are few companies who make Rankine cycle generators that utilize flared gas in a low temperature combustion chamber boiler [32]. This energy recovery method was shown to reduce emissions of CO, NO_x, and volatile organic compounds (VOCs) by 89.1%,48.1%, and 92.8%, respectively, as compared to open flaring [32]. The reduction in emissions is due to increased level of control over the combustion mode as compared to traditional diffusion-based flaring, which suffers higher rates of incomplete combustion in an uncontrolled external flow field. The emission reduction is also coupled with the benefit of power generation, which can be scaled in size [32]. Under this combustion mode, laminar flame speed data and combustion characteristics under ambient conditions would be more useful. Alternatively, commercial systems using a Rankine cycle (such as Gulf Coast Green Energy-Rankine system) utilize waste heat from the water jacket of a stationary engine to further improve the total energy recovery rates. Large scale examples of combined heat and power systems fueled by NG can reach combined efficiencies of up to 88% while operating on a wide variety of fuels [33].

2.3 Emission Regulations for Heavy-Duty Engines

U.S. Environmental Protection Agency (EPA) code of federal regulations (CFR) Title 40 part 1039 defines the emissions limits that new and in-use stationary CI engines must meet. EPA requires all stationary engines built after 2014 to meet Tier 4 emission standards and fall at or below 0.19 grams per kilowatt hour (g/kWh) non-methane hydrocarbons (NMHC), 0.40 g/kWh NO_x, 0.02

g/kWh particulate matter (PM), and 5 g/kWh CO [34]. Tier 5 regulations have not been announced but are expected to adopt PN (particulate number) limits similar to European Union (EU) stage V emission limits adopted in 2018 [35]. NG engines use NMHC emissions standards instead of total hydrocarbon (THC), due to the reactivity in ozone production of C_2 and higher fuel components. Ozone is formed from the combination of NO_x and VOCs in the presence of heat or sunlight [36]. EPA ranks propane and butane as very volatile organic compounds which occur primarily in gaseous form in the atmosphere and are highly reactive in ozone formation [37]. National ambient air quality standards have been placed on CO, NO_x, PM, SO_x, lead, and ozone [38]. Methane, while unregulated toward hydrocarbon (HC) content, contributes to the net carbon dioxide (CO_2) equivalent. The global warming potential (GWP) of methane has been recently increased from a factor of 25 to 28-36 times the potential of CO_2 per unit mass over a 100-year period [39]. Ethane, propane, and butane also carry a GWP of 6, 3, and 4 respectively [40]. From an environmental standpoint, the improvement in Carbon dioxide equivalent ($CO_{2,eq}$) emissions from transitioning to dual-fuel engine operation would come from a decrease in both the short term GWP (C_1-C_4 components) and long term GWP (CO_2).

Table 1- Emission Limits Non- Road CI Engines After 2014 (g/kWh) [34]

(Table 1 of 1039.101)

	Maximum Engine Power	PM	NO_x	NMHC	CO
Non-road CI engines	56<kW<130	0.02	0.40	0.19	5.0

Previous research conducted on the same engine platform as the one used in this study (John Deere, Model 4045) focusing on diesel combustion and emissions gave insight into how the engine must be operated to meet emission standard compliance. 200-MPa injection pressure of diesel and 41% EGR rate by mass was identified as a suitable condition for diesel operation to remain within the Tier 4 standards of PM and NO_x using a similar 6-hole injector to the OEM [41]. In general, diesel engines will be required to operate at high rates of EGR for low NO_x, higher injection pressures (above 2500 bar) for low PM, and aftertreatment with selective catalytic reduction for NO_x reduction to achieve near Tier 4 emission levels [42]. Higher injection pressure correlated with higher NO_x production but lower soot [42].

2.4 Dual-Fuel Engine Literature

NG composition varies with time and location. The requirements for pipeline quality NG are (by volume) minimum 75% methane, maximum 10% ethane, and maximum 5% propane [6]. Methane exhibits the highest knock resistance of the NG components. As higher carbon components (propane and ethane) increase in the NG mixture the fuel becomes easier to ignite and burns slightly hotter which increases thermal NO_x production [43]. Higher carbon components are less knock resistant, or easier to ignite than methane [44] and increase the regulated NMHC content in the exhaust. The higher carbon components, especially propane, burn inherently richer than methane causing increased CO production [43]. Different types of dual-fuel or dedicated NG engines offer benefit under certain fuel quality and operating conditions. The fuel composition directly influences the chemical reaction rates which determine in-cylinder peak combustion temperature and pressure rise rate. As a result, combustion quality, phasing, and duration will be affected, resulting in changes to engine performance, emissions, and efficiency [45], which will be further investigated in this section.

NG Fueling Advantages

- Locally produced fuel (e.g., in the Marcellus Shale Region)
- Lower CO_2-equivalent emission production
- Reduced particulate matter/soot emissions
- Engine may be partially or fully operated on NG depending on engine configuration
- Fuel cost reductions (15-30%) [21]
- Cleaner burning fuel, NG, increases engine life [21]

NG Fueling Disadvantages

- Bulky fuel storage containers required (issue for on-road applications)
- Less energy density than liquid fuels
- CH_4 emissions from crevice volumes (indirect injection systems)
- Lower volumetric efficiency
- Reduced brake power as compared to traditional fossil fuels
- More suitable for stationary power production than transportation vehicles

2.4.1 Dedicated NG SI Engines

Dedicated NG engines offer benefits in emission reduction and fuel cost saving when NG fuel quality is of pipeline standards. Current large displacement transportation or industrial four-stroke dedicated NG engines offer excellent emission reduction. For example, Cummins ISL G Near Zero 239 kilowatt (kW) engine produces 0.02 g/bhp-hr or 0.027 g/kW-hr NO_x, which is 90% less NO_x than current EPA standards and has a 9% greenhouse gas (GHG) decrease [46]. This stoichiometric SI NG engine is equipped with a three-way catalyst and requires NG with a methane number (MN) higher than 75. Other non-road NG SI engines operate under lean burn conditions, such as Caterpillar engines with oxidation catalyst [47]. The lean burn design is useful at reducing NO_x by lower combustion temperatures and pressures and provides fuel economy benefits [47]. Testing of various lean burn NG engines showed a trend of increasing NO_x and HC emissions with decreasing MN and increasing Wobbe index (WI). Higher WI was also associated with increased maximum cylinder pressure [44]. NMHC emissions were shown to increase with decreased MN and were proportional to NMHC contents in the fuel. CO emissions were relatively constant for all gas blends and well below standards. The stoichiometric ISL G engine did not follow any clear emission trends with regards to fuel composition. For all engines, higher WI resulted in decreased fuel consumption [48].

Dedicated NG fueling affects volumetric efficiency as it uses two gaseous intake constituents (air and gas) rather than air alone. This competition in breathing generally rules out port fuel injection of NG as an equivalent to gasoline or diesel operation. Lean burn SI NG combustion is also prone to erratic flame kernel formation because of cyclic turbulence variations [12]. NG has a higher GHG potential than traditional liquid fuels due to high amounts of CH_4 present in the combustion products. NG also has limitations for vehicle use, requiring bulky storage tanks or cryogenic LNG tanks. However, NG is easier to distribute for stationary power generation at drilling sites, pumping stations, and processing facilities.

2.4.2 Diesel NG Dual-Fuel Engines

Diesel NG dual-fuel engines offer more flexibility to variations in NG composition that can change continuously with time and location. NG with higher C_2-C_4 content has a lower WI, MN, and fuel lower heating value (LHV). The dual-fuel diesel-NG engine can adjust operating conditions for high C_2-C_4 content by using a lower NG substitution rate when needed, which is not possible under

dedicated NG operation. A general trend for dual-fuel diesel-NG engines shows decreased NO_x and CO_2 with increased CO and THC emissions over diesel-only mode [49-54]. In transportation applications, tests have shown dual-fuel engines to be more economical using only diesel at low-load but dual-fuel operation at high loads [49]. Significant combustion losses can occur under low load conditions when the premixed fuel-air equivalence ratio becomes excessively lean ($\phi = 0.27$) with substitution rates of 50%, and further decreases ($\phi = 0.11$) at the 20% substitution rate.

2.4.2.1 Fuel Composition Effects

A review of NG direct injection (DI) dual-fuel diesel engines showed that the methane content becomes more important under low-load conditions with respect to thermal efficiency [8]. Research has examined the possibility of ECU programs for dual-fuel engines which include a torque response model for various inputs of NG substitution rate, start of injection (SOI), and air-fuel ratio (AFR). Reference [55] found it was possible to create a simple programable torque curve for dual-fuel operation using commercially available NG; however, the effect of changing NG composition was not studied. Simulation studies of dual-fuel methane diesel combustion with various replacement percentages showed that increased methane percentages caused lower peak pressure and higher ignition delay compared to diesel-only combustion [56]. Increased percentages of CH_4 decreased NO_x and CO at part-load, but slightly increased CO_2 when keeping fuel energy constant [56]. A small increase in thermal efficiency was noticeable in NG mixtures with lower methane content at higher fuel energy replacement levels, but less noticeable at levels below 40% energy substitution [8]. Hydrogen (H_2) addition to dual-fuel diesel-NG engines increased the mixture flame speed, hence a faster flame growth rate and more distributed flame [57]. H_2 addition mainly affected the initial and middle stages of combustion, therefore allowing for a better premixed combustion and engine stability [57]. Ignition delay was not significantly changed when comparing H_2 and NG under increasing substitution rates [58]. The use of both H_2 and NG would be ideal for improved performance over the entire engine operating range [58], but would require more a complex fueling system, lower H_2 prices, and a higher degree of access to H_2. While higher carbon fuels (C_4-C_5) also have an increased flame speed over methane, a similar combustion enhancement may be noticed in blends with higher NGL content. Research conducted in rapid compression machines and shock tubes on C_1-C_5 blends found that regardless of the initial conditions (ϕ, T_0, P_0) fuel mixtures with higher NGL content are more reactive, which decreased

ignition delay [59]. Similar work by the authors found that larger NGL fractions produced a faster ignition, but the ignition seemed to depend more on pressure than AFR [60].

Experiments by Krishnan et al. [61] using 80% substitution rate of diesel by pure propane at high load were limited by high rates of CO and HC emissions for diesel start of injection (SOI_{DIESEL}) of 5 CAD before top dead center (BTDC) and high pressure rise rates for SOI_{DIESEL} of 20 CAD BTDC. Other research shows that propane decreases the ignition delay at high load while methane increases it [62].

2.4.2.2 Injection Strategies

Dual-fuel engines have been shown to be sensitive to 50% mass fraction burned (MFB50) timing in regard to changes in THC emissions. Under low load, as MFB50 advanced from 12 CAD after top dead center (ATDC) to 6 CAD ATDC, the THC emissions reduced by 5 g/kWh with a slight increase in NO_x [9]. Advancing the SOI_{DIESEL} from 10-30 CAD BTDC decreased CO and HC emissions but produced high NO_x compared to very advanced (50 CAD BTDC) SOI_{DIESEL} [63]. By advancing the SOI_{DIESEL} from 10 CAD to 50 CAD BTDC, NO_x, CH_4, and CO emissions reduced 65.8%, 83%, and 60%, respectively, while thermal efficiency increased 7.5% for 75% energy replacement and 25% load conditions [63]. An increase in rail pressure from 600 bar to 800 bar under low load conditions resulted in a 2 g/kWh reduction in THC, reduction in smoke, but an increase in CO emissions [9]. Research shows that earlier injection of the pilot diesel results in increased thermal efficiency and reduces NO_x emissions [64]. Also, earlier diesel injection timing is more beneficial for combustion efficiency under dual-fuel operation [65]. Multiple pilot injections at 40/30 CAD BTDC did not increase the thermal efficiency over single pilot injection at 30 CAD BTDC, single pilot injection at 7 CAD BTDC decreased thermal efficiency significantly and increased THC by nearly 5 times compared to early pilot [64]. Injection strategies such as pre-main-post have been shown to decrease unburned methane and NO_x emissions and increase efficiency in dual-fuel engines operated at high load with 50% replacement [66]. Pre-main-post injection reduced unburned CH_4 from 0.8 g/kWh to 0.37g/kWh and reduce overall GHG emissions and NO_x by 10% and 47%, respectively, over the single injection strategy [66]. Main-post injection at 40 CAD ATDC was also shown to reduce unburnt CH_4 trapped in the crevice regions that escape later in the expansion stroke [66]. Single and pre-main injection resulted in the lowest GHG emissions of 593.6 g/kWh and 596.1 g/kWh, respectively [66]. Using this same method of pre-main-post injections with very advanced pre-injection (80 CAD BTDC), yielded

low GHG emissions and high indicated efficiency [67]. Multiple pulsed NG injections into the manifold have also shown potential for efficiency improvements [68], but would require increasingly more complex controls. Split diesel injections are easier to achieve and have a clear benefit to brake thermal efficiency and fuel consumption under dual-fuel operation [53]. Indicated mean effective pressure (IMEP) was shown to vary less under dual-fuel operation than diesel over a range of pilot injection timings [69]. A higher number of fuel injection orifices was more efficient for mixing the air and fuel than higher injection pressure [70]. Numerical simulations found the lowest fuel energy consumption in dual-fuel operation to occur for diesel-to-NG fuel ratios of 0.2 to 0.3 and injection timing of 30 CAD to 15 CAD BTDC [71]. Higher injection pressure (700 bar vs 500 bar or 300 bar) decreased HC emissions at 7 bar IMEP and 54% diesel replacement by methane [72], which attributed the high HC to the low diesel spray penetration at lower injection pressures as compared to the lower excess air ratio. Experiments at 70% substitution, low load (4.05 bar IMEP), and 910 RPM show increasing the diesel injection pressure from 525 bar to 800 bar decreases the net $CO_{2,eq}$ and HC emissions for dual-fuel operation but not for diesel baseline operation [73]. A split diesel injection decreased the net $CO_{2,eq}$ for dual-fuel operation to 640 g/kWh which was below the diesel baseline and 11% lower than dual-fuel operation with a single diesel injection [73], it also lowered HC emissions.

Low temperature combustion (LTC) strategies utilize an extremely advanced diesel injection (typically 50 CAD BTDC). Early injection of pilot diesel at 50 CAD BTDC followed by a second injection between -40 to 15 CAD ATDC under 85% replacement was found to reduce HC emissions by 54%, CO by 46%, NO_x by 7%, and increase indicated fuel conversion efficiency by 11% as compared to single early injection [74]. Increasing the injection pressure in this case benefited the efficiency-emission tradeoff and fuel conversion efficiency [74]. Under high energy replacement levels (90%) a clear shift in combustion mode was noticed for advanced diesel pilot injection timings (32.5 CAD to 55 CAD BTDC), while for pilot injections (30 CAD BTDC to TDC) the combustion mode resembled a typical diesel combustion mode [75]. The critical change in combustion mode correlated with in-cylinder bulk temperature being above or below 800 K, such that at temperatures below 800 K the fuel atomization occurred slower and caused a two-stage autoignition mode [75]. The two regimes of injection timing were also detailed by Guo et al. [76], who found that $BSCH_4$ emissions remained near constant at 5 g/kWh for SOI_{DIESEL} of 60-25 CAD BTDC but then increase to slightly over 20 g/kWh for SOI_{DIESEL} = 10 CAD BTDC and 75%

replacement with pipeline NG, under low load (4 bar BMEP) and speed (910 RPM). This can have an important impact on emissions as well. Other works by Guo found CH_4 and CO emissions levels of 25 g/kWh and 20g/kWh, respectively, for 75% substitution rate, 4.05 bar IMEP, and a SOI_{DIESEL} of 10 CAD BTDC; this was lowered by 6 and 5 times, respectively, when switching to LTC with SOI_{DIESEL} = 50 CAD BTDC [73].

2.4.2.3 EGR Usage

The use of EGR with diesel dual-fuel engines was shown to have a beneficial effect on the soot-NO_x tradeoff [77]. There was a steady increase in brake thermal efficiency with increasing the EGR rate from 0-25% by mass and a trend of decreasing CO, THC, and NO_x emissions with increased EGR rate, at substitution rates of 90% NG and diesel pilot injection of 7 CAD BTDC [78]. At low load and 40% substitution, increased EGR reduced THC by 11 g/kWh and NO_x reduced from 0.9 to 0.1 g/kWh [9]. The emission values for dual-fuel operation ranged from 620-680 g/kWh $BSCO_{2,eq}$, 2.5-4 g/kWh $BSCH_4$, 2-9 g/kWh $BSNO_x$ with and without EGR, 1.5-4 g/kWh BSCO at 1000 RPM [77]. High EGR was the best way to reduce NO_x, while higher intake pressure increased engine efficiency and decreased soot [70]. EGR thermal effects were more dominant than EGR chemical effects, with CO_2 thermal contribution greater than H_2O contribution [79]. Temperature had more effect on chemical reactivity of EGR components such as C_2H_2, CO, CH_4, and NO than pressure [79]. Lower EGR rate and higher diesel injection quantities were beneficial for CH_4 oxidation [71]. Lastly, as EGR is known to be an effective measure at lowering the maximum pressure rise rate (MPRR), the use of EGR aided in lowering NOx formation, which was found to be proportional to the MPRR [65].

2.4.2.4 NG Substitution Rate Effects

A recently developed dual-fuel engine (Mahindra & Mahindra Ltd) was successful at meeting emission standards (for TREM III A) but on average uses only 40% compressed natural gas (CNG) substitution [80]. At 50-60% load, a substitution rate of 30-35% was used over the entire operating speed range, while over 50% substitution provided better fuel economy at high load and 1000-1400 RPM [80]. A 40% substitution rate was shown to reduce CO_2 emissions by 10% compared to baseline diesel emission levels at higher speed and load, and by 21% at mid-load [81]. At mid-load with high excess air ratios under high substitution rates, combustion losses can be as high as 20-35%, essentially eliminating the reduction in CO_2 based on fuel chemistry and negating fuel cost savings [81]. When increasing the energy substitution rate from 0% to 90%, a trend of

decreased cylinder pressure and thermal efficiency with increasing cyclic variation in maximum cylinder pressure and IMEP was observed [82]. Increasing engine speed from 1335 RPM to 1655 RPM with increasing NG substitution further reduced the thermal efficiency, more so at high substitution rates [82]. Another study found that increasing methane energy substitution rate decreased NO, CO, and soot emissions for experiments conducted on an engine with 17:1 compression ratio at 1500 RPM, SOI_{DIESEL} of 5 CAD BTDC, and 5 bar BMEP [83].

CA10 advanced significantly at 10% and 50% substitution rates and delayed significantly at 90%, while CA50 first advanced with increased replacement then delayed [82]. Heat release rates were the fastest for 70-90% replacement, slowest and most unstable for 30-60% replacement, and initial stage combustion occurred faster and was more stable for modes with over 50% replacement [82]. Peak brake thermal efficiency was reported slightly above 39% for 75% energy replacement at an early SOI of -22 CAD ATDC [77]. A trend of increased HC and NO_x at increased levels of replacement, with decreasing CO_2 and PM was also found [84]. Other studies show it was possible to have extreme replacement by NG of up to 99%, which promoted end-gas ignition of the premixed fuel [85]. A 35 DBTDC injection was shown to increase brake thermal efficiency to nearly 35% in high substitution cases (90%) when EGR and intake throttling were used [78]. Simulation studies determined the increasing methane percentages primarily influence ignition delay by changing the specific heat of the mixture, followed by dilution effects of low oxygen [86]. Both effects reduced chemical reactivity during the low temperature combustion phase but increase the global reactivity and temperature [86].

Studies conducted on Cetane Number (CN) of the ignition fuel under dual-fuel diesel-NG operation have shown that higher CN fuels were beneficial. CN over 45 maintained brake thermal efficiencies closer to that of baseline diesel. Ignition delay was shown to increase with increasing NG replacement for all CN ignition fuels, with ignition becoming unstable at replacement levels over 78% even for high CN fuels [87]. The dilution of air by methane nearly doubled the ignition delay when energy replacement reached upper limits of 98% [22]. At 1000 bar rail pressure, higher CN fuel was shown to benefit dual-fuel combustion efficiency and decreases CH_4, THC, and CO emissions at 97% NG replacement compared to a lower CN pilot fuel [88]. As pilot fuel aromatic content increases, combustion efficiency also increases, along with decreased unburnt CH_4 at the expense of increased NO_x [88]. When higher fuel rail pressure is used, lower CN fuels with

aromatics show enhanced combustion characteristics over higher CN fuel without aromatics [88]. It was noted that for over 95% replacement rates at low load the diesel pilot amount becomes smaller than what typical injectors were designed to deliver, making injections unstable and with less chance of igniting the NG mixture [78]. The combustion heat release rate occurs faster than traditional diesel when using high NG replacement levels (80%) [69]. Flame kernel formation at higher NG energy replacement levels (70-85%) was shown in optical studies to occur scattered throughout the combustion chamber [89].

Experimental studies show too high of an energy replacement at low load conditions by NG becomes unstable at around 90%, suggesting for suitable emissions levels to limit the replacement to 60% [90]. As the methane energy content reaches high levels (60-90%), the diesel pilot flame becomes increasingly weaker, and the combustion characteristics become more premixed flame propagation controlled [90]. Even at 60% replacement there is a significant shift into a premixed burning regime as detailed by optical experiments [91], which follows the same trend observed by others [92]. Under high load conditions the substitution rate of NG can increase up to 95% with near stoichiometric conditions [90]. A CO_2 reduction from 756 g/kWh to 544 g/kWh was shown for 22% replacement of diesel energy by methane, with little effect on ignition delay [50]. High replacement percentages (75%) by NG show major impact on net $CO_{2,eq}$ (~1200 g/kWh) for low load conditions at SOI_{DIESEL} 10 CAD BTDC [76]. Significant ignition delay occurs under higher levels of NG energy replacement (85%) also noting a degraded combustion process [89,92]. For 90% replacement, it was found that for advanced diesel pilot injection from 5 to 35 CAD BTDC the combustion duration of the NG decreased from 35.5 to 16.5 CAD, respectively [93]. The shortest combustion duration was found to have the best fuel consumption and emission characteristics [93]. Late pilot SOI (TDC) shows a trend of decreased indicated efficiency with increasing NG energy replacement from 52-70%, however an inverse trend occurs for pilot injection timing 30 CAD BTDC [94]. Heat transfer was found to increase drastically (near double) but decrease combustion losses and exhaust losses for the 30 CAD BTDC pilot as compared to TDC pilot [94]. Increasing NG substitution rate is also associated with higher rates of pressure rise, suggesting longer ignition delays in the pilot fuel allow the NG to also autoignite under high compression ratio in-cylinder conditions around TDC [95]. Preheating the intake air was shown to allow increased NG energy substitution rates with stable combustion [96].

Cycle to cycle variation of maximum cylinder pressure and heat release were found to be a compounding issue of cycle differences in the mass of ingested gas, in-cylinder mixture stratification, gas temperature and turbulence at intake valve closure, and diesel start of injection [97]. As the equivalence ratio becomes increasingly lean ($\phi = 0.5$), THC and CO emissions rise considerably compared to richer conditions ($\phi > 0.5$) with high substitution rates (95-97%) [70]. Early pilot injection (30 CAD BTDC) and lower substation rates resulted in the highest NO_x and lowest THC and CO, while a pilot injection at 10 CAD BTDC with high substitution resulted in the lowest NO_x but highest CO and THC emissions [91]. CH_4 emissions accounted for the majority of THC emission under increasing NG energy replacement at 82.4%, 84.9%, 87.4% for energy replacements of 30%, 50%, and 70%, respectively [89]. Total CH_4 emissions were higher at 50% replacement due to shorter combustion duration than for the 70% case [89]. It was found in other studies with NG replacement levels of 50-87% that CH_4 accounted for 52-87% of the THC emissions [94]. Increasing the substitution rate from 20% to 80% reduced NO_x but increased CO and HC, regardless of SOI_{DIESEL} [65]. The larger substitution rates cause more incomplete combustion (increased amount of low-reactivity fuel) with combustion stability issues setting an upper limit on replacement percentage [65].

2.4.2.5 Engine Load Effects

Engine load plays a critical role in the emission formation process. Reference [72] show a steep increase in HC emissions as engine load decreased from 7 to 2 bar IMEP, primarily at higher replacement levels in a diesel-methane dual-fuel engine. Also, a higher load and substitution rate decreased BSCO and $BSCO_2$ emissions in general, except for $BSCO_2$ at the lowest load levels (2 bar IMEP) [72]. Mitchell and Olsen [96] conducted high load experiments with 35-55% diesel replacement using a 6-cylinder tier 2 heavy-duty engine and observed dual-fuel emissions similar to diesel operation (i.e., NO_X was unaffected and CO+HC slightly increased), with roughly 2% of the initial NG fuel fraction unburnt in the exhaust. At medium load and 65% diesel energy substitution, a larger fraction of NG was unburnt, with flame quenching late in the expansion stroke and higher emission levels limiting the diesel substitution rate. Under low load (~10% of the maximum load) and ~50% diesel replacement, reference [96] observed that 20% of the initial NG was unburnt in the exhaust, attributed to the mixture being too lean to propagate a flame outside the diesel fuel plume region. At 25% load, HC emissions were less sensitive to SOI_{DIESEL} compared

to the diesel replacement rate. Low load conditions are also prone to speed and power fluctuation [96].

2.4.2.6 Engine Design Considerations

One predominant issue with converting existing diesel engines to dual-fuel operation is the stock diesel piston design. It has been shown that crevice volume from the piston top land results in as much as 75% of NG emissions [98]. The use of specialized low crevice volume pistons would require additional cost in converting traditional diesel engines into dual-fuel operation; however, it may become necessary to meet stricter emission standards. Modeling studies focused on the dual-fuel bowl design found that methane emissions could be reduced with optimized bowl design at the expense of a NO_x increase [99]. Also, adjustments to the intake valve closure timing may be required to avoid any backflow of lean NG mixture for late closure timing, hence uneven distributions of fuel cylinder to cylinder [100]. In the case of negative valve overlap, premixed gases could slip into the exhaust for a brief period around the time of intake valve opening. It was also found that at extra lean equivalence ratios (<0.4), a larger piston bowl diameter was beneficial in reducing THC emissions and increasing efficiency; however, there was little difference with respect to piston bowl diameter for cases not so lean [101].

Optimum in-cylinder flow motion is paramount for efficient combustion. An investigation on the effects of swirl and tumble motion on dual-fuel combustion showed higher swirl ratios improved combustion efficiency, reduced soot, and improved crevice HC oxidation, but also increased the wall heat transfer. Dual-fuel diesel engines were relatively insensitive to tumble as compared to conventional SI NG-dedicated engines [52]. Moderate intake throttling was shown to reduce CO and THC in dual-fuel operation and increase indicated thermal efficiency and combustion efficiency [51]. Controlled ignition of the premixed mixture in the end-gas region was also shown to be beneficial in reducing unburned THC emissions and well as improved efficiency at high IMEP. A compression ratio of 16.5 was suitable for low emissions and high efficiency as compared to a CR of 14.5 or 18.5, which suffered from misfires at low loads and rapid combustion at high loads, respectively [51]. Increasing the compression ratio over 17 with advanced SOI_{DIESEL} was shown to increase efficiency and offer a mechanism to lower CO but could only be completed for high substitution rates, due to high pressure rise rates at lower substitution levels [83]. Increased intake pressure and excess air ratio by turbocharging has been shown to reduce NO_x, with peak efficiency in the 1.5-1.65 bar boost pressure [102]. Increased indicated efficiency and lower NO_x

was noted for higher mass fractions of methane [102]. Intake throttling with EGR was shown to reduce brake specific CO and THC, with increased brake thermal efficiency and NO_x for high NG substitution rates [78]. Other research points out that dual-fuel operation favorably reduced PN on the whole range of particle sizes measured [103]. It was found that 60% of the PN in dual-fuel operation is ultrafine particles, however they only contributed to 10% of the PM emissions [104].

Reactivity-Controlled Compression Ignition (RCCI) modes of dual-fuel operation with pilot injection 60-84 CAD BTDC have been shown to improve indicated efficiency and reduce THC emissions [94]. Premixed Charge Compression Ignition (PCCI) modes of dual-fuel operation reduced THC and CO but increased NO_x as equivalence ratio increased from 0.6 to 0.7 [105]. PCCI with two pilot injections offered significant advantages in reducing emissions of NO_x, THC, and CO by 17.6%, 35.5%, and 45.1% respectively and fuel consumption by 1.88% [105]. Other techniques such as cylinder deactivation were found to be successful at reducing CH_4 and CO emissions at low load levels, while maintaining higher levels of NG substitution [106].

2.5 Optical Engine Studies on Combustion

Optical engines are the best available tool for understanding in-cylinder combustion processes. Generally, the combustion phenomena are recorded with a high-resolution and high-speed camera. By illuminating the flow field with high energy lasers or LEDs and filtering the images with wavelength-dependent filters, certain radical species may be analyzed. The radicals of OH (excited between 284-310 nm wavelengths [107]) are of particular importance as they are produced mainly inside the chemically reactive flame front and are important in soot oxidation. Optical studies conducted only with diesel (or diesel surrogates) show important aspects of soot formation and oxidation, such as a general trend of decreasing exhaust soot emissions with increased injection pressure, with some non-linearity attributed to swirl ratio [107].

Dual-fuel studies were previously conducted in optical engines to gain insight into flame propagation phenomena with increasing methane replacement [10, 108]. Higher methane replacement levels increased the ignition delay of the pilot fuel [89, 109]. The influence of turbulent flow motion, changing pressure, and temperature on combustion characteristics of a particular fuel composition were also observed. Optical investigation of a mid-load combustion process showed that high excess air (i.e., high boost pressure) increased the incomplete combustion of the premixed fuel; however, a flame front was observed at lower boost pressure [81]. In addition,

optical measurements suggested high levels of knocking and pressure oscillations at high diesel replacement percentage (99%), which amplified until temperature decreased or fuel was depleted during the combustion process [110]. Tests conducted by Kim et al. [65] using an optical diesel-NG dual-fuel engine with SOI_{DIESEL}=10 CAD BTDC and 40% energy replacement found that NG aided in the premixed flame development, however a fuel-rich diesel pocket was still formed around the piston bowl.

2.6 Research Objectives

Most gas production sites are also very remote (hence more difficult to access from a logistical point of view). Therefore, the usage of minimally treated and less demanded components of NG directly at the source will benefit production costs while also supplementing local power production and conserving energy in the NG production sector. As combustion characteristics of dual-fuel diesel-NG engines are known to deteriorate at lower load conditions [90], the major tasks of this study were:

1. Develop a testbed for a near production engine capable of simultaneously and robustly controlling both the direct injection of the diesel fuel and the sequential port-fuel injection of NG inside the intake manifold. Conduct experiments under lower load conditions where various C_1-C_4 mixtures of fixed energy content are supplied. Analyze the experimental data to determine the effect of C_1-C_4 mixture composition on engine performance and emissions.
2. Use the same engine controller to conduct experiments in an optical access version of the same engine. Optical experiments will visualize the combustion phenomena and will primarily investigate the cases with poor combustion behavior associated with certain fuel compositions as found from Task 1. Ignition quality and flame propagation of different fuel mixture compositions will also be compared.
3. Compare the results of the various gas blends with the data collected from the burner experiments. Analyze laminar flame speed of each gas blends to determine if a higher flame speed improved the combustion characteristics of the C_1-C_4 mixtures investigated in previous tasks.

2.7 Summary of Major Contributions

The aim of this dissertation was to investigate the combustion characteristics of C_1-C_4 blends using three different experimental platforms. The major research questions to be addressed were as follows:

1. How does C_1-C_4 mixture composition and substitution rate influence the combustion characteristics at low load conditions in a dual-fuel diesel-NG engine?
2. Does a C_1-C_4 mixture with a higher laminar flame speed (S_L) have a better combustion behavior, or are other physical and chemical properties of the mixture also important?
3. What noticeable changes in the combustion phenomena can be assessed with an optical engine, when both C_1-C_4 composition and substitution rates are changed?

In addition, the data collected in this study will also benefit the modeling community as the effects of variable C_1-C_4 mixtures on dual-fuel combustion characteristics are very difficult to find in literature.

3 Methodology

The experiments consisted of three separate testing platforms, with a goal of gaining insight into the combustion phenomena related to utilizing different NG fuel composition at low load and low speed in a stationary heavy-duty dual-fuel diesel engine. The primary experiments were conducted on a near production industrial diesel engine (i.e., a simple conversion to allow for partial fueling by NG). Laminar flame burner experiments were conducted to provide additional information on laminar flame speed differences of the compositions utilized. Lastly, the pure NG components were examined using an optical access version of the production engine to visualize the stratification and premixing effects of the main components used to create the NG fuel blends. As differences in laminar flame speed were expected to be small based on literature, the use of pure methane, ethane, and propane components for optical experiments provided a way to measure the largest possible differences that could be visualized.

- Burner experiments measured C_1-C_4 flame parameters of mixtures representative of well head or pretreated NG
- Engine experiments investigated the effect (and usage limitations) of physical and chemical properties of C_1-C_4 mixture on engine efficiency and emissions

- Optical engine provided additional information with respect to compounding flow motion effects on the combustion process in addition to C_1-C_4 mixture effects

3.1 Metal Engine- Setup

The heavy-duty diesel engine (John Deere, Model 4045-HFC04; mentioned in the next sections as the "metal engine" to differentiate it from the optical version of the same engine platform) used for the bulk of dual-fuel diesel-NG engine experiments. The engine was operated in dual-fuel mode by adding two low-pressure NG injectors (Rail Spa, Model IG7 Navajo) that inject NG into the intake manifold just before the intake valves. A National Instruments PXI 8106 alongside Drivven engine control cards for NI-RIO and CalVIEW software controlled engine operation. The control cards included two Drivven Direct Injections drivers, two Drivven Port Fuel Injector drivers, a Drivven AD-Combo, a Drivven Low-Side controller, and NI-9401 and NI-9402 expansion cards. The engine controller software required NI LabVIEW FPGA, Real-Time, and Full software suite to allow the user to make changes to the program. Modifications to the CalVIEW application were needed to accommodate the transition to dual-fuel operation and adjust inputs such as encoder type, encoder Z-pulse alignment to engine TDC, gating every other Z-pulse for four-stroke operation, skip-fire controls, and more. Outputs were also modified to show and record the injection command along with the high-speed in-cylinder pressure data. The Low-Side module controlled the suction control valve, EGR valve, and boost valve. The entire platform was designed in such a way that it was capable of easily transferring it to the optical engine setup.

A separate LabVIEW program on a different computer was used to control the dynamometer, control and/or measure C_1-C_4 flows (via AliCat flow controllers and meters), control the diesel common rail suction control valve, as well as collect and display the low-frequency engine data. The low-frequency data included numerous thermocouple measurements, the diesel fuel digital scale (used to measure the diesel fuel consumption), engine load, engine speed, EGR valve position, various air and gas pressures, etc. Intake airflow was measured using a Meriam 4-inch laminar flow element (LFE) with classical coefficients and then standardized within the LabVIEW program.

A pressure transducer (Kistler 6056A) connected to a charge amplifier Kistler 5010B measured in-cylinder pressure data, which was then transferred to a fast data acquisition board (National Instruments SCB-68A, 100kHz sampling) and LabVIEW software that recorded it. The fast data acquisition board also collected high-speed data from the 1800-bit engine encoder signal, the high-frequency intake and exhaust pressures, and the injection command signal, which were used later for the analysis. For example, the high-frequency intake pressure data was used to peg in-cylinder pressure data at the time of the intake valve closing.

Emission measurements were collected using a Fourier Transform Infrared Spectroscopy Analyzer (FTIR) gas analyzer (MKS, Model Multigas 2030). Emissions data was given time to stabilize between test runs before collection, then recorded emissions values were averaged over three-minute steady-state engine operation. Commercial software (MKS MG2000) controlled the FTIR operation and emissions data acquisition. The emission analyzer was calibrated each day prior to data collection using a certified quad blend gas bottle (NO_x, CO, CO_2, and C_3H_8) and a 10,000-ppm CH_4 gas bottle. A heated line (Atmo-Seal, Model IGH, 190°C) delivered sample emissions to the FTIR for measurements. For a more accurate sampling of the C_1-C_4 hydrocarbon emissions, the analyzer was operated using the NG recipe developed by the FTIR manufacturer specifically for such fuel. This recipe interprets the unburned diesel emissions as a C_1 equivalent.

All engine tests were conducted at low engine speed and low load conditions. A dynamometer (Medsker Electric Inc.) maintained a constant speed of 1000 RPM and engine load was selected such as operating conditions could be replicated in the optical version of the same engine. The design of experiments considered that if preliminary data warrants further investigation, then data will be collected at other speeds. Overall, three separate LabVIEW applications were used in data collection: a modified Drivven CalVIEW for the dual-fuel control, one for the high-speed pressure data, and one for the low-level dynamometer and engine controls and the low-frequency data. Pressure data and emission data was averaged over 200 cycles. Figure 2 illustrates the design of experiments and Figure 3 shows the experimental setup. Table 2 lists the metal engine specifications. Fuel properties and naming conventions are discussed later in Section 3.5.

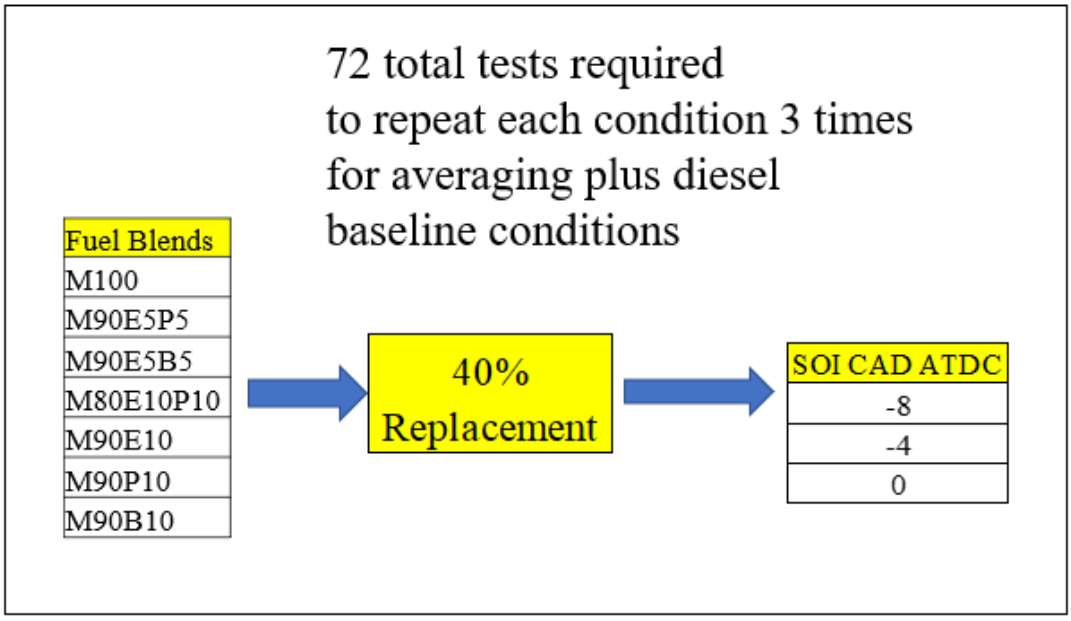

Figure 2- Test Matrix for Metal Engine Experiments

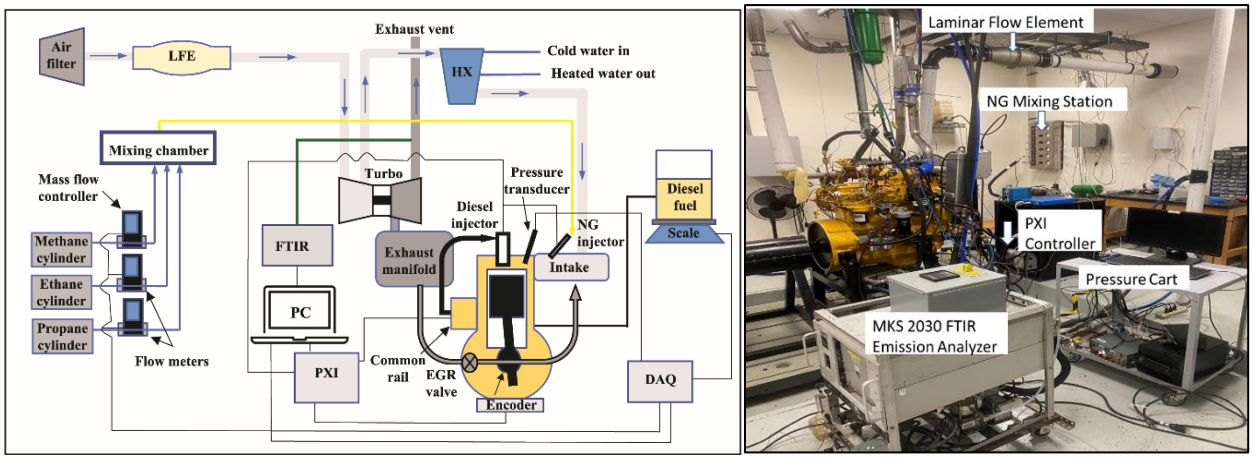

Figure 3- Metal Engine Experimental Schematic (left) and Laboratory Setup (right)

Table 2- Metal Engine Parameters

Engine Type	4-cylinder, 4-stroke Diesel, Turbocharged, Common Rail
Engine Make and Model	John Deere 4045-HFC04
Bore and Stroke [mm]	106 x 127
Displacement [L]	4.5
Compression Ratio	17.0:1
Fuel System Diesel/NG	Direct Injection / Sequential Port Fuel Injection
Piston Shape	Bowl-in piston
IVO/IVC [CAD]*	338.7/570
EVO/EVC [CAD]*	138.25/361.8
Low Idle Speed	800 RPM
Rated Power/Speed	93-129 kW at 2200-2400 RPM

* 0 CAD is the TDC compression/firing

3.2 Optical Engine- Setup

Optical engine experimental setup consists of a single-cylinder engine with extensive optical access. The engine is based on a 4-cylinder, 4.5-Liter interim Tier 4 industrial direct injection turbocharged diesel engine (John Deere, Model 4045-HFC93). Similar to the metal engine setup, two low-pressure NG injectors (Rail Spa, Model IG7 Navajo) injected NG into the intake manifold just before the intake valves. The OEM common rail fueling system delivered the diesel fuel to the injector via a custom extended high-pressure line. Figure 4 shows the optical engine experimental setup without the engine controller and camera in place, Figure 5 shows a visual schematic of the entire laboratory setup, and key engine parameters are provided in Table 3. Supply intake air, delivered by an oil-free screw air compressor (Atlas Copco, Model ZT1), was pre-filtered for condensate (Quincy, Model QCF 300) and for particulates (Quincy, Model QPF 300), then passed to an air chiller (Quincy ECODRI QED250) to remove most of the remaining moisture, and finally supplied to two holding tanks (240+300 gallon) with enough capacity to ensure a constant pressure air reservoir. Commercial software (ERTUNE) controlled the air flow to the cylinder via a pneumatic volume booster (Fairchild, Model 4918A) and an electropneumatic actuator (TESCOM, Model ER5000SI-1). The air flow was measured using a calibrated sonic nozzle (Flow Systems Inc., Critical Flow Venturi, d = 0.167 inch). As the compression ratio of the optical engine (13:1) is much lower than that of the production engine (17:1), a 45-kW air heater (Watlow, Model CFPNA47R5XSJHJ) heated the supply air to 91°C ± 10°C, which, together with the pressurized intake (1.94 bar ± 0.04 bar), created in-cylinder conditions at the start of diesel injection similar to those in the metal engine. External coolant and lubrication systems maintained

the engine block, cylinder liner, and cylinder head at normal operating temperatures (~90 C° for the coolant temperature in the cylinder liner and ~80 C° for the lubrication oil).

Table 3- Optical Engine Parameters

Engine Type	Single Cylinder 4-Stroke Diesel with Optical Access
Engine Make and Model	John Deere 4045-HFC93
Bore and Stroke [mm]	106x127
Displacement [L]	1.125
Geometric Compression Ratio	13:1
Dynamic Compression Ratio	~10:1
Fuel System Diesel/NG	Common Rail Direct Injection/ Port Fuel Injection
Piston Shape	Bowditch /Bowl-In Piston
IVO/IVC [CAD]	343.4/565.2 ATDC compression
EVO/EVC [CAD]	138.25/361.8 ATDC compression
Air System	Externally Fed Dry Compressed Air

The control software mentioned in Section 3.1 was modified to allow skip-fire control of both the diesel and NG injectors and provide the triggers for image acquisition. The one fired cycle followed by nine non-fired cycles skip-fire ratio was selected to protect the optical engine components. Table 4 specifies fuels properties used in optical engine experiments. The Appendix lists further details of key engine experiment sensors.

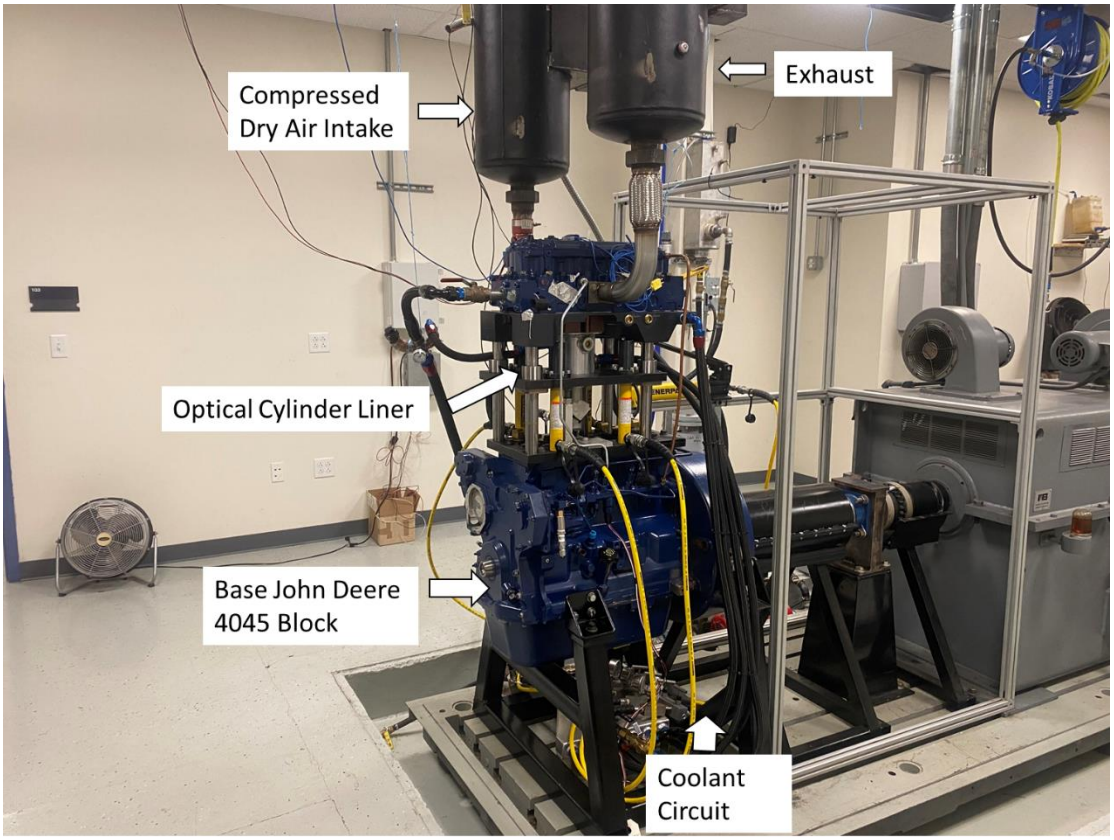

Figure 4- Optical Engine Experimental Setup

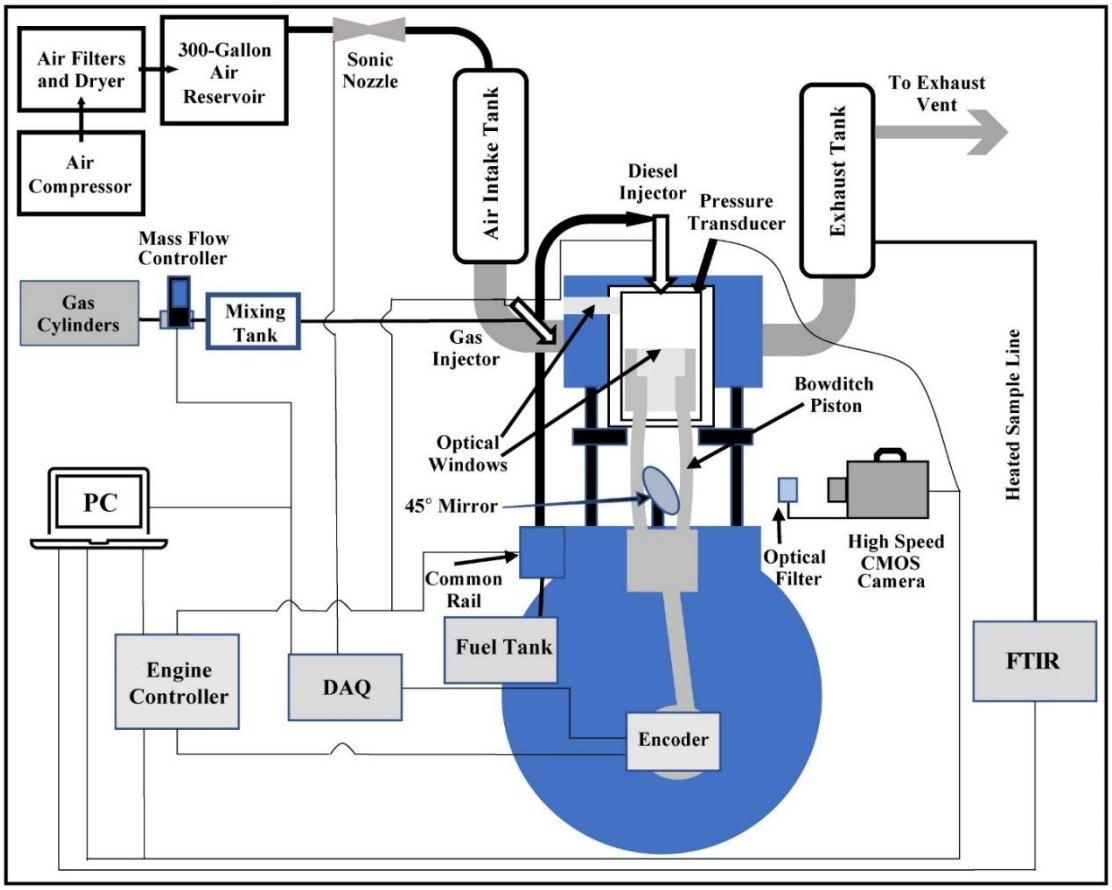

Figure 5- Optical Engine Schematic

Table 4-Optical Engine Fuel Properties

Fuel	MW [kg/kmol]	LHV [MJ/kg]	AFR Mass	Density [kg/m^3]	Net ϕ
Diesel	170	42.8	14.5	810	0.17
Methane	16.04	49.9	17.12	0.67	0.46
Ethane	30.06	47.2	15.99	1.24	0.47
Propane	44.08	46.4	15.58	1.84	0.48

Testing was conducted at low load conditions and low speed (~25% rated maximum IMEP and 1000 RPM). The diesel injection timing was selected to produce two distinct combustion regimes:

a SOI_{DIESEL} of -40 CAD ATDC resulted in RCCI mode, and a SOI_{DIESEL} of -8 CAD ATDC resulted in traditional mixing-controlled compression ignition (MCCI) mode. Preliminary experiments determined that a SOI_{DIESEL} of -40 CAD ATDC was optimum in terms of efficiency for the RCCI type of combustion mode, when the diesel injection mass per cycle and injection pressure were 28 mg/injection and 500 bar, respectively. Preliminary tests conducted on the optical engine at 1000 bar diesel injection produced excessive pressure rise rates which could damage optical components; thus, experiments were carried out at 500 bar diesel injection. MCCI was used to give direct comparison to the results of the metal engine configuration. The maximum gas mass per cycle before the rate of pressure rise reached extreme levels was the equivalent of 2100 J/injection (42 mg, 44 mg, and 46 mg of C_1, C_2, and C_3, respectively). Therefore, as the diesel energy per cycle was ~1192 J/injection, diesel energy substitution rate (ESR) in this study was ~63%, and $\phi \approx 0.3$ for the delivered gaseous air-fuel mixture. Pure components of NG replaced part of the diesel energy to visualize the maximum distinction between the gaseous fuels, thus creating a baseline optical data set for future testing with mixtures of the components which would likely have a higher degree of similarity. The intake boost pressure was set to 28 PSIA for experiments which resulted in a significantly higher NG fuel slip rate through the exhaust. For this reason, the NG fuel energy delivered over-estimates the actual in-cylinder conditions.

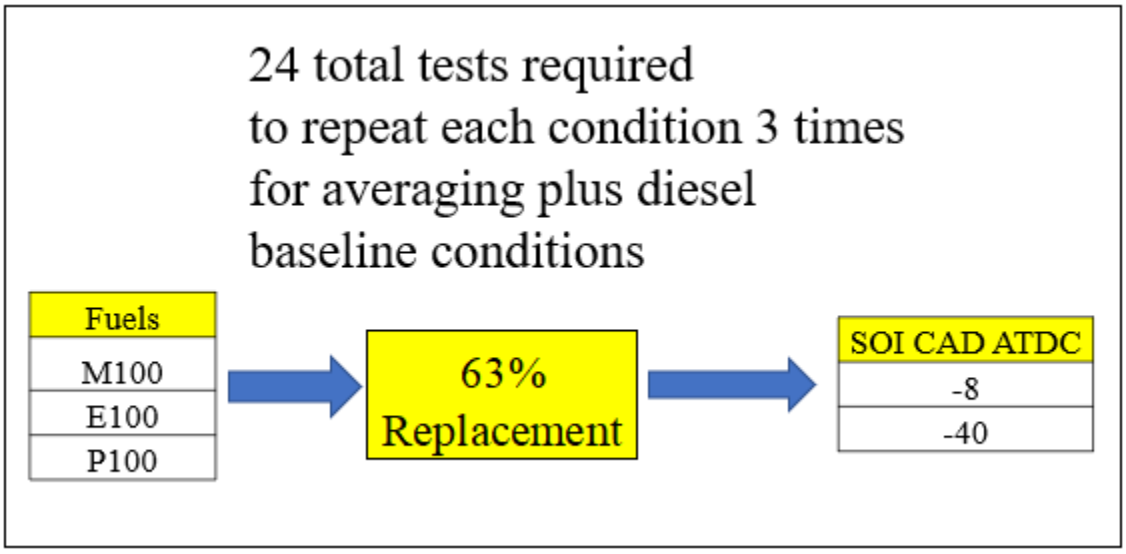

Figure 6- Optical Engine Experimental Test Matrix

After motoring the optical engine for one minute while also injecting the gaseous fuel to allow the gas flow meter to stabilize [65], ~50 fired cycles were collected and used for averaging pressure

data. The coefficient of variation (COV) of IMEP was below 3% for all the dual-fuel cases, which suggested repeatable combustion cycles despite the less optimal combustion chamber of the optical engine. Each operating condition was repeated three times. MATLAB© was used to post-process the experimental data. In-cylinder pressure analysis used the average cycle value. Emissions calculations followed the CFR part 1065 methodology. Only nitric oxide (NO) emissions were reported here due to the insignificant levels (1-5 ppm) of nitrogen dioxide (NO_2). No exhaust soot measurements were performed.

Image Acquisition and Processing

A high-speed CMOS camera (Photron, Model Fastcam SA5) fitted with a 50-mm f-1.4 Nikon lens, recorded in-cylinder natural luminosity (NL) during the fired cycles. NL refers to the combustion broadband light emitted during a fired cycle [111]. As seen in Figure 5, a 45° mirror (Edmund Optics, Model 43579), mounted under the piston, reflected the NL that passed through the fused-silica piston window to the camera lens. The start of image acquisition was synchronized with the diesel injection timing to ensure that recorded data contains all the flame stages, from inception to end of combustion. The camera was operated at 30,000 frame-per-second (fps), which corresponded to one frame every 0.2 CAD at an engine speed of 1,000 RPM. The maximum image resolution at this framing rate was 320 × 264 pixels, which resulted in a 0.313 mm/pixel resolution. The camera exposure times was set to 13.33 μs (1/75,000 s) to avoid Nyquist sampling issues. As NL increases several orders of magnitude throughout combustion (especially when soot is present) and the exposure time cannot be modified during image acquisition, this approach can result in saturated pixels even at the largest lens f-number. A short-pass filter (Schott KG3) and, if needed, a neutral density filter, was placed in front of the camera for high transmission in the visible and high absorption in the IR ranges.

Figure 7 shows an example of image processing. Figure 7a shows the non-firing image (acquired at camera settings that maximize feature extraction) that was used to identify the area of interest for the combustion visualization (i.e., the piston bowl area as seen from below the piston) Then, as shown in Figure 7b, the location of the intake and exhaust valves, pressure transducer, and injector nozzle, and the direction of the six diesel sprays as they exit the nozzle, respectively, were superimposed for analysis clarity. The circle mask in Figure 7c eliminated from image analysis everything outside the area of interest. After background subtraction, the intensity of each pixel

was scaled from no signal to maximum pixel saturation signal (as seen in Figure 7d) to (i) help identify and separate the premixed flame/oxidation regions (associated with the low signal intensity) from those of high signal intensity, associated with soot radiation, and (ii) compute the spatially integrated NL (SINL), which is a measure of the instantaneous flux of natural luminosity over the entire field of view and correlates with the intensity of the combustion activities captured by the camera. As one of the benefits of dual-fuel diesel-gas combustion is the significant reduction in particulate emissions, images such as that in Figure 7d allows us to also quantify the soot reduction, as the soot fraction is proportional to signal intensity in the natural luminosity images.

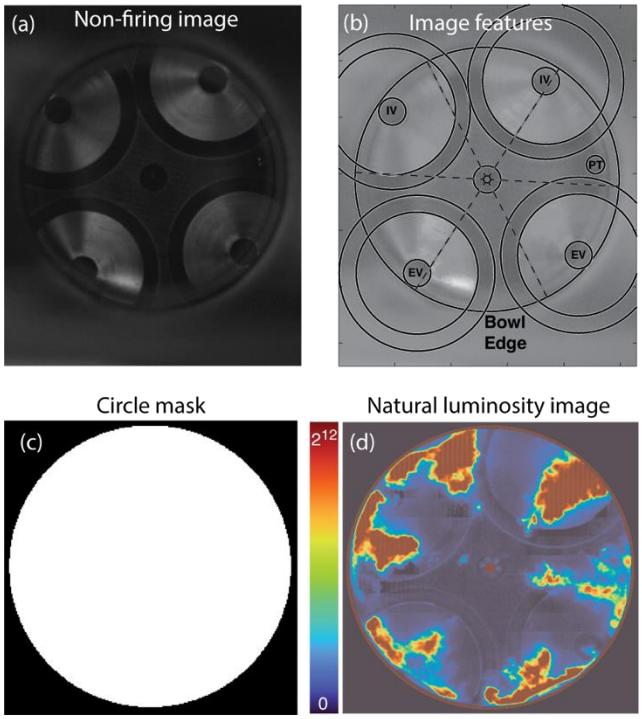

Figure 7- Combustion Image Processing: (a) Non-Firing Image used to Determine the Area of Interest; (b) Non-Firing Image with the Most Important Chamber Features Superimposed: the Bowl Edge, the Location of the Intake Valves (IV) and Exhaust Valves (EV), the Location of the Pressure Transducer (PT), the Position of the Injector Nozzle, and the Direction of the Six Diesel Sprays as They Exit the Nozzle; (c) the Mask used to Separate the Image Area of Interest; and (d) an Example of Combustion Natural Luminosity. The Color Scale Shows the Intensity of the Light (Max 212) as Seen when Visualized From Under the Transparent Piston.

3.3 Burner Experimental Setup

The experimental setup consisted of methane, ethane, propane, butane, and air bottles with flow pressures regulated to 18.5 PSIA. The fuel and air passed separately through mass flow meters and/or mass flow controllers (AliCat), where the flow pressure, temperature, and volumetric flow rate were measured. The fuel and air then entered a mixing chamber, followed by a pulsation tank/secondary mixing chamber before entering a flame arrestor then passing to the burner tube. All gas lines before the flame arrestor were made from Teflon tubing with an inside diameter of $1/8^{th}$ inch. To ensure accurate flow rate measurements, fuel and air lines were checked for leaks prior to each testing day using leak detector (Snoop). A schematic of the experimental setup is shown below in Figure 8 (left), and picture of the laboratory setup in Figure 8 (right). The exhaust hood (seen above the burner tube) removes flue gas from the laboratory at a low flow rate to avoid disturbing the flame structure but enough to completely exhaust the combustion products.

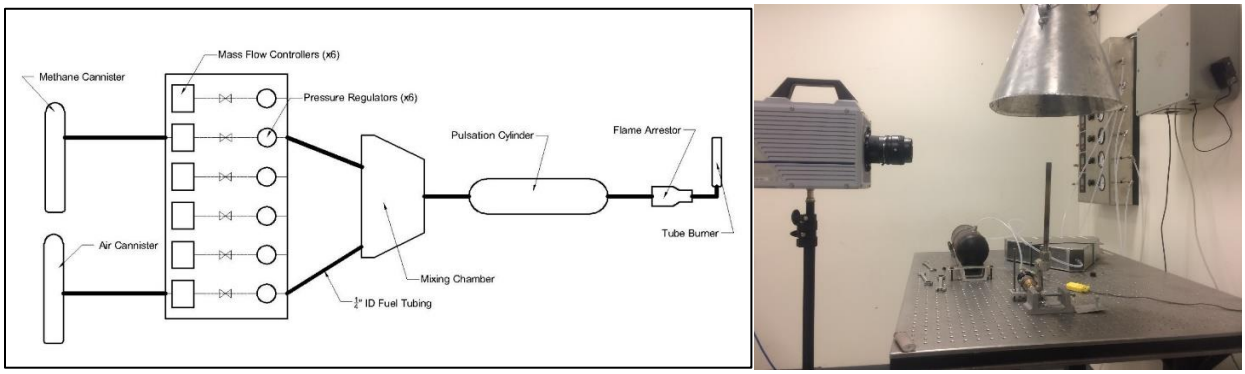

Figure 8-Burner Experimental Setup

3.4 Data Processing

3.4.1 Engine Calculations

The collected engine data was post-processed using MATLAB©. Pressure data was filtered and analyzed to determine indicated performance and heat release rates. The following equations were used in engine data analysis.

$Cylinder\ Volume \quad V = V_c\left\{1+\frac{1}{2}(r_c-1)\left[R+1-\cos\theta-(R^2-\sin^2\theta)^{1/2}\right]\right\}$	(1)
$Displacement\ Volume \quad V_d = \frac{\pi}{4}B^2L$	(2)
$Apparent\ Heat\ Release\ Rate \quad \frac{dQ}{dt} = \frac{\gamma}{\gamma-1}P\frac{dV}{dt}+\frac{1}{\gamma-1}V\frac{dP}{dt}$	(3)
$Brake\ Power \quad P_b[kW] = \frac{(Torque[ft\cdot lb]\cdot N[RPM])\cdot 0.745}{5252}$	(4)
$Indicated\ Power \quad P_i[kW] = \frac{(IMEP)(V_d)(N)}{6000}$	(5)
$Brake\ Specific\ Fuel\ Consumption \quad bsfc = \frac{\dot{m}_f\cdot 60\cdot 1000}{P_b}$	(6)
$Brake\ Thermal\ Efficiency \quad \eta_{th,brake} = \frac{P_b}{\dot{m}_f LHV}$	(7)
$Equivalence\ Ratio \quad \phi[-] = \frac{\frac{NG_{SLPM}\cdot AFR_{NG,stoich}\cdot\rho_{CNG}}{60000}+Diesel_{g/s}\cdot AFR_{Diesel,stoich}}{\frac{MAF_{SLPM}}{60000}\cdot\rho_{AIR}}$	(8)
$Fuel\ Energy \quad \dot{E}_{in} = \frac{(LHV_{CNG})(NG[SLPM])(\rho_{CNG})}{60000}+\frac{(LHV_{Diesel})(Diesel\left[\frac{g}{s}\right])}{1000}$	(9)
$Percent\ Diesel\ Substitution \quad ESR = \frac{\dot{E}_{NG}}{\dot{E}_{NG}+\dot{E}_{Diesel}}$	(10)
$Indicated\ Thermal\ Efficiency \quad \eta_{th,i} = \frac{P_{i,avg}}{\dot{E}_{in}}\cdot 100\%$	(11)

Emission calculations were performed using a CFR part 1065 graphical user interface program developed at WVU. NMHC emissions were determined from the difference between THC and methane measurements. NO_2 and NO emissions were combined during post processing of the data to produce a single NO_x value for metal engine experiments. Only NO was reported for optical engine experiments due to insignificant levels of NO_2 (<5 ppm). The emission values were calculated with respect to brake power.

Brake Specific NO_x	$BSNO_X = \frac{\dot{m}_{NO_X}}{P_b}$	(12)
NO_x Mass Flow	$\dot{m}_{NO_X} = \frac{NO_x[ppm]}{10^6} \cdot 38\left[\frac{g}{mol}\right] \cdot \dot{n}_{exh}[\frac{mol}{s}] \cdot Kh$	(13)
NO_x Sample	$NO_x[ppm] = FTIR_{NO_{PPM}} + FTIR_{NO2_{PPM}}$	(14)
THC Sample	$THC[ppm] = FTIR_{CH4_{PPM}} + FTIR_{NMHC_{PPM}}$	(15)
Brake Specific THC	$BSTHC = \frac{\dot{m}_{THC}}{P_b}$	(16)
THC Mass Flow	$\dot{m}_{THC} = \frac{THC\ [ppm]}{10^6} \cdot 17.60\frac{g}{mol} \cdot \dot{n}_{exh}[\frac{mol}{s}]$	(17)
Brake Specific CO	$BSCO = \frac{\dot{m}_{CO}}{P_b}$	(18)
CO Mass Flow	$\dot{m}_{CO} = \frac{CO\ [ppm]}{10^6} \cdot 28\frac{g}{mol} \cdot \dot{n}_{exh}[\frac{mol}{s}]$	(19)
Brake Specific CO_2	$BSCO_2 = \frac{\dot{m}_{CO2}}{P_b}$	(20)
CO_2 Mass Flow	$\dot{m}_{CO2} = \frac{CO_2[\%]}{100} \cdot 44\frac{g}{mol} \cdot \dot{n}_{exh}[\frac{mol}{s}]$	(21)
Brake Specific CH_4	$BSCH_4 = \frac{\dot{m}_{CH4}}{P_b}$	(22)
CH_4 Mass Flow	$\dot{m}_{CH4} = \frac{CH_4\ [ppm]}{10^6} \cdot 16.04\frac{g}{mol} \cdot \dot{n}_{exh}[\frac{mol}{s}]$	(23)
Brake Specific CO_2 Equivalent	$BSCO_2$ *Equivalent* = $BSCO_2$ + *(28· $BSCH_4$)+(6· BSC_2H_6)+(3· BSC_3H_8)+(4· BSC_4H_{10})* [40]	(24)
Gas Emission only Brake Specific CO_2 Equivalent	$BSCO_2$ *Equivalent C_1-C_4 Contribution* = *(28· $BSCH_4$)+(6· BSC_2H_6)+(3· BSC_3H_8)+(4·C_4H_{10})*	(25)
Ringing Intensity	$RI = \frac{1}{2\gamma} * \frac{\left(\beta\left(\frac{dP}{dt}\right)_{max}\right)^2}{P_{max}} * \sqrt{\gamma R T_{max}}$ (where β=0.05 ms)	(26) [112]

$relative\ CH_4 = \left(\frac{\frac{CH_4(blend)}{CH_4(M100)} - CH_4\ mass\ fraction}{CH_4\ mass\ fraction}\right) * 100\%$	(27)
$Fraction\ of\ Gas\ Burned \quad NG\ MFB\ (\%) = \left(1 - \frac{C_{i,firing\ (ppm)}}{C_{i,non-firing\ (ppm)}}\right) \times 100\%$, $where\ i = 1,2,3$	(28)
$Modified\ Energy\ Substitution\ Rate\ (\%) = \left(\frac{\frac{NG\ MFB\ \%}{100}\dot{E}_{NG}}{\left(\frac{NG\ MFB\ \%}{100}\dot{E}_{NG}\right)+\dot{E}_{Diesel}}\right) \times 100\ \%$	(29)
$Emission\ Correction\ Factor = -1^{-8}HC_{ppm}{}^3 + 5^{-6}HC_{ppm}{}^2 + 5^{-4}HC_{ppm} + 1.0011$	(30)

3.4.2 Burner Calculations

Laminar flame burner consisted of a tube with inner diameter of $^7/_{16}$ inch and outer diameter of ½ inch. The tube length minimum for testing must be 10 times the inner diameter of the pipe to ensure fully developed flow. The density and viscosity of air and fuel used by AliCat flow measurement devices are taken at the standard reference of 25°C and 14.70 PSIA [113]. For any given measured standard volumetric flowrates (Q) of gas blend and air, the mass flow rate ($\dot{m}$) was determined. Individual mass flow rates of the components are used in order to calculate a mass weighted mixture viscosity and density. The exit velocity and Reynold's number of the mixture was determined using Equations 31 and 32, respectively.

The air-fuel ratio and equivalence ratio of the mixture was determined by the ratio of mass flow rates inside a LabView sub-VI (Appendix A, Figure 73), which calculated the stoichiometric chemical balance for the current fuel mixture composition which was then compared to the current air supply. This allows for continuous monitoring of the equivalence ratio of any C_1-C_4 fuel mixture in real-time as experiments are being conducted. For example, the air/fuel equivalence ratio (λ) is determined as the ratio of actual air/fuel ratio normalized to the stoichiometric value 17.2 for methane/air combustion. The fuel-air equivalence ratio (ϕ) is the inverse of λ and is the parameter reported for comparison with literature. All parameters described in Equations 28-32 are calculated in LabView. The timeseries data is collected using analog/digital data acquisition modules (ICP-CON, Model PET-7016 CR) and K-Type thermocouples for temperature

measurements, one mass flow controller (AliCat, Model MCP-100SLPM) as well as 5 flowmeters for gas flow measurement (AliCat, Model M-5SLPM-RD (gases C_2-C_4)). ϕ is calculated by the software, then monitored and maintained at a set value for each test. New mixtures are allowed at least 5 minutes for stabilizing the air/fuel ratio within the mixing chamber and pulsation tank. Images of the flame are taken using a high-speed camera (Photron, Model Fastcam SA5) coupled to an adjustable lens (Nikon, Model AF NIKKOR 50 mm, 1:1.4 D). The camera was operated at 1024x1024 resolution with a frame rate of 7000 frames per second [114]. The images were post processed alongside the time series data to determine S_L and flame angle of the mixture. MATLAB© image processing was utilized in determining flame dimensions.

Mixture Velocity	$V_{mix} = \frac{\dot{m}_{mix}}{\rho_{mix} A_{exit}}$	(31)
Reynold's Number	$Re = \frac{\rho_{mix} V_{mix} D_{exit}}{\mu_{mix}}$	(32)
Actual Air Fuel Ratio	$AFR_{actual} = \frac{\dot{m}_{air}}{\dot{m}_{fuel}} = \frac{\rho_{air,st} Q_{air,slpm}}{\rho_{CH4,st} Q_{CH4,slpm}}$	(33)- methane case
Relative Air Fuel Ratio	$\lambda = \frac{AFR_{actual}}{AFR_{stoichiometric}} = \frac{AFR_{actual}}{17.2}$	(34)- methane case
Equivalence Ratio	$\phi = \frac{1}{\lambda}$	(35)
Laminar Flame Speed	$S_L = \sqrt{\frac{{V_{mix}}^2}{\left[\left(\frac{2 * x_{F,0}}{b}\right)^2 + 1\right]}}$	(36)
Flame Angle	$\alpha = \tan^{-1}\left(\frac{b}{2x_{F,0}}\right)$	(37)
Mass Flow Uncertainty	$\Delta Q = \pm(0.008 * Q_{measured} + 0.01)$	(38)- for 0-5 slpm flow meter

S_L and the flame angle were calculated based on Heinz Pitsch's G-equation based solution to the slot burner flame geometry, Equations 36 and 37 [115]. Critical measurements for analysis are the mixture velocity at the tube exit, V_{mix}, the width of the tube or flame base width, b, and the location of the flame tip, $X_{F,0}$. Figure 9 below shows an example of how the height of the flame tip was

determined using a pixilated reference to the tube OD. In this case, the flame base width was observed to expand out to the tube OD, thus (b) was equal to the tube OD for analysis. Using the given mass flow controller uncertainty in Equation 38 along with Equations (39-44) the uncertainty in S_L and ϕ was determined. It should be mentioned that the error associated with $X_{F,0}$ was considered to be negligible (roughly 0.21% error) compared with the error in mixture flow velocity.

Mass Flow Uncertainty	$\Delta\dot{m}_i = \rho\Delta Q_i$	(39)
Air Fuel Ratio Uncertainty	$\Delta AFR = \sqrt{\left(\frac{\Delta\dot{m}_a}{\dot{m}_f}\right)^2 + \left(\frac{-\dot{m}_a\Delta\dot{m}_f}{\dot{m}_f{}^2}\right)^2}$	(40)
Equivalnce Ratio Uncertainty	$\Delta\phi = \frac{AFR_{st}\Delta AFR}{AFR^2}$	(41)
Mixture Mass Flow Uncertainty	$\Delta\dot{m}_{mix} = \sqrt{(\Delta\dot{m}_a)^2 + \left(\Delta\dot{m}_f\right)^2}$	(42)
Mixture Velocity Uncertainty	$\Delta V = \frac{\Delta\dot{m}_{mix}}{\rho A}$	(43)
Laminar Flame Speed Uncertainty	$\Delta S_L = \sqrt{\frac{1}{\left(\frac{2x_F}{b}\right)^2 + 1}} * \Delta V$	(44)

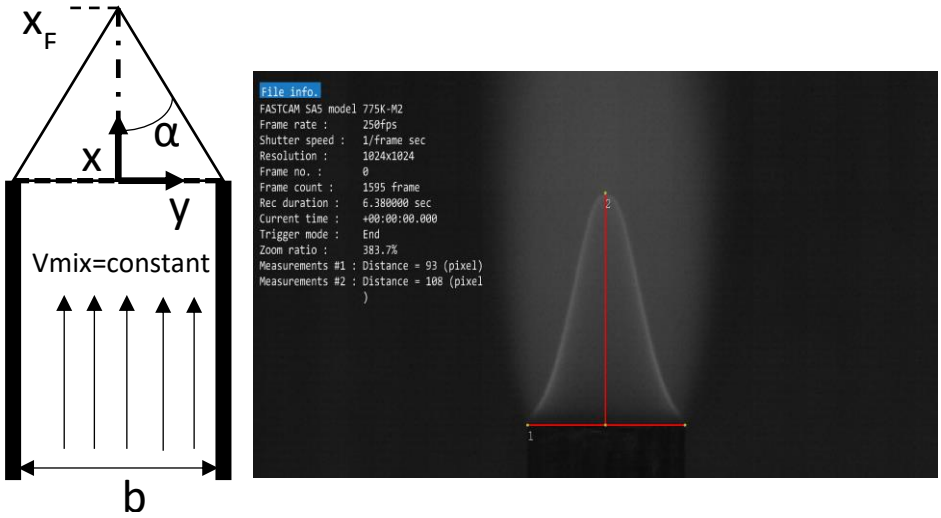

Figure 9- Image Data

3.5 Fuel Properties

Fuel properties influence combustion in numerous ways. Physical properties such as density, viscosity, heating value, and stoichiometric air-fuel-ratio, and flame speed are primary factors when comparing the effects of fuel composition. The design of experiments compared the effects of different components in the C_1-C_4 mixture on the overall performance and emissions of the dual-fuel engine. The mixtures were kept within the naturally occurring ranges found across the globe and described in literature [29]. Table 5 shows some of the physical properties of the fuels investigated here. Table 6 details the naming convention of gas blends used for burner laminar flame speed experiments and metal engine experiments. The gas blends are described by their name following a notation of M for C_1, E for C_2, P for C_3, and B for C_4 then followed by the molar (volumetric) percentage of each fuel in the gas blend. For example, M90E10 represents a blend with 90% by volume methane and 10% by volume ethane.

The initial design of experiments for this work included C_5 addition to the fuel compositions. As C_5 is liquid at ambient laboratory conditions, a method of heating ~~the~~ C_5 in a small tube and extracting the vapor was devised. However, the C_5 flow was not constant and depleted rapidly. A second method was conceived to use a drip delivery system into the engine intake manifold and measure the consumption using a fuel scale. This method would work in delivering the fuel but created issues with controlling the precise volume fraction for a given fuel blend (other components measured could be controlled more accurately). For this reason, the C_5 was withheld from experimental fuel compositions and limited the blends to C_1-C_4.

Table 5- Fuel Properties

Fuel	CH_4	C_2H_6	C_3H_8	C_4H_{10}	Diesel
Energy content [MJ/kg]	49.9	47.2	46.4	45.3	42.8
Density at 20°C 1 bar [kg/m3]	0.66	1.24	1.84	2.49	810
Molecular weight [kg/kmol]	16.04	30.07	44.10	58.12	170
A/F ratio	17.2	16.0	15.7	15.4	14.5
Liquid density [kg/m3]				580	830

Table 6- Naming Convention of Fuel Mixture Compositions Examined

Mix Name	Methane (molar %)	Ethane (molar %)	Propane (molar %)	Butane (molar %)
M100	100	0	0	0
M90E5P5	90	5	5	0
M90E5B5	90	5	0	5
M80E10P10	80	10	10	0
M90E10	90	10	0	0
M90P10	90	0	10	0
M90B10	90	0	0	10

Mixture Name	LHV [kJ/kg]	AFR Mass	Density [kg/m^3]	WI [kJ/kg]	MN	Propane Knock Index	Knock Rating	CO_2 ratio [kg CO_2/kg fuel]	S_L [cm/s]
M100	50000	17.12	0.67	74600	100	0	good	2.74	38.22
M90E5P5	49400	16.83	0.76	68800	72	6.1	bad	2.79	39.87
M90E5B5	49200	16.75	0.79	67100	57	16	bad	2.80	NA
M80E10P10	48900	16.61	0.85	64200	63	12	bad	2.83	41.15
M90E10	49600	16.92	0.73	70700	81	2.9	good	2.78	38.82
M90P10	49100	16.75	0.79	67100	66	10	bad	2.80	41.05
M90B10	48800	16.61	0.85	64100	<46.8	30	bad	2.83	NA

Table 7 details other critical fuel properties and attributes such as differences in gas blend LHV, AFR, density, WI, MN, propane knock index and rating [116], potential CO_2 differences, and laminar flame speed used by common models. It should be mentioned that the GRI MECH III - based laminar flame speed at atmospheric conditions [117] varies inversely with the LHV, WI, and MN of the gas blend but varies directly with the molecular weight (MW), density, and propane knock index of the gas blend.

Mixture Name	LHV [kJ/kg]	AFR Mass	Density [kg/m^3]	WI [kJ/kg]	MN [116]	Propane Knock Index [116]	Knock Rating [116]	CO_2 ratio [kg CO_2/kg fuel]	S_L [cm/s] [117]

M100	50000	17.12	0.67	74600	100	0	good	2.74	38.22
M90E5P5	49400	16.83	0.76	68800	72	6.1	bad	2.79	39.87
M90E5B5	49200	16.75	0.79	67100	57	16	bad	2.80	NA
M80E10P10	48900	16.61	0.85	64200	63	12	bad	2.83	41.15
M90E10	49600	16.92	0.73	70700	81	2.9	good	2.78	38.82
M90P10	49100	16.75	0.79	67100	66	10	bad	2.80	41.05
M90B10	48800	16.61	0.85	64100	<46.8	30	bad	2.83	NA

Table 7- Fuel Properties of Mixtures Examined

The mass fractions of each fuel component in the different blends are presented in Table 8. This information was provided to help differentiate the impact of methane emissions in the results section due to emission values being presented by mass.

Table 8- C_1-C_4 Mass Fractions in the Gas Blend

Mixture Name	C_1 mass fraction	C_2 mass fraction	C_3 mass fraction	C_4 mass fraction
M100	1	0	0	0
M90E5P5	0.794	0.083	0.123	0
M90E5B5	0.761	0.079	0	0.160
M80E10P10	0.631	0.149	0.220	0
M90E10	0.827	0.173	0	0
M90P10	0.763	0	0.237	0
M90B10	0.705	0	0	0.295

4 Results/Discussion

4.1 Burner Experiments

Figure 10 shows S_L measurements versus ϕ against those mentioned in literature. Data consistency was shown by repeating the experiments twice, matching flowrates with near equal ϕ's. Repeated experiments show agreement with each other. The experimental data points show best agreement with literature data from Aung 1995 and Hassan 1998 [25-26]. For the ϕ range of 0.9-1.2 the current data reflects the same trend as literature showing an average deviation of 6.5%. Within this range, the maximum deviation (13.5%) occurs for ϕ of 0.9 [27]; however, results deviated only 2.0% from data reported by Aung [25]. A strong deviation of 70.7% occurred for ϕ of 1.4 with data reported in Vagelopoulous et al [27], but reference [27] also disagrees with the data reported

by Aung [25]. The error analysis, Equations 41 and 44, was used to determine the experimental error associated with data in the figure.

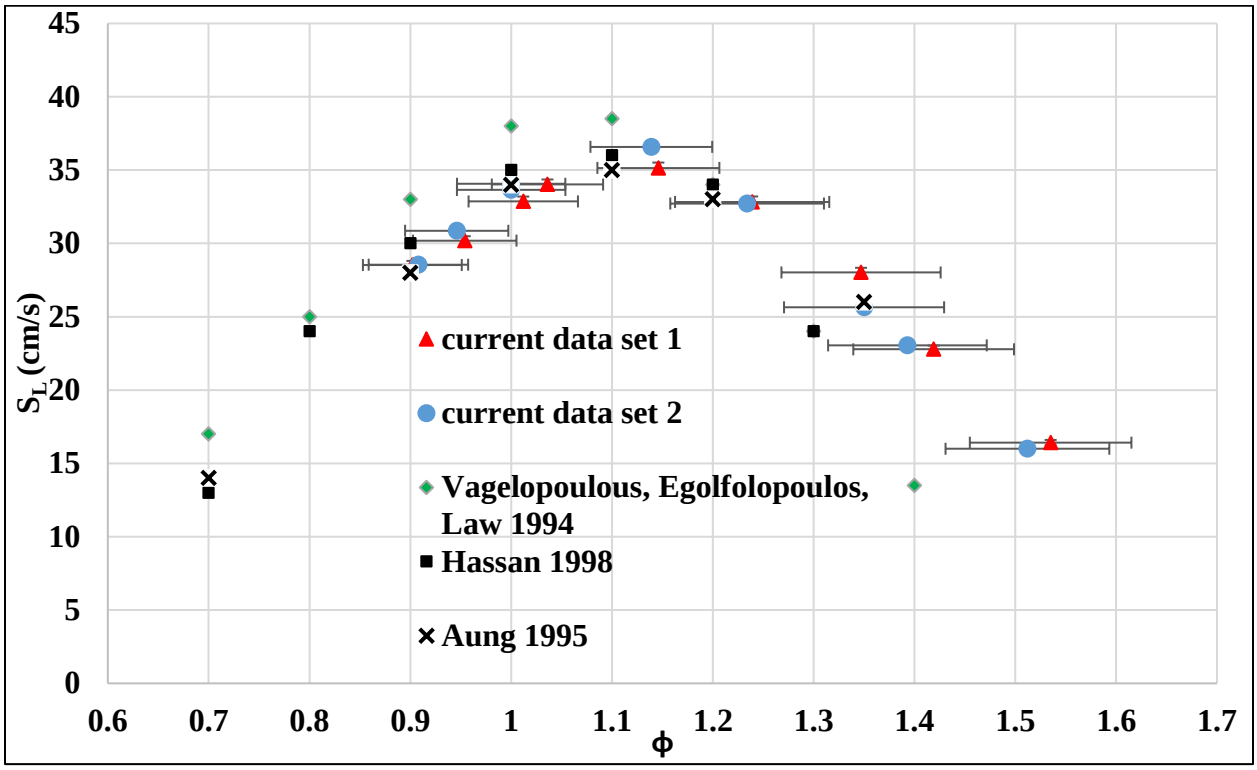

Figure 10- Methane Laminar Flame Speed (Burner Method)

The consistency of data acquisition was analyzed by performing a series of experiments within a small range of ϕ's (1.05-1.10). The data differs in overall mass flow rate of the mixture while maintaining a similar ϕ. Consistency of the data was sufficient, having an apparent S_L variation of less than 1% for the two points with equal ϕ. For the burner experimental setup higher uncertainty was shown in regard to ϕ determination than S_L calculations.

While this method of flame speed analysis is known to have limitations with respect to determining the most accurate flame speed value, it provides a platform for comparison of the C_1-C_4 mixtures of interest. The relative change in laminar flame speed with respect to methane will be the target of the investigation to help possibly explain any differences in performance noticed under dual-fuel engine testing. The relative change in flame speed may also be noticeable in initial flame propagation data under optical investigation.

Results from the initial verification with CH_4 show that this approach in laminar flame speed measurement is adequate in determining flame speed within a few percent deviation from

literature. The same experimental procedure was conducted on the other six gas blends to compare the compositional effects of the blends under atmospheric conditions and is shown in Figure 11. The data for M100 agrees well with the original data from Figure 10. The flame speed for other gas blends shows a slightly unexpected trend (i.e., certain gas blends did not show a smooth curve as expected). M90P10 and M90B10 in particular show deviation from this trend near equivalence ratio of 1.2. Also, the data shows the increased number of flow meters used in data collection substantially increases the uncertainty in equivalence ratio as a compounding result of each individual mass flow meters' device uncertainty (0.8 % reading ± 0.2% full scale). As a result, tertiary gas mixtures show the highest uncertainty followed by binary gas mixtures. In the case of tertiary gas mixtures, the uncertainty can be as high as 20% of the nominal equivalence ratio when using the flow meter near the minimum flow. For more accurate results it would be necessary to use gas chromatography (GC) calibrated gas blends to eliminate this uncertainty.

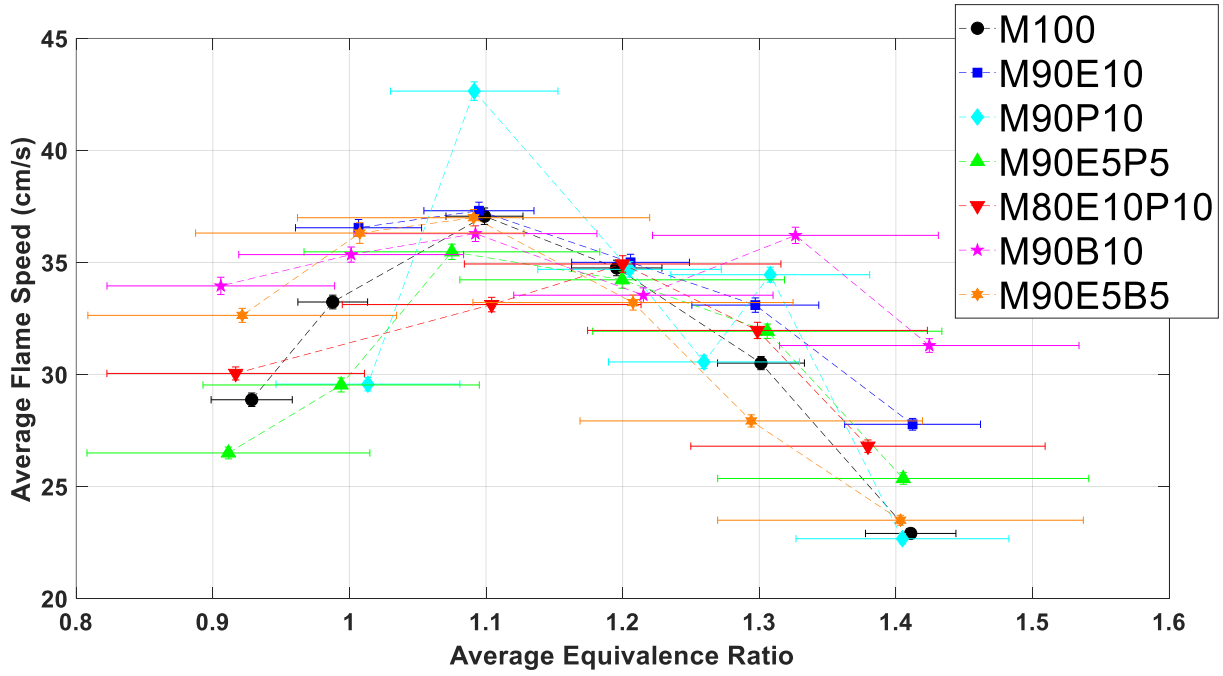

Figure 11- Effect of Gas Composition on the Laminar Flame Speed Measured in the Burner Experiments (P=1 atm and T=300K)

4.2 Baseline Diesel Experiments – Metal Engine

Experiments targeted an input fuel energy rate of 63.2 kW, which, for diesel-only operation, was the equivalent of 1.48 g/s of diesel fuel, delivered via a single 0.8-ms fuel injection at 1000 bar.

At 1000 RPM, it resulted in a low load (25 kW brake power, or roughly 25% of the rated intermittent power, and 40% fuel conversion efficiency) [118]. All energy replacement plots in the next sections refer to this diesel-only baseline condition when discussing the relative changes in performance and emissions. NG flow requirements were then calculated for 40% energy replacement under dual-fuel operation. The lowest baseline diesel brake specific fuel consumption (BSFC) without EGR was 219.4 g/kWh for SOI_{DIESEL} = -4 CAD ATDC. This is consistent with literature for a similar engine which reported minimum BSFC around 227 g/kWh for SOI_D -5 ATDC at 1400 RPM [41].

Figure 12 compares the average in-cylinder pressure when the metal engine operated without EGR or with the EGR valve opened at 30%, at SOI_{DIESEL} from -12 CAD ATDC to TDC. A continuous decrease in in-cylinder pressure is observed as the EGR rate is increased. The pressure trace is only reported for a baseline indication of combustion conditions with changing start of injection. For clarity, EGR % reported refers to the relative open percentage of the EGR valve position feedback sensor. The EGR % reported here does not represent a mass flow-based percentage of in-cylinder residuals to fresh air.

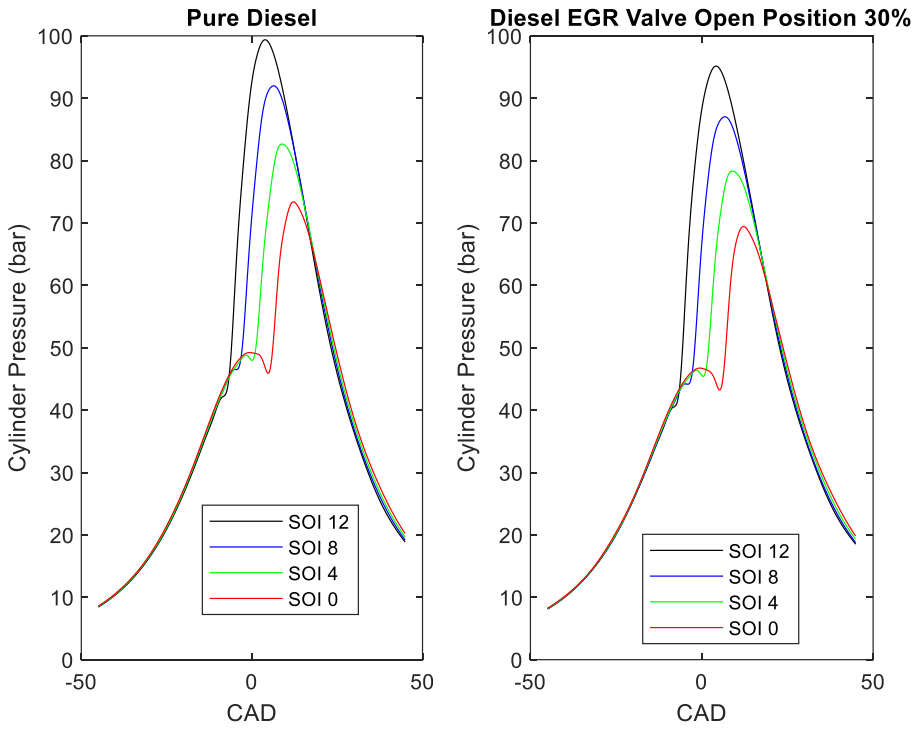

Figure 12- Effect of EGR on Cylinder Pressure for Diesel-only Combustion (Metal Engine, 1000 RPM, $P_{inj,\ diesel}$ = 1000 bar).

4.3 40% Fuel Energy Replacement by Natural Gas Mixtures: Metal Engine

The effect of replacement mixture composition on the dual-fuel diesel-NG engine performance and emissions was investigated at 40% ESR, under different SOI_{DIESEL} timings. As for the NG delivery, the end of NG injection (EOI_{NG}) was maintained constant at 225 CAD BTDC.

Similar to observations in literature, the addition of gaseous fuel increased the ignition delay of dual-fuel operation compared to diesel-only operation. Figure 13 suggests that the resulting increase in ignition delay was due to a delay in the diesel fuel vaporization. While the effect was noticeable for all gas blend compositions, the C_1-C_4 fraction influenced the magnitude of the delay. M100 consistently had the most delay for all SOI_{DIESEL} conditions, followed by M80E10P10 and M90E5P5. The least delay was found consistently for M90B10 over all SOI_{DIESEL} conditions. However, for gas blends with mid-level ignition delay M90E10, M90E5B5, and M90P10 there was also a sensitivity to SOI_{DIESEL} which did not form a general trend among the fuels. A closer

inspection of in-cylinder pressure traces shows that the delay correlated with the up to 3 bar decrease in pressure just before the start of the diesel injection, with M100 showing the lowest in-cylinder pressure at SOI_{DIESEL}. As the differences in intake pressure and temperature between the baseline diesel and the dual-fuel operation mentioned previously are not enough to completely explain the decrease in pressure just before the start of the diesel injection, the data suggests that the increase in vaporization delay was due to the changes in the specific heat of the mixture. A different specific heat will change the polytropic coefficient, hence the change in the temperature and pressure at the end of the compression stroke. This supports the simulation findings in [86]. Then, the actual SOI_{DIESEL} affected the vaporization delay magnitude, with the delay increasing from 1 CAD at SOI_{DIESEL} = - 8 CAD ATDC to 2 CAD at SOI_{DIESEL} = TDC. The additional timing allowed the diesel fuel to penetrate even further inside the combustion chamber, therefore yielding a better air-diesel mixing before ignition. This explains why, even if the combustion process started later than for the baseline diesel case, the pressure increased faster in the dual-fuel mode. Specifically, the maximum rate of pressure rise increased from 7-8 bar/CAD for diesel to 11-14 bar/CAD for the dual-fuel cases, or an almost 80% increase. The lengthened ignition delay results in a more rapid and intense heat release [119]. This substantial increase in the rate of pressure rise is important when considering its effect on the structural integrity of the engine. It also supports the maximum substitution rate of 40-45% mentioned in [9] but, if just the rate of pressure rise is a concern, there are ways to mitigate it, such as the use of EGR to slow the combustion. The substantial increase in the pressure rise at this low load operating condition is also attributed to the high turbulence inside the bowl region of the piston near TDC [120-121], which further accelerates the premixed combustion process (i.e., fast burn). However, the almost parallel pressure lines throughout the fast burn period shown in Figure 13 for each respective fuel suggests that SOI_{DIESEL} did not have a large influence on the rate of pressure rise, for both baseline diesel and dual-fuel operation. With regards to the actual C_1-C_4 percentage effect; M90B10 consistently had the highest maximum in-cylinder pressure. The second highest pressure varied between M90P10 (SOI_{DIESEL} = -8 CAD ATDC), M80E10P10 (SOI_{DIESEL} = -4 CAD ATDC), and M90E10 (SOI_{DIESEL} = TDC) depending on SOI_{DIESEL}. M100 consistently had the lowest maximum pressure. The higher in-cylinder pressure correlated with the autoignition temperature ranking [23] mentioned in the literature except SOI_{DIESEL} at TDC which was likely a consequence increased ignition delay. The most notable difference of all the fuels was the extended burn duration for SOI_{DIESEL} at TDC of

M90B10 which is evident in the continuing increase in pressure after all other gas blends begin to decrease. This strongly suggests the lower auto-ignition temperature allowed for continued combustion after other fuels began to quench.

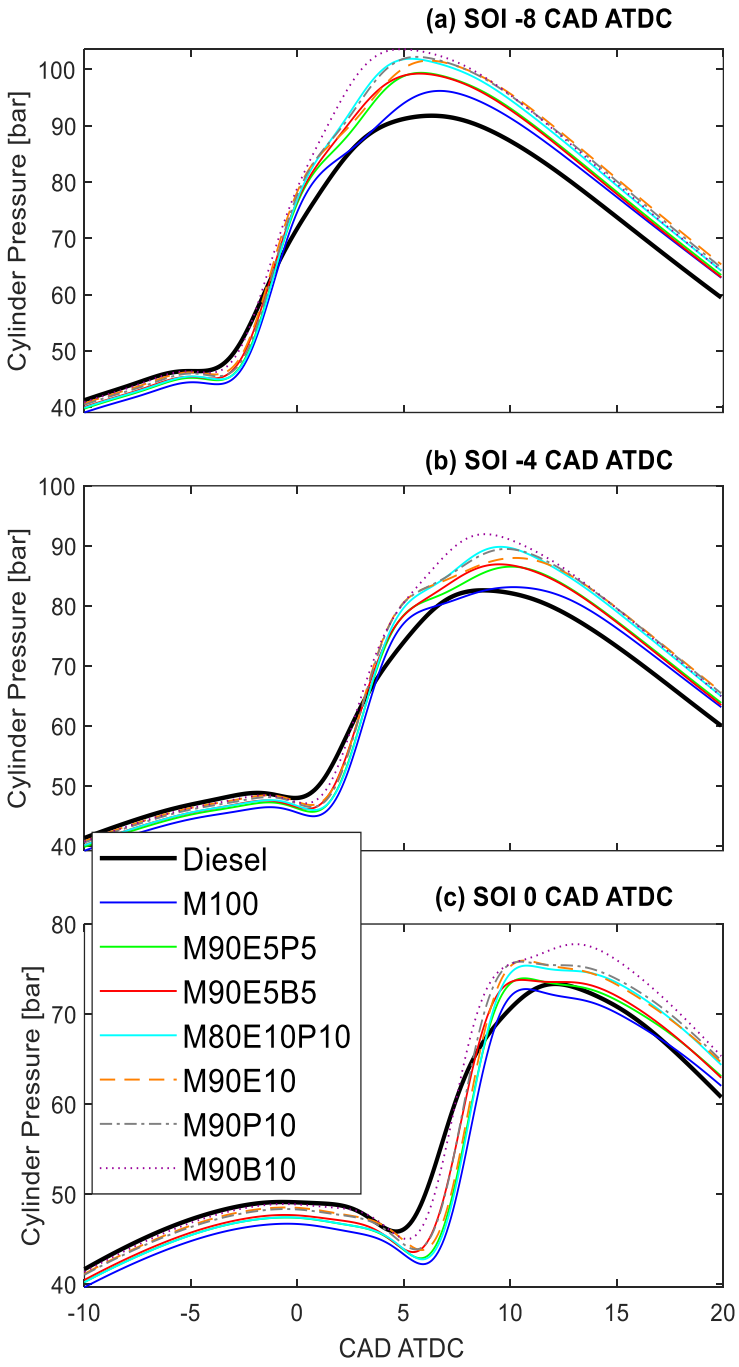

Figure 13- Effect of Gaseous Mixture Composition on Cylinder Pressure (a- SOI_{DIESEL} -8 CAD ATDC), (b- SOI_{DIESEL} -4 CAD ATDC), (c- SOI_{DIESEL} at TDC), (Metal Engine, 40% Substitution Rate, 1000 RPM, $P_{inj,Diesel}$ = 1000 bar).

The apparent heat release rate (AHRR) plotted in Figure 14 provides additional details about the effect of the C_1-C_4 percentage on combustion behavior. Previous work on the topic [122] suggests that the first AHRR peak was associated with the premixed combustion inside the bowl of the diesel fuel plus some of NG entrained inside the vaporized diesel. It started at local equivalence ratios closer to stoichiometry and continued in a leaning out mixture. As in-cylinder pressure and temperature increased, this premixed combustion extended inside the squish region, but at a slower rate, as turbulence decreased and the heat transfer to the wall increases, due to the higher surface-to-volume ratio in the squish region. The result was the second peak heat release rate which was also observed by previous work conducted on a single cylinder CI engine converted to SI operation that maintained the original diesel bowl-in-piston geometry [121]. As the equivalence ratio (shown later in Figure 24 and Figure 25) was very lean (0.52-0.57 global ϕ), it suggests that the combustion process after the first AHRR peak was a combination of flame propagation and autoignition, which was expected considering the high compression ratio (CR = 17) of this engine. Unlike what was shown for in-cylinder pressure, M90B10 generally had the lowest magnitude first AHRR peak, with less ignition delay than other gas blends. M90E5B5 had the second lowest AHRR first peak also with less ignition delay than non-butane blends which further confirms that butane addition impacted the early-stage combustion rate. In general, mixtures with propane had the largest magnitude first AHRR peak suggesting a faster burn rate considering the ignition delay was later or similar to most gas blends over the various SOI_{DIESEL} conditions. Blends with ethane had a higher magnitude first AHRR peak than M100, but not as substantial as propane dominant blends.

The second AHRR peak was more sensitive to change in the C_1-C_4 composition. It was more evident at advanced SOI_{DIESEL} due to the associated increase in bulk temperature (later shown in Figure 34), hence an increase in the kinetics rates. Specifically, it shows substantial differences in the second heat release peak location and magnitude. As expected, the mixtures with butane and propane combusted faster inside the lower-turbulence and higher heat transfer squish region, due to lower autoignition temperatures. For M90B10 with advanced SOI_{DIESEL} the second peak appears more like a lower magnitude continuation of the first peak. At the opposite, M100 had the lowest and most delayed second heat release peak. Therefore, it can be inferred that the autoignition temperature will play an important role in increasing or decreasing the combustion rate at low load operating conditions. Figure 14 also shows the second AHRR peak magnitude was consistently the highest for M90B10, M80E10P10, M90P10, and M90E5B5 in that order, with earlier second

AHRR phasing related to an increase in magnitude of the peaks. The lowest second AHRR peak was consistently associated with M100, however for earlier SOI_{DIESEL} M100 also had the most heat release occur in the late stages of combustion. This suggests that methane trapped in the crevices continued to burn late into the expansion stroke as compared to other gas blends which had a faster initial AHRR. The other gas blends did not follow a specific pattern and were more dependent on SOI_{DIESEL} compared to those previously mentioned, with M90E10 being the most sensitive. Lastly, the differences in second AHRR peak at SOI_{DIESEL} = TDC were minimal, due to the increase in the squish volume at the time combustion reached that region compared to the more advanced SOI_{DIESEL} operation.

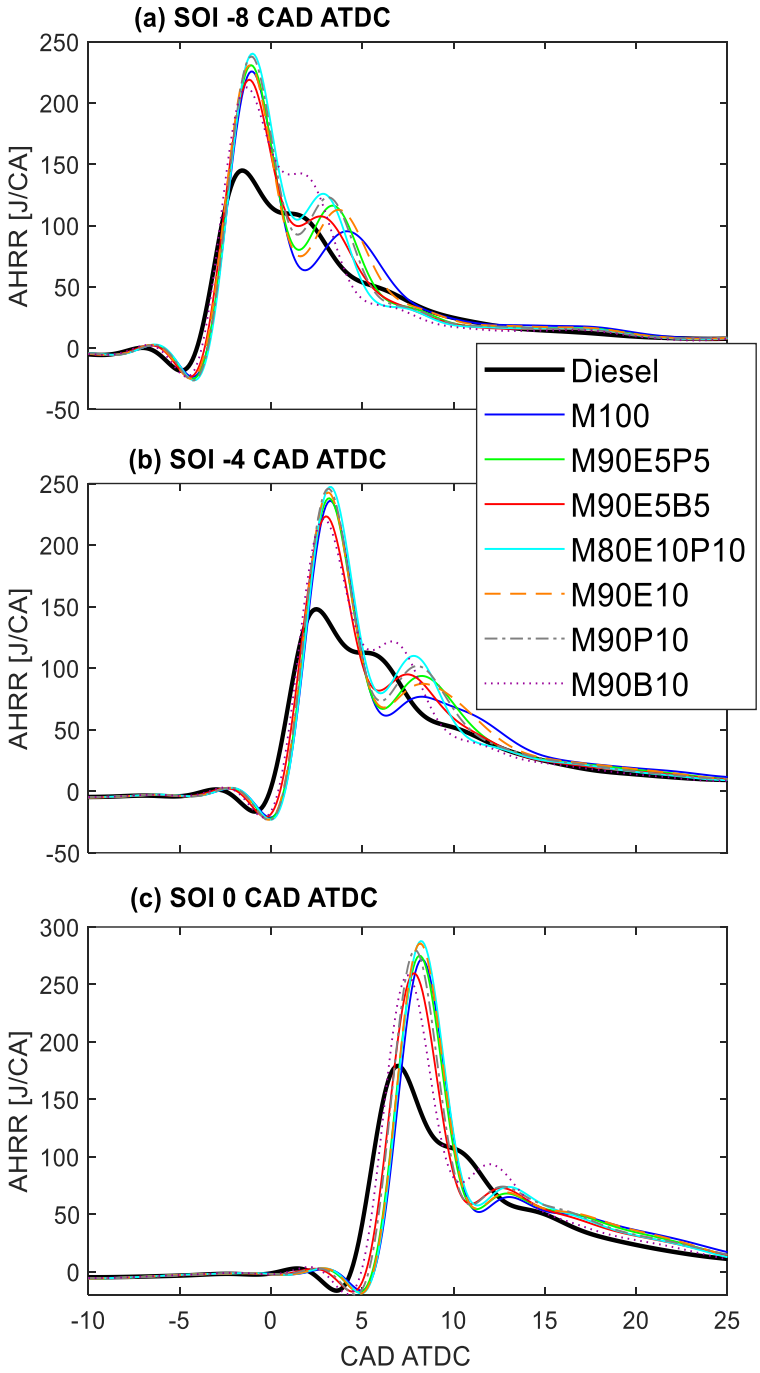

Figure 14- Effect of Gaseous Mixture Composition on Apparent Heat Release Rate (a- SOI_{DIESEL} -8 CAD ATDC), (b- SOI_{DIESEL} -4 CAD ATDC), (c- SOI_{DIESEL} at TDC), (Metal Engine, 40% Substitution Rate, 1000 RPM, $P_{inj,diesel}$ = 1000 bar)

The maximum in-cylinder pressure and location were plotted in Figure 15, including their cycle-to-cycle variation with SOI_{DIESEL} advancing from left to right. The effect of the C_1-C_4 percentage was more apparent in terms or magnitude at earlier SOI_{DIESEL}, but the opposite was true for

location. M100 had a lower maximum in-cylinder pressure than other gas blends but similar maximum pressure location to the other non-butane blends at SOI_{DIESEL}= -4 CA ATDC and TDC. Blends with butane had the most delayed location for SOI_{DIESEL}= TDC, but high butane content advanced the location for earlier SOI_{DIESEL}. The location of maximum pressure was the most repeatable for baseline diesel operation irrespective of the injection timing and least repeatable for M90P10 at SOI_{DIESEL} = TDC. It also suggests that improvement in the engine performance with high propane or butane content correlated with the higher maximum cylinder pressure and earlier location at SOI_{DIESEL} = -8 CA ATDC and -4 CA ATDC. M100 and M90E10 had a tendency to delay the location of maximum cylinder pressure for early SOI_{DIESEL}, suggesting less favorable combustion phasing and a slower burn rate.

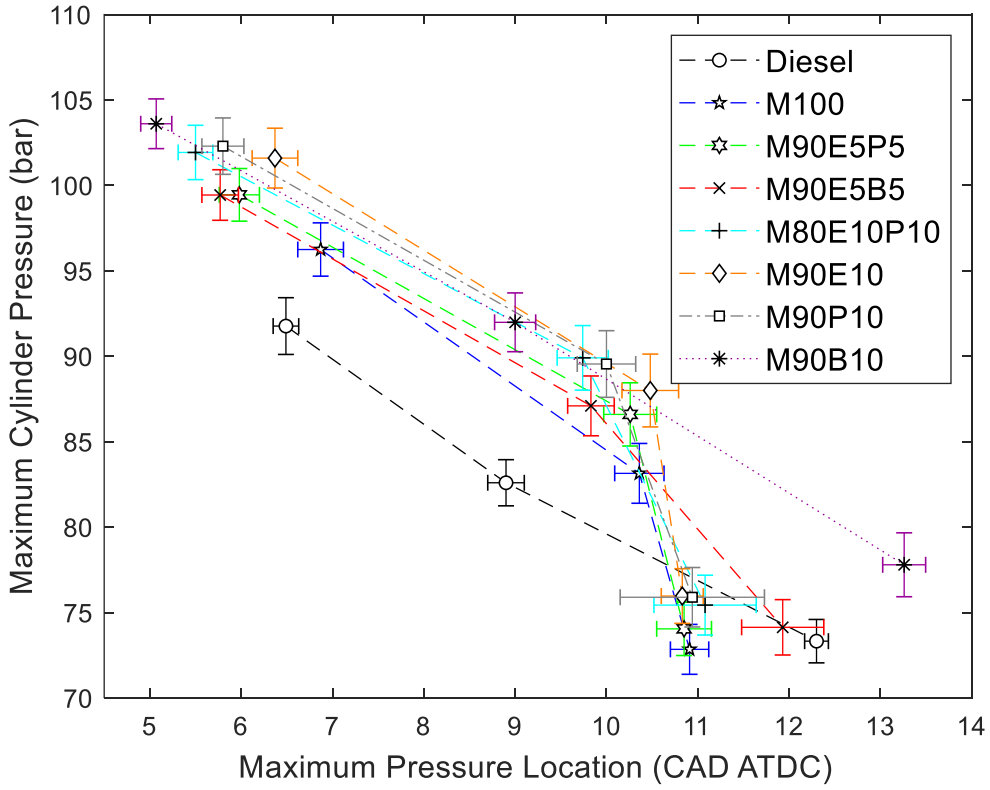

Figure 15- Effect of Gaseous Mixture Composition on Maximum Cylinder Pressure and Location (Metal Engine, 40% Substitution Rate, 1000 RPM, $P_{inj,diesel}$ = 1000 bar). Error Bars Represent the Standard Deviation of the Measurement.

Figure 16 shows the differences in CA50 (defined as the crank angle associated with 50% cumulative heat release) for the different gas blends. Dual-fuel operation delayed CA50 at SOI_{DIESEL} of -4 CA ATDC and 0 CA ATDC (TDC) for most gas blends. M100 produced the largest

CA50 delay (~ 2 CAD), while the CA50 for M90E10, M90E5P5 and M90P10 were relatively similar. As CA50 in a diesel engine converted to SI NG operation was near the end of the fast burn inside the piston bowl [122] , it correlates with the small differences between M90E10, M90E5P5 and M90P10 first AHRR peak in Figure 14. The most advanced combustion phasing occurred for M90B10 followed by M80E10P10, M90P10 and M90E5B5 (nearly identical), M90E5P5, M90E10, and M100. The only exception to this order was for M90E5P5 and M90E10 being switched for SOI_{DIESEL}= TDC. The diesel baseline was the most sensitive to SOI, varying from a second most delayed at SOI -8, third most advanced at SOI -4, and most advanced at TDC. Based on the locations of CA50 a strong dependency on the start of the second AHRR peak and magnitude was observed. For this reason, M90B10 and M100 were the most and least advanced, respectively. The deviation in CA50 location for different gas blends was similar at each SOI_{DIESEL} condition, with less deviation at earlier injection timings. It is interesting to observe that CA50 for all blends with C_2-C_4 addition advanced slightly at SOI_{DIESEL}= -8 CA ATDC and that M80E10P10 advanced also at SOI_{DIESEL}= -4 CA ATDC over the diesel baseline. This fact seems to support the notion that auto-ignition temperature of the fuel components played an important role in the rate of early fuel oxidation.

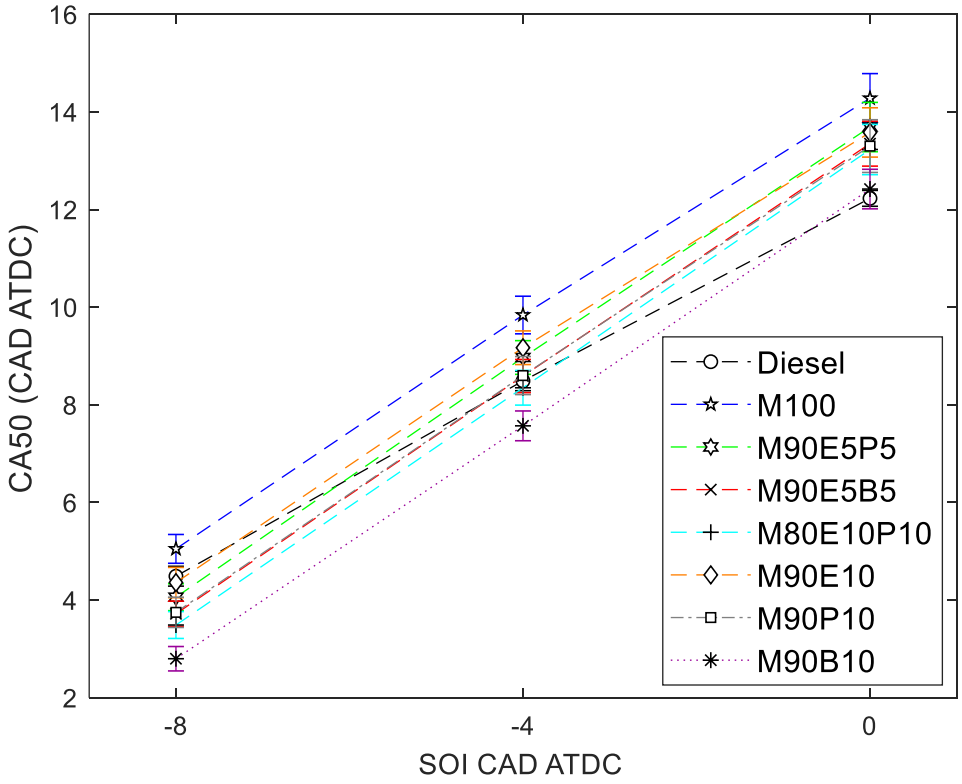

Figure 16- Effect of Gaseous Mixture Composition on CA50 (Metal Engine, 40% Substitution Rate, 1000 RPM, $P_{inj,diesel}$ = 1000 bar). Error Bars Represent Standard Deviation of the Measurement

The ignition delay (defined as the duration in CAD between SOI_{DIESEL} command and the crank angle associated with 10% cumulative heat release) is shown in Figure 17. It suggests that the advanced CA50 was due to the ignition delay becoming shorter as SOI_{DIESEL} advanced. Specifically, there was ~1 CAD increase in the ignition delay for M100 at SOI_{DIESEL} = TDC compared to a similar ignition delay to baseline diesel at SOI_{DIESEL} = -8 CA ATDC. The shortest ignition delay of the dual-fuel cases consistently occurred for blends with butane addition, again related to lowest auto-ignition temperature. The fact that M80E10P10 and M90E5P5 had a longer ignition delay than M90E10 was therefore unexpected. For late SOI_{DIESEL} the addition of propane to blends with ethane contributed to a longer ignition delay even if the volume fraction was the same for propane (M80E10P10 and M90E5P5 compared to M90P10). There could be a less favorable reaction chain branching responsible for this observation, but further investigation would be required. The ignition delay data suggests that a relatively small change in SOI_{DIESEL} can have an important effect in the ignition delay of the dual-fuel operation based on NG blend composition,

which is important for engine control applications. Specifically, engine manufacturers can update the original diesel operating map to allow for dual-fuel operation of a particular NG composition.

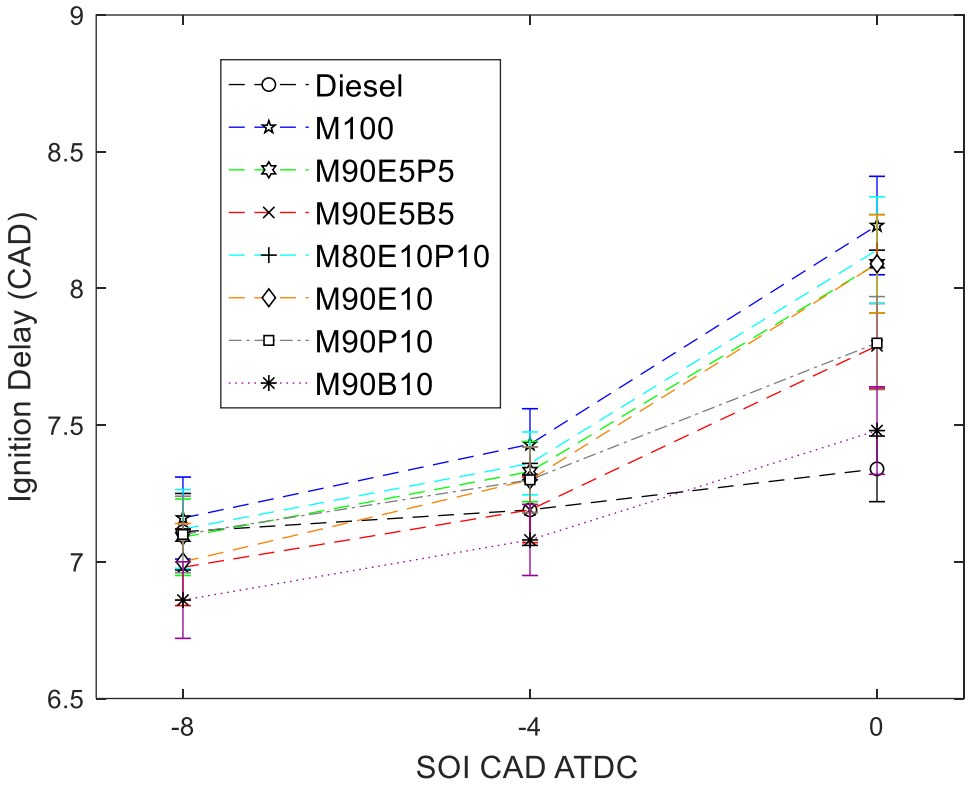

Figure 17- Effect of Gaseous Mixture Composition on Ignition Delay (Metal Engine, 40% Substitution Rate, 1000 RPM, $P_{inj,diesel}$ = 1000 bar). Error Bars Represent Standard Deviation of the Measurement

The combustion duration (defined as the duration in CAD between the 10% and 90% cumulative heat release) shown in Figure 18 suggests a similar decreasing trend with delayed SOI_{DIESEL} for all fuels. Dual-fuel operation with M100 increased the combustion duration by ~2-3 CAD compared to the diesel baseline, irrespective of the SOI_{DIESEL}. Combustion duration for C_2-C_4 gas blends increased over the baseline diesel at all SOI_{DIESEL}, however it was roughly half the increase experienced by M100. The increased combustion duration of M100 is also evident in the AHRR in Figure 14 which has a longer late-stage heat release than other blends, likely due to more fuel trapped in crevices re-entering the combustion chamber later in the expansion stroke. This is important because, at similar ignition delays as those in this work, a longer combustion duration can affect efficiency and emissions, as discussed later. The most substantial deviation in combustion duration occurred for M90B10 at all SOI_{DIESEL} conditions. The only common trend

for C_2-C_4 blends was that M80E10P10 consistently had the shortest combustion duration for all SOI_{DIESEL} conditions, with the other blends being more sensitive to injection timing.

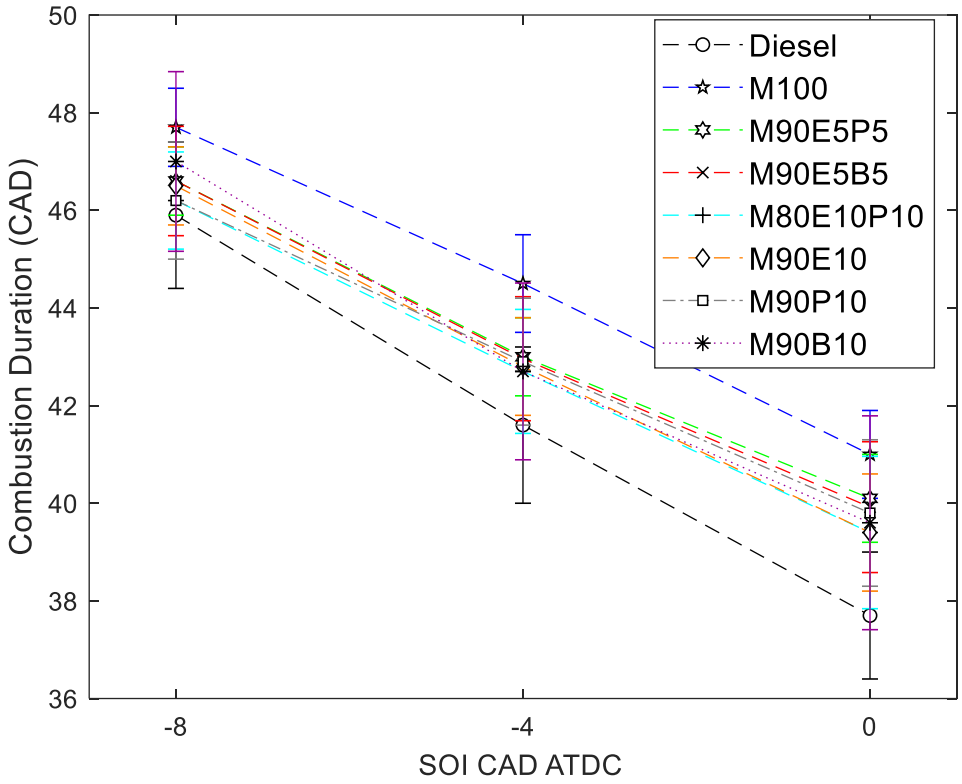

Figure 18- Effect of Gaseous Mixture Composition on Combustion Duration (Metal Engine, 40% Substitution Rate, 1000 RPM, $P_{inj,diesel}$ = 1000 bar). Error Bars Represent Standard Deviation of the Measurement

With tests being conducted at the same speed, Figure 19 suggests that diesel maximum brake torque (MBT) timing occurs at -4 CAD ATDC. Most of the dual-fuel cases follow the same trend, however the change in BMEP and thus power between SOI_{DIESEL}= -8 to 0 CAD ATDC was not as pronounced. The differences in combustion phasing shown previously affected the performance data. It shows the 40% diesel replacement at these lower load dual-fuel operating conditions reduced BMEP by ~ 7% compared to the diesel baseline. Both the diesel baseline and dual-fuel operating conditions shared the same MBT timing, however the magnitude of change was smaller for dual-fuel operation. The highest BMEP of the dual-fuel cases was for blend M90P10 at all SOI_{DIESEL} conditions, but also for M90B10 at SOI_{DIESEL} = -4 CA ATDC. As previously shown by CA50, this does not correspond to an earlier combustion phasing for M90P10. Interestingly, M90E5B5 and M90E5P5 had perfectly overlaying BMEP for all SOI_{DIESEL}, only with variations

in the deviation at the conditions. In general, due to the constant fuel energy input the BMEP differences of the tested blends had overlapping standard deviation which suggests a high degree of similarity in power output.

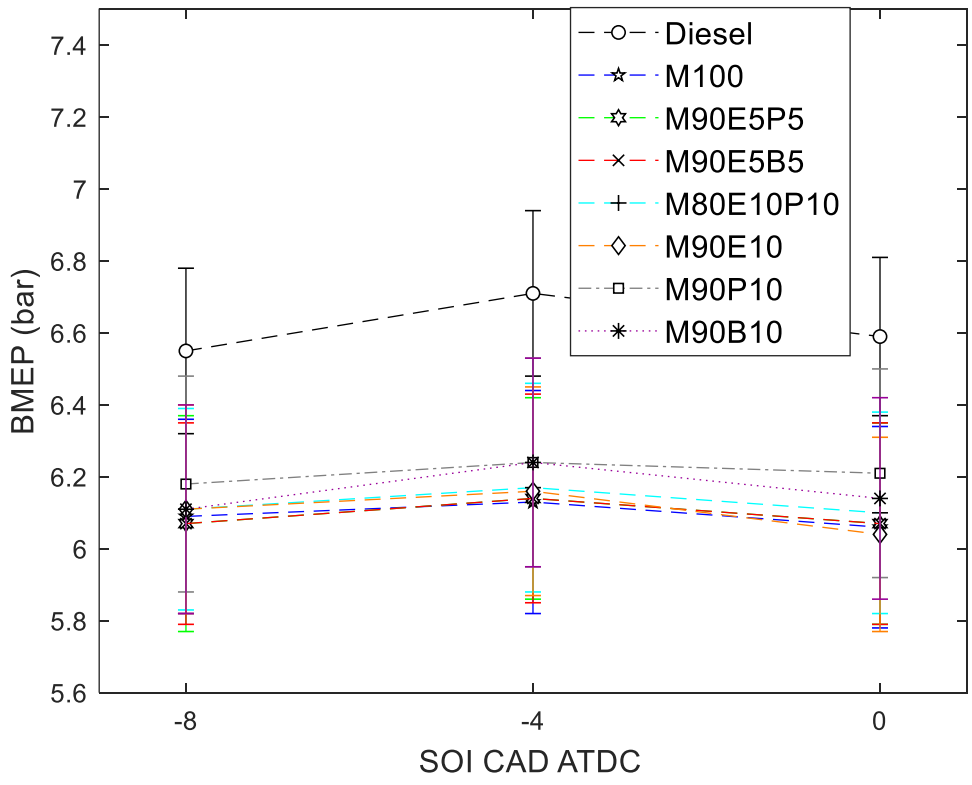

Figure 19- Effect of Gaseous Mixture Composition on Brake Mean Effective Pressure (Metal Engine, 40% Substitution Rate, 1000 RPM, $P_{inj,diesel}$ = 1000 bar). Error Bars Represent Standard Deviation of the Measurement

An unexpected finding by closer examination of the BMEP to IMEP ratio shown in Figure 20 details large discrepancies between dual-fuel operation and the diesel baseline. The IMEP and BMEP was within 12% difference for all diesel baseline conditions, however for dual-fuel operation there was a 37-42% difference. Furthermore, this difference was not directly correlated with higher or lower fuel density. The most apparent reason for the difference between diesel only and dual-fuel operation would relate to added pumping losses or a change in the mixture polytropic index of expansion. It would be expected that higher NG LHV would have a lowering effect on the ratio due to a smaller NG mass required to meet the constant energy input requirements, however M100 had an average BMEP to IMEP ratio compared to the other fuel blends. Another explanation could be increased heat transfer to the walls for certain gas blends compared to

primarily air in the outer fuel jet regions of the diesel only case. Only one other reference has mentioned this discrepancy [61], but not for dual-fuel conditions other than propane-diesel combustion. This finding also is important because most research works on dual-fuel operation only consider the IMEP values for data analysis, which would not reflect a realistic power output expected by the end user of the engine platform. Further investigation into this phenomenon should be considered in future research.

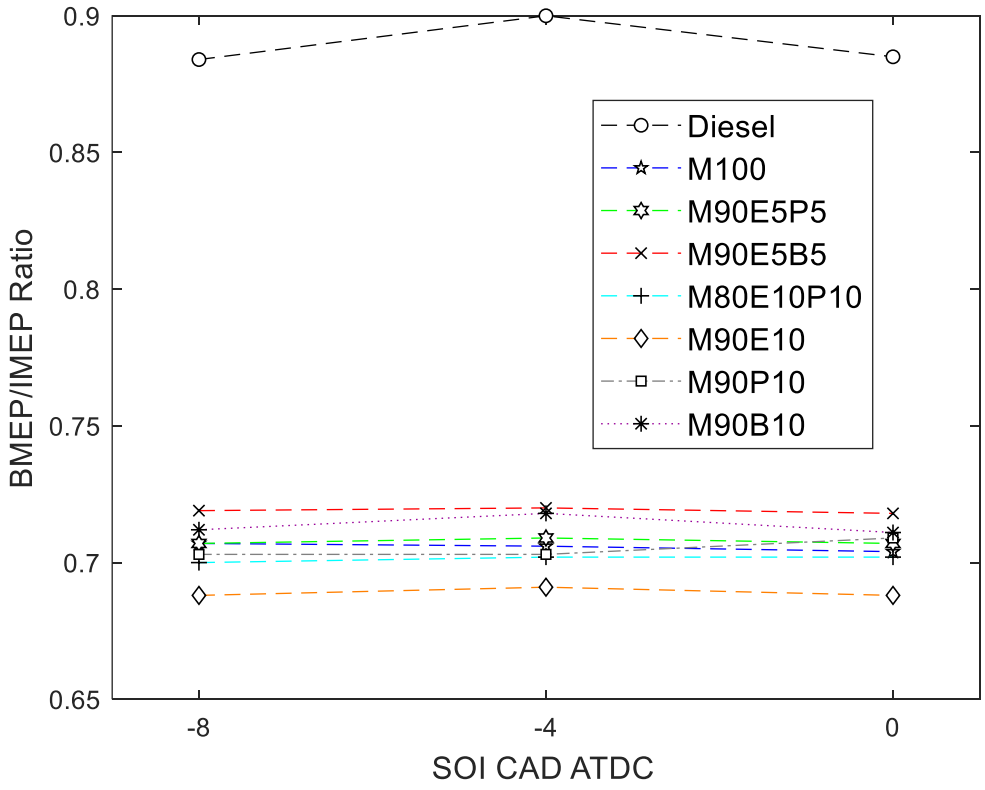

Figure 20- Effect of Gaseous Mixture Composition on BMEP to IMEP (Metal Engine, 40% Substitution Rate, 1000 RPM, $P_{inj,diesel}$ = 1000 bar)

The COV of IMEP in Figure 21 shows that dual-fuel conditions all remained below 3% which indicates stable combustion. The COV of IMEP for the diesel baseline was between 3.5-3.7% which is also stable for practical purposes [11]. M100 had the lowest COV of IMEP for all SOI_{DIESEL} conditions tested followed by M90E5P5 and M90P10. M100 was also the only dual-fuel case to increase the COV of IMEP steadily with delayed SOI_{DIESEL}. M90E5B5 showed the most sensitivity to SOI_{DIESEL} with higher COV of IMEP at the earliest and latest injection timings compared to the MBT timing of -4 CAD ATDC, matching the same trend exhibited by the diesel

baseline. Blends with ethane had a clear peak in COV of IMEP at the MBT condition which was unexpected. This also correlated to a higher degree of deviation in the CA50 values presented previously in Figure 16. The highest COV of IMEP was found for M80E10P10 at SOI_{DIESEL} =-8 CAD ATDC and for M90B10 at the more delayed conditions. Other studies have found lower COV of IMEP for 40% ESR with methane as compared to the diesel baseline as well, mentioning the lowest combustion variations occurred between 40% to 80% ESR [123].

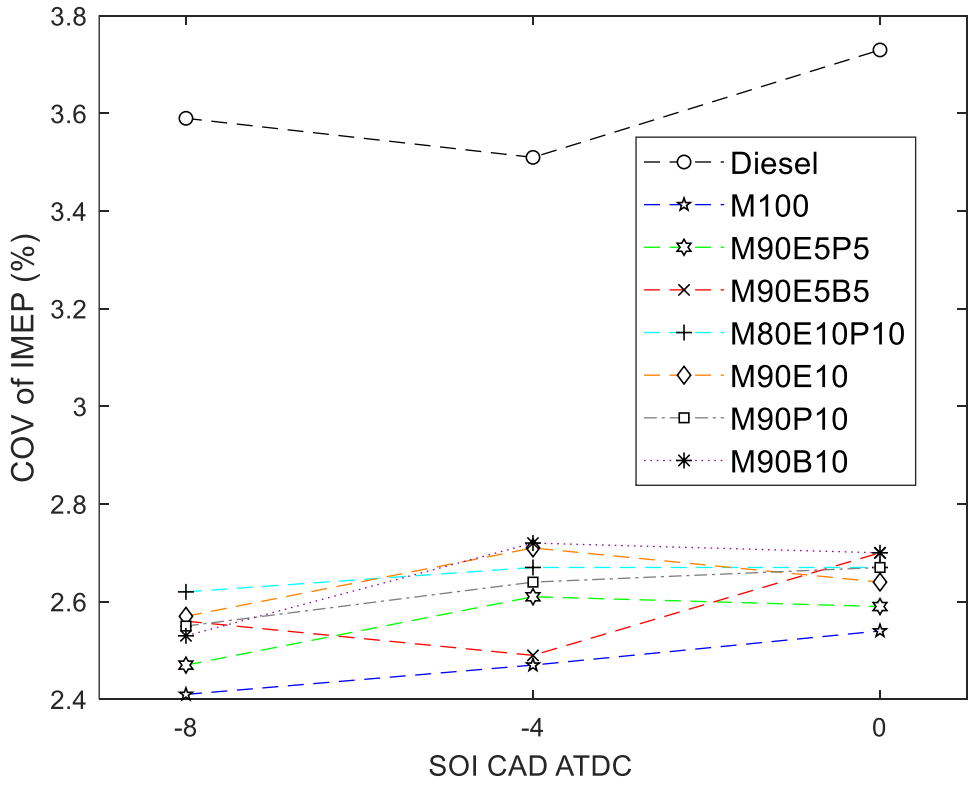

Figure 21- Effect of Gaseous Mixture Composition on COV of IMEP [%] (Metal Engine, 40% Substitution Rate, 1000 RPM, $P_{inj,diesel}$ = 1000 bar)

The BSFC in Figure 22 was lowest for the diesel baseline as expected. The best BSFC of the dual-fuel cases occurred for M90P10, which can be attributed to the slightly higher BMEP previously mentioned. The highest BSFC was found for M90E5B5 followed by M90E10, which again suggests ethane addition negatively affected the power output. The blends with propane generally had the lowest BSFC, while M100 and M90B10 fell into the middle of the dual-fuel cases with a modest increase in BSFC over the diesel baseline. There was not a clear dependency on NG mixture density for lower BSFC considering the densest fuels (M80E10P10 and M90B10) had

higher BSFC than M100 at certain SOI_{DIESEL} conditions. The MBT timing however did reduce BSFC slightly for most dual-fuel cases as expected.

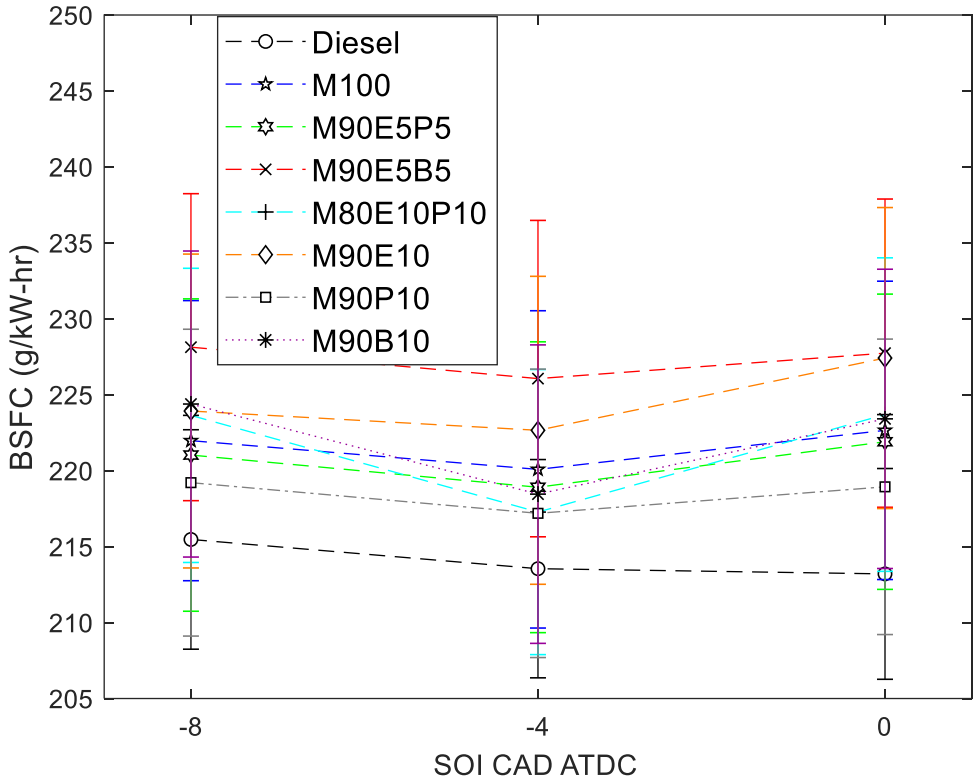

Figure 22- Effect of Gaseous Mixture Composition on Brake Specific Fuel Consumption (Metal Engine, 40% Substitution Rate, 1000 RPM, $P_{inj,diesel}$ = 1000 bar). Error Bars Represent Standard Deviation of the Measurement

The transition from diesel only to dual-fuel combustion translated in ~ 3% lower brake efficiency. However, the literature mentions that dual-fuel operation usually decreases engine performance, and the decrease in BMEP and thermal efficiency is similar to what was reported. The diesel thermal efficiency was also within an expected range based on the low load conditions [11]. While the BMEP and brake thermal efficiency differences between the C_1-C_4 gas blends were relatively small, M90P10 consistently performed better. Figure 23 shows the lowest thermal efficiency was for M90E5B5, M90E10, and M100 in that order and ethane addition produced the highest losses. Specifically, blend LHV and density played an important role in differentiating thermal efficiency, while fuels M100 and M90E5B5 had similar BMEP values. It should be noted that at the MBT timing the denser fuels produced a slightly higher thermal efficiency, albeit for blends with ethane. This could be due to a lower fraction of the premixed fuel entering into crevices near the location

of peak combustion efficiency nearest TDC, or from differences in equivalence ratio as discussed next.

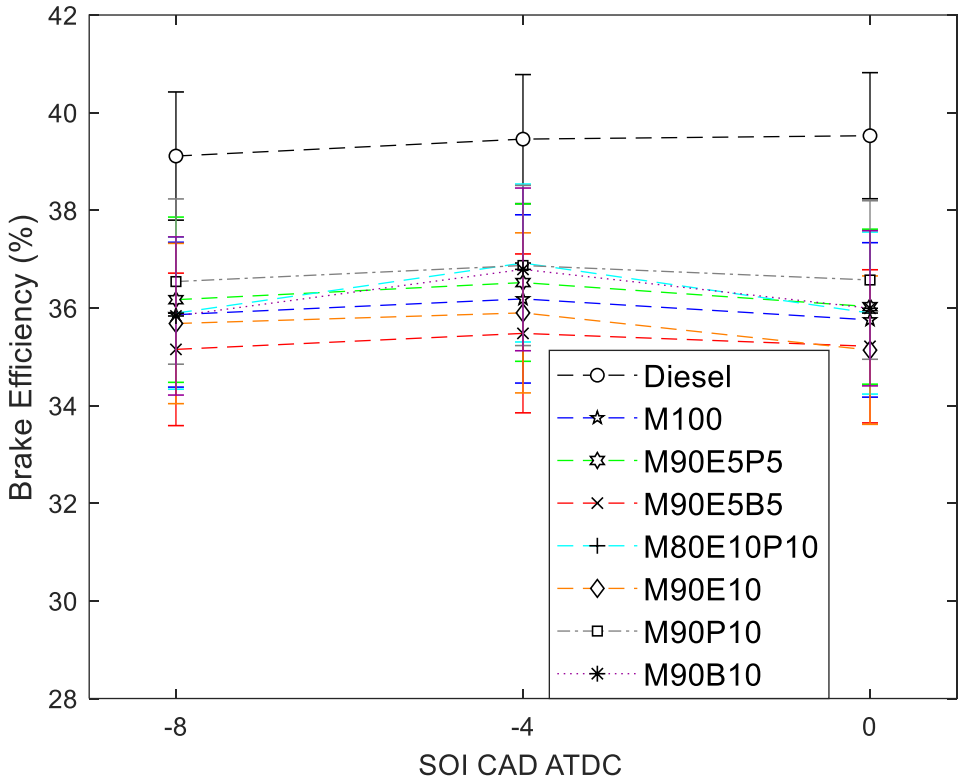

Figure 23- Effect of Gaseous Mixture Composition on Brake Efficiency (Metal Engine, 40% Substitution Rate, 1000 RPM, $P_{inj,diesel}$ = 1000 bar). Error Bars Represent Standard Deviation of the Measurement

The variation in global equivalence ratio (ϕ) shown in Figure 24 provides more detail on in-cylinder condition differences. The global ϕ was between 0.52 and 0.57 for both the diesel baseline and dual-fuel conditions. The highest global ϕ was for M90E5B5 followed by the diesel baseline, M80E10P10, M100, M90P10, M90E10, M90B10, and M90E5P5, except for M80E10P10 at the MBT timing. The variations were a result of constant energy input requirements, but also due to measurement error and the difficulty in controlling the fuel flow for multiple gas components simultaneously. For example, maintaining the desired energy input constant became more difficult to control for gas blends with higher carbon content due to changes in delivery temperature and pressure. Specifically, pure butane delivered at laboratory ambient conditions was difficult to maintain at a constant delivery pressure because the output flow was dependent on the boil-off rate

inside the gas cylinder and thus more fluctuation in the butane mass flow rate occurred. However, the differences in global ϕ also result from different LHV, AFR_{stoich}, and in-cylinder AFR, thus are difficult to directly compare the effects. Yet the global ϕ can be used to help explain why M90E5B5 had a lower thermal efficiency with inherently higher fuel fractions trapped into crevices. The global ϕ was also subject to measurement error in the diesel fuel scale mass, with the interpretation method described in Appendix A Figure 72.

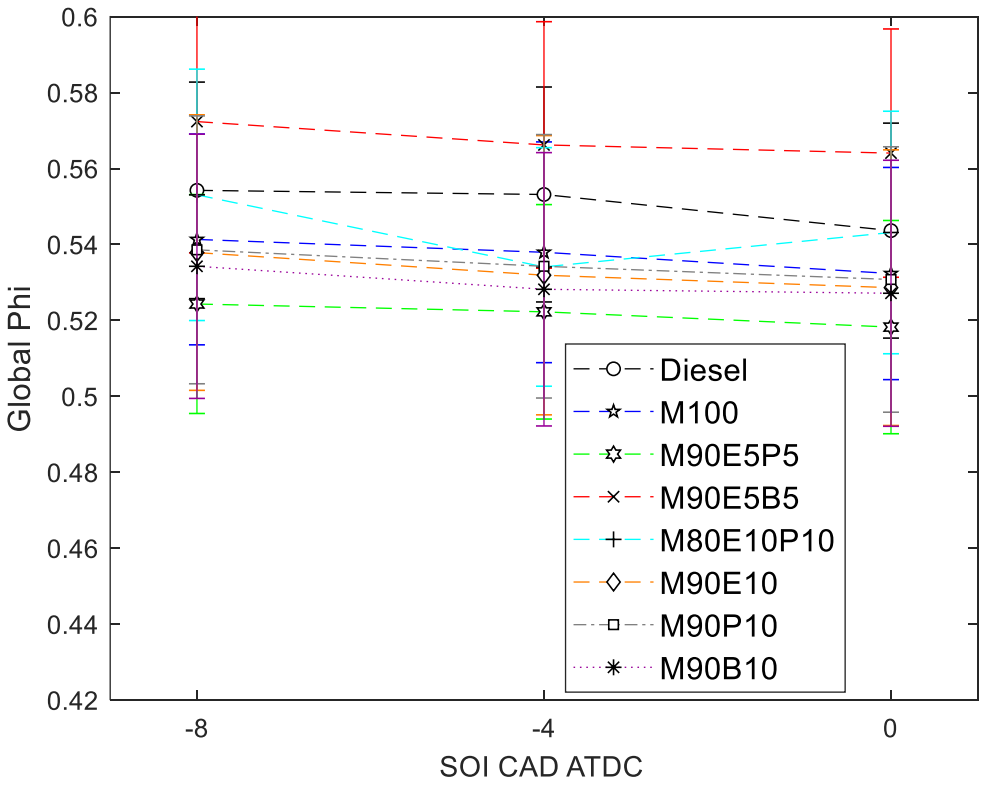

Figure 24- Effect of Gaseous Mixture Composition on Global Phi (φ) (Metal Engine, 40% Substitution Rate, 1000 RPM, $P_{inj,diesel}$ = 1000 bar). Error Bars Represent Standard Deviation of the Measurement

The premixed ϕ in Figure 25 shows a similar trend to global ϕ for most dual-fuel conditions. However, a clear distinction can be made for M90E10 having a lower premixed ϕ than global ϕ. All premixed equivalence ratios remained between 0.21 and 0.23. This shows that the larger deviations in global ϕ were indeed subject to multiple device uncertainties combined, as well as the unknown repeatability of the diesel injection quantity at the given injection duration command. Considering that M90P10 and M90B10 had the best performance metrics, it can be concluded that

the premixed ϕ was not a dominating factor compared to how the change in the auto-ignition temperature of the gaseous mixture affected combustion phasing.

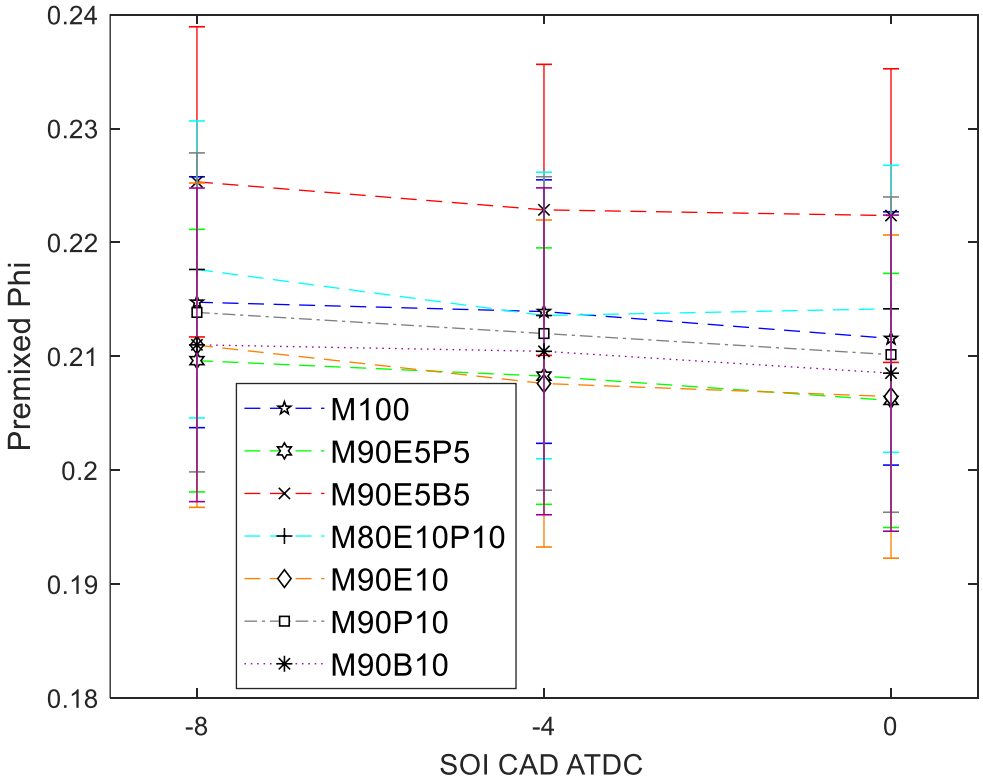

Figure 25- Effect of Gaseous Mixture Composition on Premixed Phi (φ) (Metal Engine, 40% Substitution Rate, 1000 RPM, $P_{inj,diesel}$ = 1000 bar). Error Bars Represent Standard Deviation of the Measurement

Figure 26 shows that, compared to the diesel baseline, dual-fuel operation decreased brake specific CO_2 ($BSCO_2$) emissions for all operating conditions, as also mentioned in the literature. This reduction was a direct impact of the lower C:H ratio of the C_1-C_4 components while the diesel produced more brake power (hence higher BMEP), as shown in Figure 19. M90P10 at SOI_{DIESEL}=-4 CAD ATDC had the largest $BSCO_2$ reduction (6.6%) compared to the diesel baseline, while the least reduction (2.6%) occurred for M90E5B5 at the most advanced injection timing. Considering the experiments were conducted at a constant fuel energy among the C_1-C_4 blends, the energy to theoretical CO_2 ratio in

Table 7 suggests that M100 should have had the lowest $BSCO_2$ while M90B10 and M80E10P10

Mixture Name	LHV [kJ/kg]	AFR Mass	Density [kg/m^3]	WI [kJ/kg]	MN	Propane Knock Index	Knock Rating	CO_2 ratio [kg CO_2/kg fuel]	S_L [cm/s]
M100	50000	17.12	0.67	74600	100	0	good	2.74	38.22
M90E5P5	49400	16.83	0.76	68800	72	6.1	bad	2.79	39.87
M90E5B5	49200	16.75	0.79	67100	57	16	bad	2.80	NA
M80E10P10	48900	16.61	0.85	64200	63	12	bad	2.83	41.15
M90E10	49600	16.92	0.73	70700	81	2.9	good	2.78	38.82
M90P10	49100	16.75	0.79	67100	66	10	bad	2.80	41.05
M90B10	48800	16.61	0.85	64100	<46.8	30	bad	2.83	NA

should have had the highest $BSCO_2$. Theory suggests that, compared to M100, a 5.5% maximum increase between the blends should be expected, yet the difference between M90E5B5 and M100 was 3.4% at most. It was unexpected that those blends had one of the lowest $BSCO_2$ values for SOI_{DIESEL}=-4 CAD ATDC, almost the same as for M100. This was due to the slightly increased BMEP at the given condition, meaning that the enhanced combustion characteristics played a more important role in determining $BSCO_2$. Also, for the same reason M90P10 had the lowest $BSCO_2$ at all test conditions.

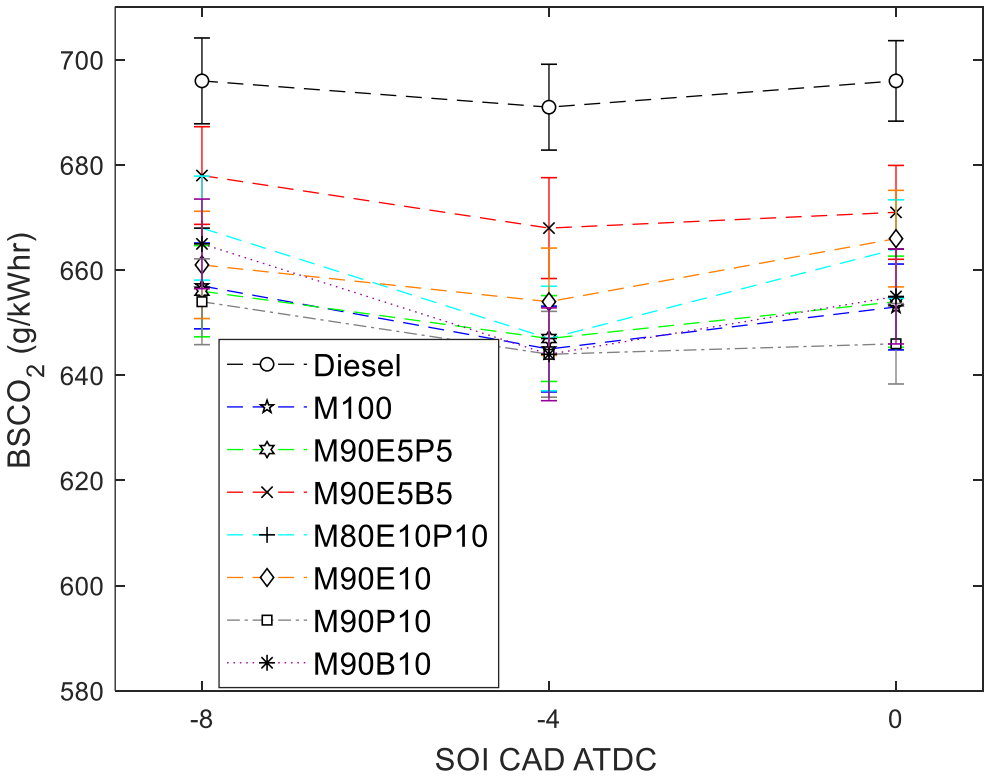

Figure 26- Effect of Gaseous Mixture Composition on Brake Specific CO_2 (Metal Engine, 40% Substitution Rate, 1000 RPM, $P_{inj,diesel}$ = 1000 bar). Error Bars Represent Standard Deviation of the Measurement

The brake specific CO (BSCO) emissions are shown in Figure 27. As expected, dual-fuel operation substantially increased BSCO over the diesel baseline due to a higher degree of in-complete combustion (up to 3000% for M90B10 at TDC). The primary reason for the lower combustion efficiency is the fuel trapped inside crevices during compression and partially oxidizing later in the expansion stroke when it re-enters the combustion chamber. Reduced combustion efficiency was also due to a higher fraction of the premixed air-fuel mixture pyrolyzing near the walls due to the local temperature being much lower than the temperature in the vicinity of the burning diesel jets. M100 had the lowest BSCO except for SOI_{DIESEL}=-4 CAD ATDC, where M80E10P10 had a slightly lower (by ~0.1 g/kWh) BSCO. M90B10 had a substantial BSCO increase over the grouping of other blends, while M90E5B5 was in the middle of the grouping. Blends with both ethane and propane remained on the lower end of BSCO emissions, suggesting some benefit of the two components interacting. This complimentary benefit was supported by M90E10 and M90P10 having the second and third highest BSCO respectively.

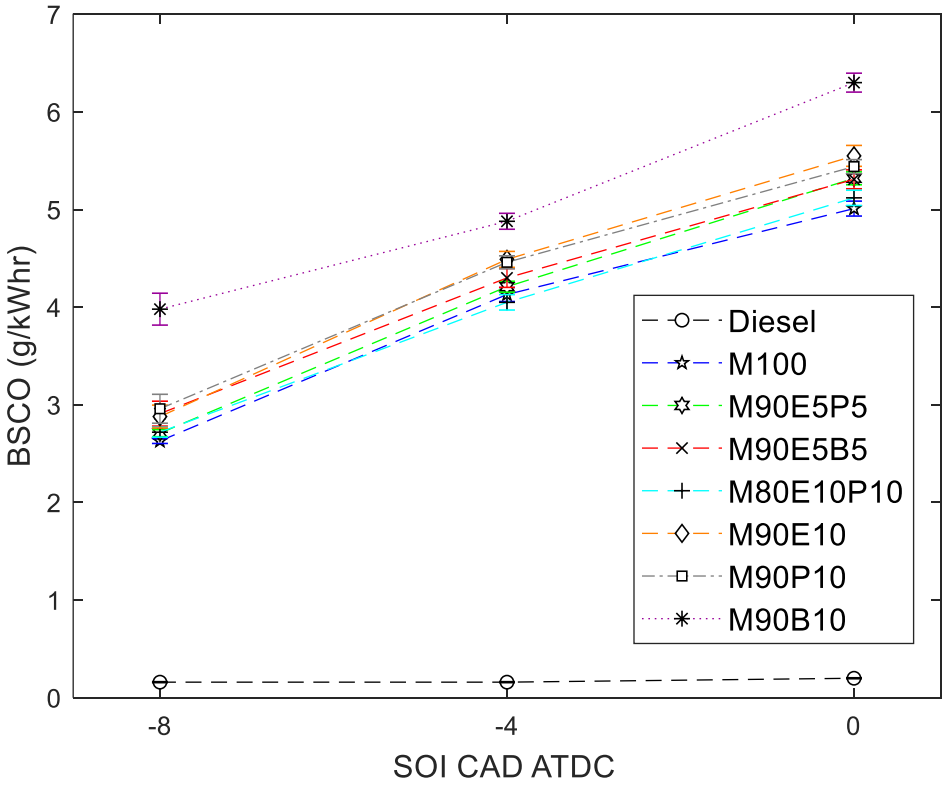

Figure 27- Effect of Gaseous Mixture Composition on Brake Specific CO (Metal Engine, 40% Substitution Rate, 1000 RPM, $P_{inj,diesel}$ = 1000 bar). Error Bars Represent Standard Deviation of the Measurement

Figure 28 shows the brake specific oxides of nitrogen ($BSNO_x$). As expected, the dual-fuel combustion decreased $BSNO_x$ up to 21% compared to the diesel baseline. Of the gas blends, M90E5B5 had the highest $BSNO_x$ followed by M90B10, while M100, M90P10, and M90E10 had the lowest. Indications of thermal NO importance for these operating conditions can be inferred from the fact that M90E5B5 had the highest maximum cylinder temperature and M90E10 had the lowest, which also corresponded to highest and lowest $BSNO_x$. However, when considering the other gas blends, the difference was associated to both the increased bulk gas temperature and change in BMEP. The maximum in-cylinder temperature (later shown in Figure 34) also does not explain why $BSNO_x$ decreases with advanced SOI_{DIESEL} for the diesel baseline while maximum in-cylinder temperature increases with delayed SOI. This was assumed to be a result of NO_X forming at a higher rate in the vicinity of the high temperature combusting diesel spray, which increased as the SOI_{DIESEL} was delayed. Lastly, unlike BSCO emissions, the combination of ethane and propane increased $BSNO_x$ emissions.

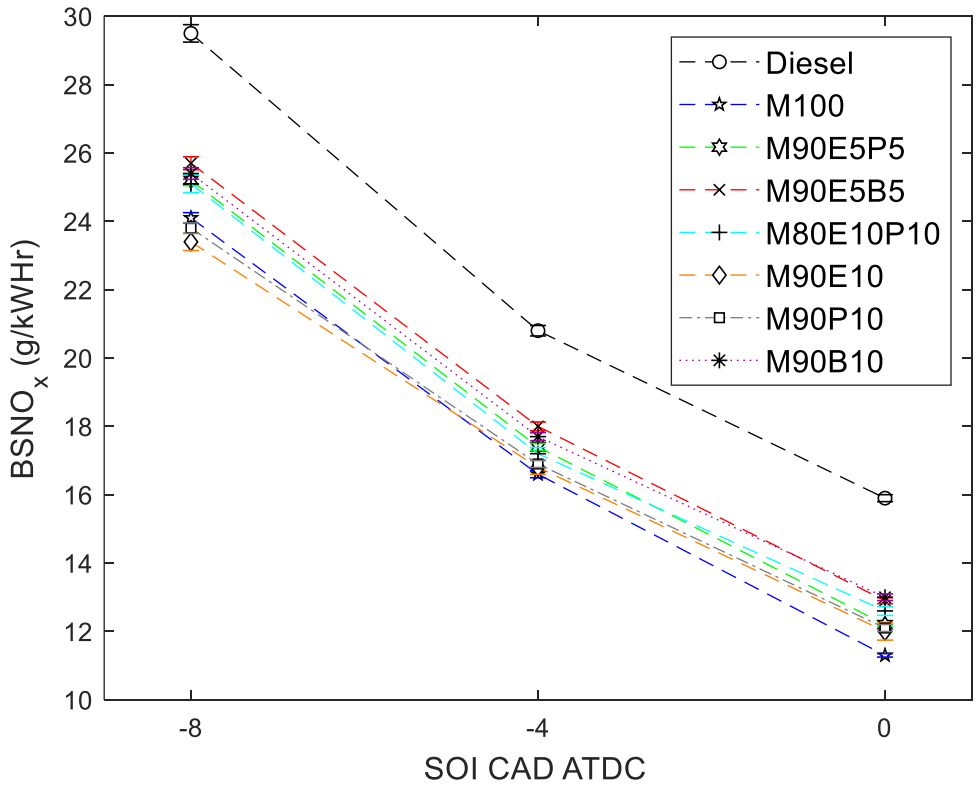

Figure 28- Effect of Gaseous Mixture Composition on Brake Specific NO_X (Metal Engine, 40% Substitution Rate, 1000 RPM, $P_{inj,diesel}$ = 1000 bar). Error Bars Represent Standard Deviation of the Measurement

Figure 29 shows the brake specific hydrocarbon (BSHC) emissions. The HC emissions represent the sum of C_1-C_4 hydrocarbon emissions as well as diesel and any other HC resulting from the partial fuel oxidation and species recombination. M100 and M90E10 had the highest BSHC emissions, both within the same deviation. This was followed by M90E5P5 and M90E5B5, which had nearly identical results. The lowest BSHC emissions were for blends with 10% propane or 10% butane. In particular, M80E10P10 had the lowest BSHC of all mixtures, mainly due to the lower methane content. This was due to a combination of better fuel oxidation (lower CO emissions than other blends besides M100), but also due to the FTIR sensitivity to methane emissions. The FTIR has a sample range of 3000 ppm for methane as compared to 500 ppm ethane and 200 ppm propane. The sampled ethane emissions for M90E10 were approximately 80 ppm while the HC emissions were close to 400 ppm. This large difference in HC emissions was assumed to be from the unburnt diesel or partially pyrolyzed ethane and methane. M100 BSHC emissions were roughly 300 ppm over the measured CH_4 emission values. Therefore, the

additional 300 ppm over the pure species measurements in C_1-C_4 blend data was assumed as diesel interference and partially oxidized components for all tests. The BSHC emissions had a tight repeatability band (~0.1 g/kWh) for all fuels tested, especially at earlier SOI_{DIESEL}.

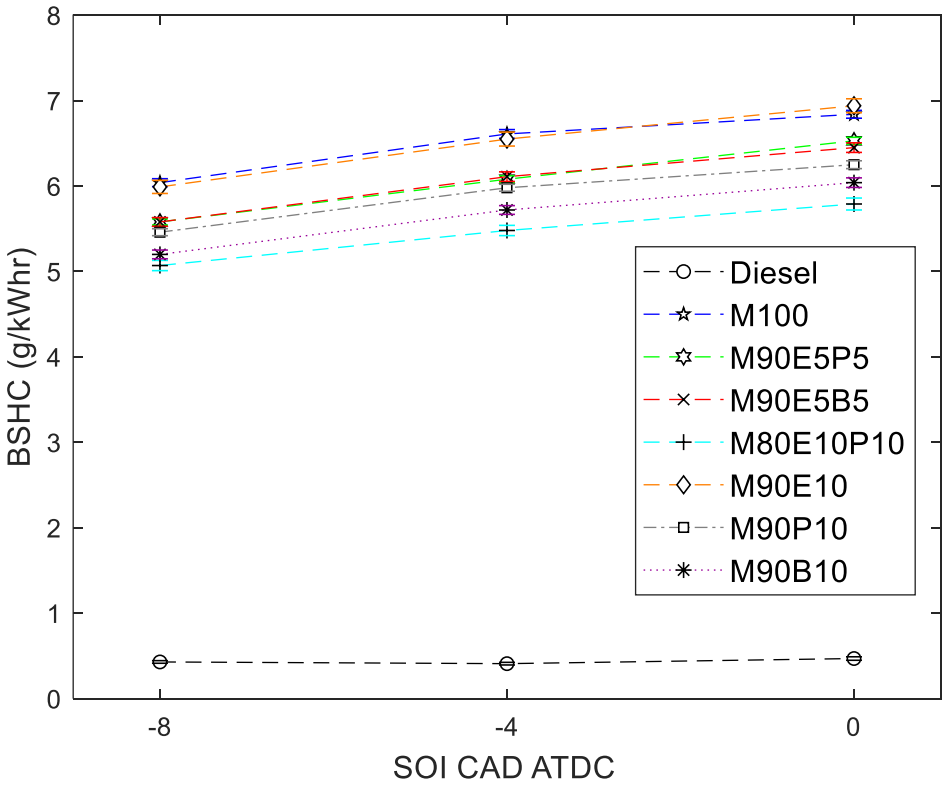

Figure 29- Effect of Gaseous Mixture Composition on Brake Specific HC (Metal Engine, 40% Substitution Rate, 1000 RPM, $P_{inj,diesel}$ = 1000 bar). Error Bars Represent Standard Deviation of the Measurement

Figure 30 shows the combination of BSHC and BSCO emissions, a metric used to compare fuel oxidation quality between different gas blends. Due to BSHC emissions having a higher proportion in the addition, M80E10P10 again was the lowest. The low BSCO emissions coupled with low BSHC indicated that M80E10P10 had the best fuel conversion efficiency between all gas blends. Further, it was observed that all fuel blends with propane had a similar benefit of lower BSCO+BSHC, with M90E5P5 and M90P10 being the second and third lowest. M90E10 and M90B10 had the highest BSCO+BSHC, depending on SOI_{DIESEL}. For M90E10 this was primarily due to the high BSHC emissions, while for M90B10 this was due to high BSCO emissions. M100 had a slightly higher than average BSCO+BSHC, which indicates that ethane and propane addition

had clear benefits for fuel oxidation. On the other hand, butane addition tended to have less of an impact on BSCO+BSHC, even though it provided benefits to BMEP.

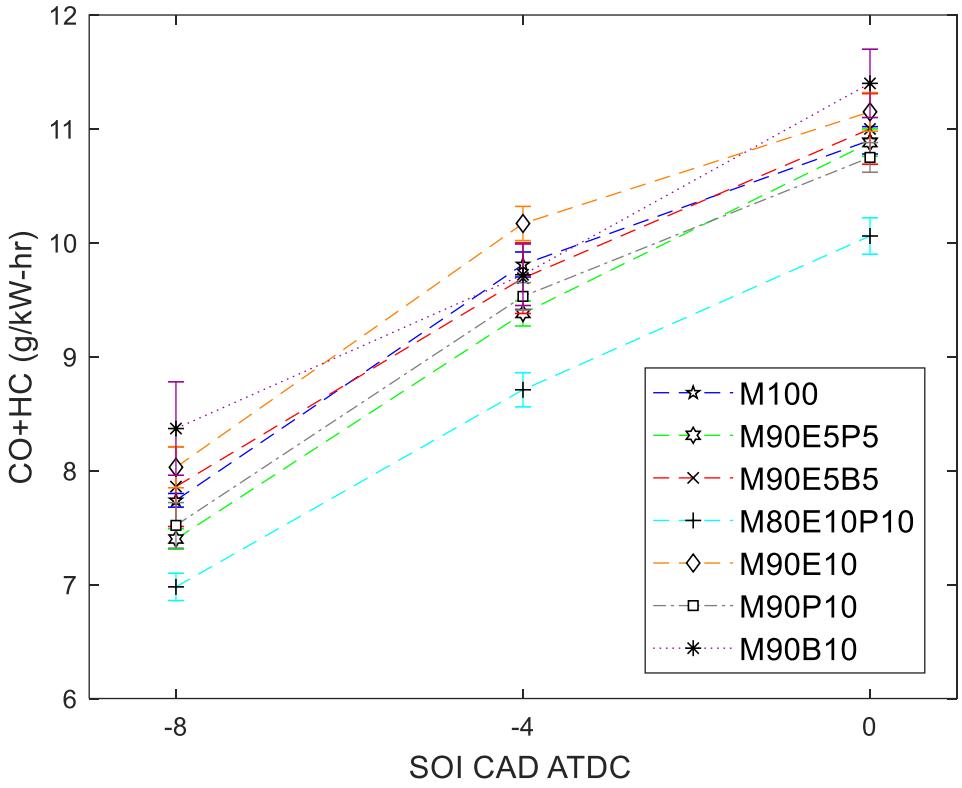

Figure 30- Effect of Gaseous Mixture Composition on Brake Specific CO+HC (Metal Engine, 40% Substitution Rate, 1000 RPM, $P_{inj,diesel}$ = 1000 bar). Error Bars Represent Standard Deviation of the Measurement

Methane emissions are shown in Figure 31. As expected, M100 had the highest methane emissions due to a larger fraction in the composition compared to the rest of the mixtures. This also follows that M80E10P10 had the lowest methane emission values due to a lower fraction of the fuel input being methane. The results followed closely with the C_1-C_4 mass fractions provided in Table 8. The only exception was M90E5B5, which had slightly higher methane emissions than M90P10 even though the mass fraction of methane was lower. However, the magnitude of the reduction did not correlate to the mass fraction. The relative methane emissions compared to M100 normalized to the respective mass fraction of C_1 in the gas blend was used to compare the reduction (see Equation 27). M90E10 had an 8.8% increase in methane emissions over the expected mass fraction reduction. M90E5P5, M90E5B5, and M90P10 had a 5.3%, 5.7%, and 3.2% increase, respectively. The only gas blend to have a lower relative CH_4 value was M90B10, which had a 1.6% decrease.

M80E10P10, despite having the lowest methane emissions, had a 1.9% increase in relative methane emissions. As a result, ethane was found to have a negative effect on methane emissions when the mass fraction of methane in the blend was considered. Furthermore, all gas blends had reduced methane oxidation for delayed SOI_{DIESEL}.

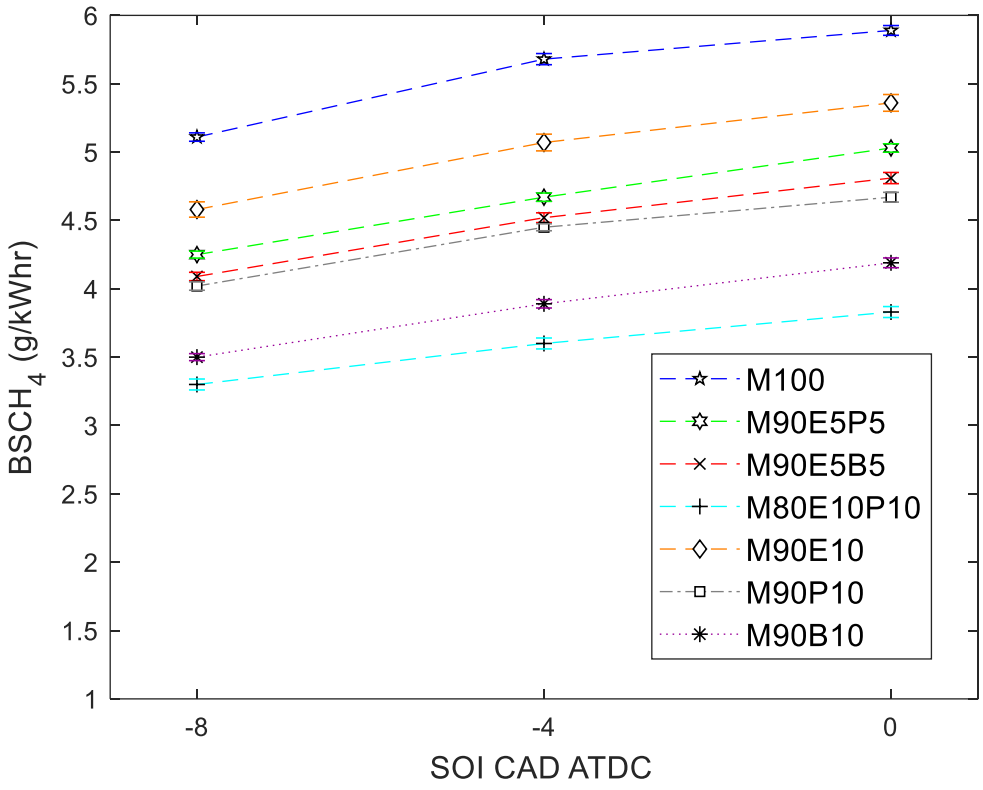

Figure 31- Effect of Gaseous Mixture Composition on Brake Specific CH_4 (Metal Engine, 40% Substitution Rate, 1000 RPM, $P_{inj,diesel}$ = 1000 bar). Error Bars Represent Standard Deviation of the Measurement

The $BSCO_{2,eq}$ presented in Figure 32 was determined using Equation 24. The diesel baseline considered only CO_2 emissions while data for fuel-blends included the GWP of individual species measured. It should be mentioned that NMHC emissions not related to C_1-C_4 species were not included in the analysis. The results show the largest $BSCO_{2,eq}$ occurred for M100, M90E5B5, and M90E10, depending on SOI_{DIESEL}. Due to the large GWP of methane (28), it was expected M100 would have the highest $BSCO_{2,eq}$; however, this was balanced by the reduced CO_2 levels of M100 over M90E5B5 and M90E10. Gas blends with propane had lower $BSCO_{2,eq}$ as compared to ethane mixtures without propane. The combined effect of ethane and propane in reducing engine out emissions were also evident in $BSCO_{2,eq}$ as it was with BSCO. Gas blends with 10% propane or

butane had the lowest overall $BSCO_{2,eq}$. The $BSCO_{2,eq}$ values were sensitive to the SOI_{DIESEL} for certain blends, particularly for M90B10 and M80E10P10 at the MBT timing. All other gas blends had reduced $BSCO_{2,eq}$ for more advanced SOI_{DIESEL}. The largest reduction in magnitude of $BSCO_{2,eq}$ was 51 g/kWh for M80E10P10 compared to M100.

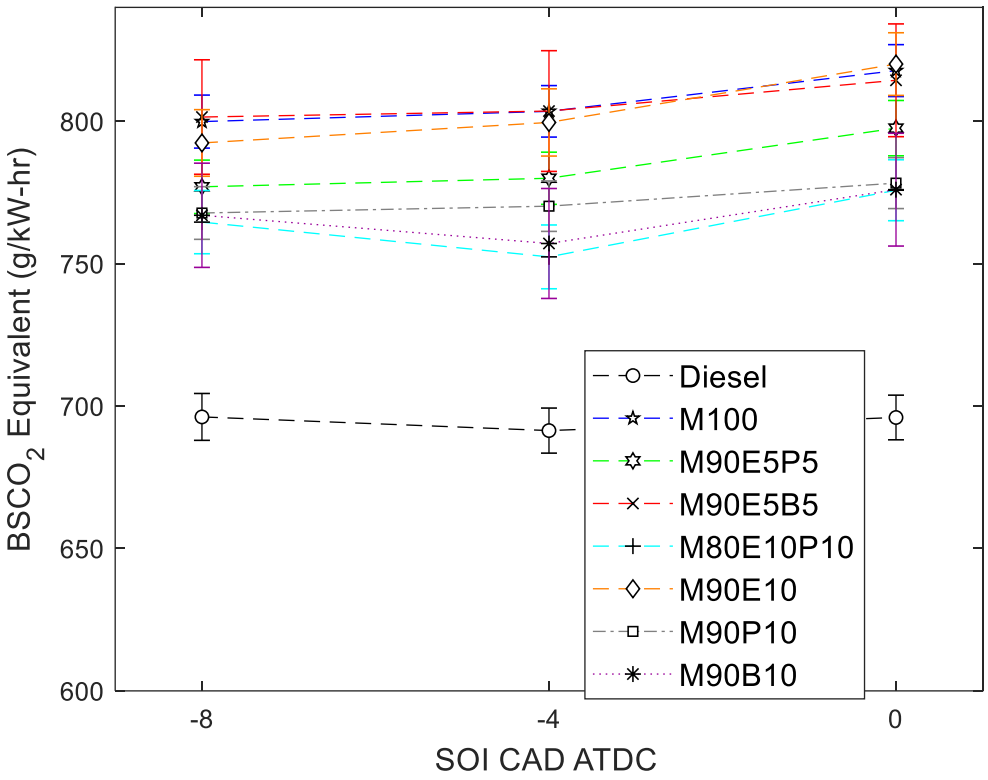

Figure 32- Effect of Gaseous Mixture Composition on $BSCO_2$ Equivalent (Metal Engine, 40% Substitution Rate, 1000 RPM, $P_{inj,diesel}$ = 1000 bar). Error Bars Represent Standard Deviation of the Measurement

To further understand the differences in $BSCO_{2,eq}$ between the gas blends the $BSCO_{2,eq}$ C_1-C_4 contribution (Equation 25) was determined and shown in Figure 33. As expected, M100 had the highest $BSCO_{2,eq}$ C_1-C_4 contribution due to the significantly larger GWP for methane (28) compared to ethane (6), propane (3), and butane (4). The gas blends with 90% methane plus ethane were also subject to a higher GWP scaling than those with propane and butane, therefore leading to moderately increased $BSCO_{2,eq}$ C_1-C_4 contribution. M80E10P10 had the lowest contribution based on impact factor scaling. All gas blends decreased the $BSCO_{2,eq}$ contribution for decreasing methane mass fraction except for M90E5B5, which should have been lower than M90P10. The

largest reduction in magnitude of $BSCO_{2,eq}$ C_1-C_4 contribution was 53 g/kWh for M80E10P10 compared to M100, almost identical to the difference in $BSCO_{2,eq}$. All gas blends had reduction in $BSCO_{2,eq}$ C_1-C_4 contribution for advancing SOI_{DIESEL} unlike $BSCO_{2,eq}$, suggesting less sensitivity to BMEP.

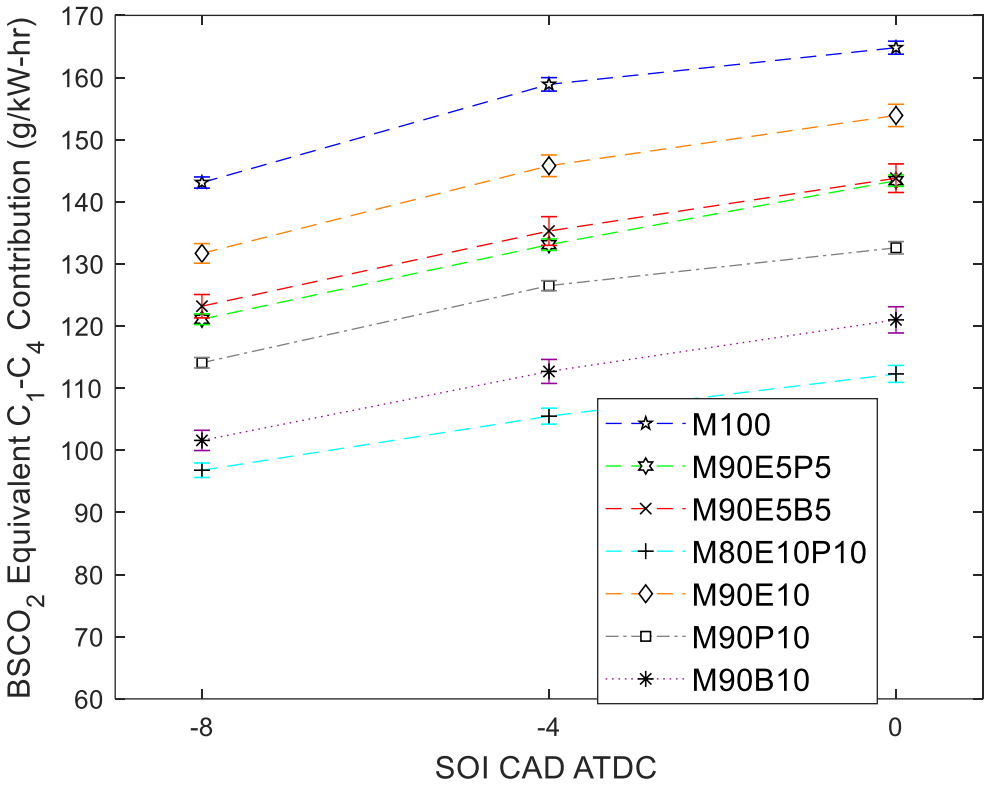

Figure 33- Effect of Gaseous Mixture Composition on $BSCO_2$ Equivalent C_1-C_4 Contribution (Metal Engine, 40% Substitution Rate, 1000 RPM, $P_{inj,diesel}$ = 1000 bar). Error Bars Represent Standard Deviation of the Measurement

The maximum in-cylinder temperature in Figure 34 shows advancing SOI_{DIESEL} increased bulk gas temperature for dual-fuel operation but decreased for the diesel baseline. Based on literature [28], the adiabatic flame temperature over a wide range of equivalence ratios is the highest for butane followed by propane, ethane, and methane. The difference was not substantial between butane and propane, but methane should have a noticeably lower value. This expected trend was not evident in the dual-fuel combustion data, with M100 having a higher maximum in-cylinder temperature than half of the blends. All tertiary gas blends had a higher peak temperature than M100 while binary blends were lower. Even though the temperature was lower than M100 the binary mixtures increased as expected with (M90B10>M90P10>M90E10) except for M90B10 at

the most advanced SOI_{DIESEL}. For the tertiary gas blends, it was expected that fuel M80E10P10 would produce the highest peak temperature due to reduced methane content. Interestingly, M90E5B5 had the highest indicated peak temperature for all operating conditions, which correlated to higher NO_x and CO_2 emissions. This would suggest better NG fuel oxidation resulted in more heat release occurring which elevated thermal NO_x, but the first AHRR peak was lower than most gas blends. M90E5B5 also had the lowest thermal efficiency, highest BSFC, highest BMEP to IMEP ratio, and nearly the same BMEP as M100. Therefore, the increased CO_2 and NO_x were not simply related to decreased power but rather differences in measured emissions.

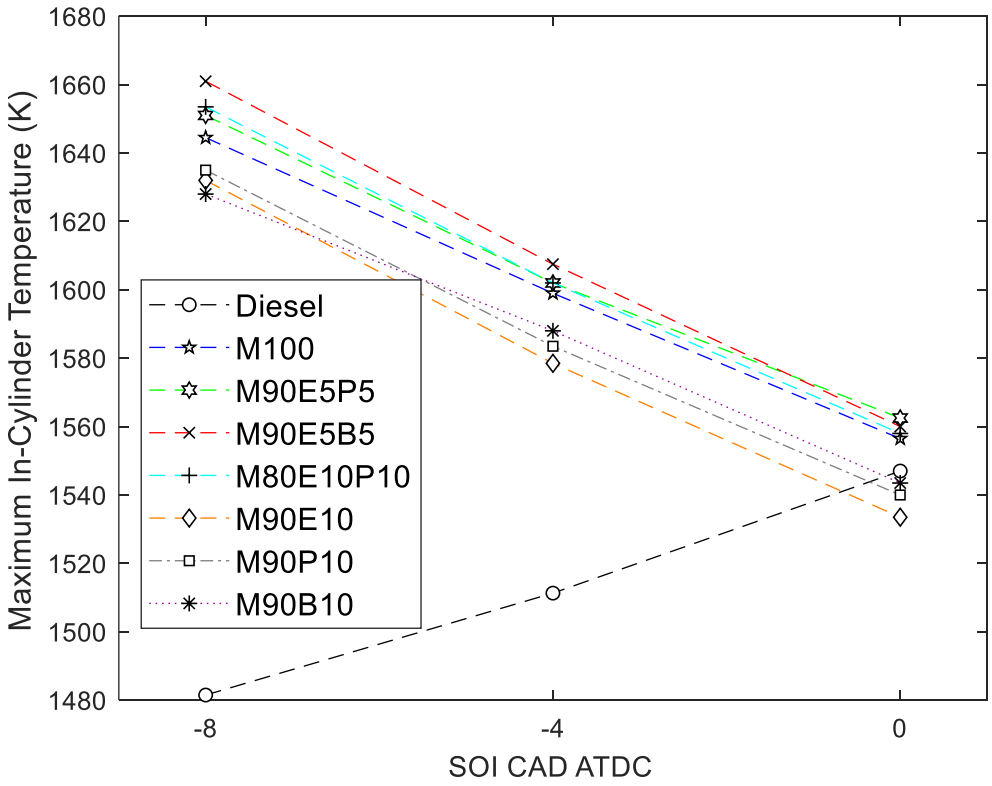

Figure 34- Effect of Gaseous Mixture Composition on Maximum In-Cylinder Temperature (Metal Engine, 40% Substitution Rate, 1000 RPM, $P_{inj,diesel}$ = 1000 bar). Error Bars Represent Standard Deviation of the Measurement

Figure 35 shows that M100 had the highest exhaust temperature (measured in the vicinity of the exhaust port) of all the fuel compositions tested, and M90B10 had the lowest exhaust temperature. The differences for other blends were rather small, yet compared to the diesel baseline there was a ~40-50 °C increase for dual-fuel operation. While the exhaust temperature did not correlate with maximum in-cylinder temperature trends, it increased with delayed SOI_{DIESEL} compared to the

opposite for the maximum in-cylinder temperature. The data on exhaust temperature was mainly provided to allow for after-treatment considerations on the potential catalyst efficiency at the given operating conditions.

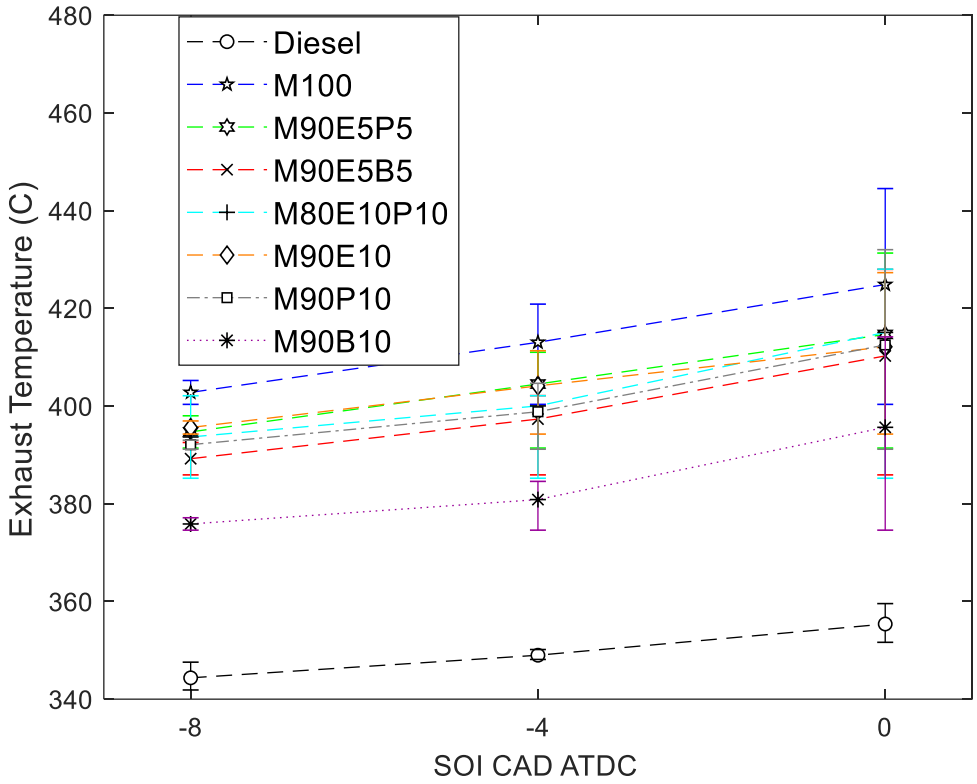

Figure 35- Effect of Gaseous Mixture Composition on Exhaust Temperature (Metal Engine, 40% Substitution Rate, 1000 RPM, $P_{inj,diesel}$ = 1000 bar). Error Bars Represent Standard Deviation of the Measurement

Figure 36 shows the pressure knocking intensity (PKI), which is a good indicator of knock severity. PKI represents the maximum amplitude of the raw pressure transducer signal after using a 6 kHz bandpass filter (i.e., the first transverse mode of gas vibration) [11]. All dual-fuel conditions increased PKI for delayed SOI_{DIESEL}, however the diesel baseline increased PKI with advance SOI_{DIESEL}. While the mean value for each gas blend was within the standard deviation of all others, some conclusions can still be inferred. Gas blends with 10% propane had the highest PKI for SOI_{DIESEL}=-4 CAD ATDC and TDC, even though butane has a lower auto-ignition temperature. For the most advanced injection timing, M90B10 PKI was nearly identical to that of the 10% propane fuels. The lowest dual-fuel PKI was for M100, which was a result of higher auto-ignition temperature and low propensity for knock [116]. PKI suggests gas blends with butane would have

the most severe knock followed by propane then ethane. This was only true for the most advanced SOI_{DIESEL} for M90B10, however M90E5B5 had an average PKI compared to other fuels. Also, fuel M90E10 should have the second lowest propensity to knock but had a higher PKI than M90E5B5, M90E5P5, and even M90B10 for SOI_{DIESEL}=TDC. A higher PKI was not directly related to increased thermal efficiency or BMEP.

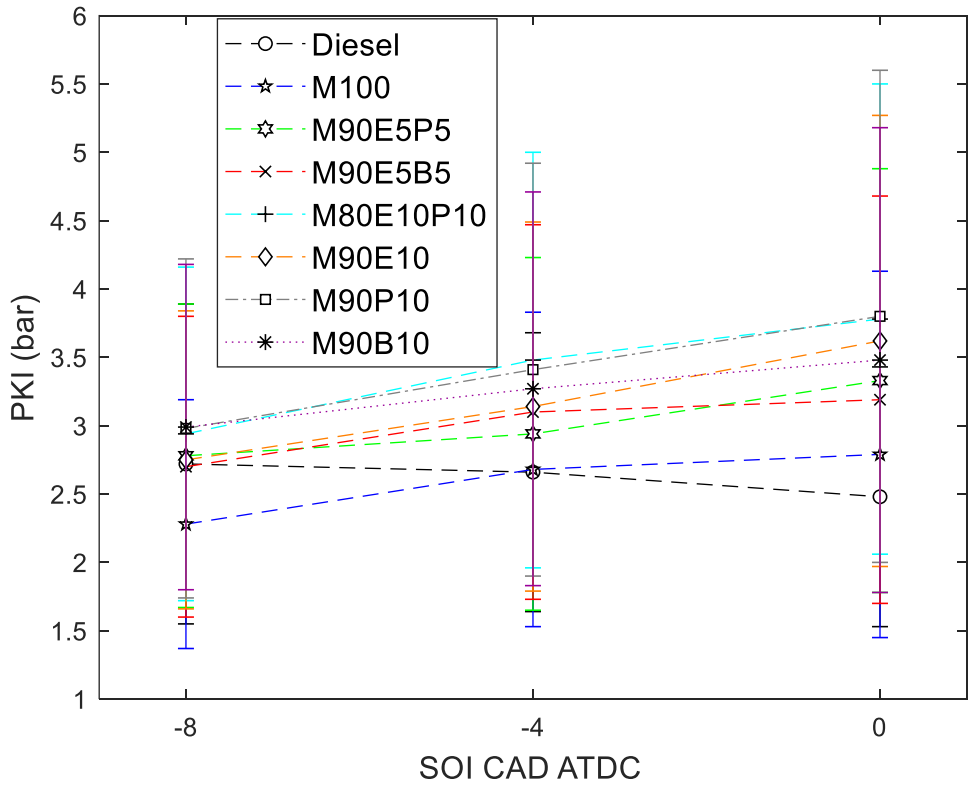

Figure 36- Effect of Gaseous Mixture Composition on PKI (Metal Engine, 40% Substitution Rate, 1000 RPM, $P_{inj,diesel}$ = 1000 bar). Error Bars Represent Standard Deviation of the Measurement

The ringing intensity (RI) in Figure 37 (see Equation 26 for its methodology) shows a substantial difference for dual-fuel cases compared to diesel baseline. The results indicate that dual-fuel conditions experience a higher degree of knocking than the diesel baseline. As indicated in [112], a RI value greater than 5 MW/m^2 correlates with the onset of knocking. While the maximum indicated in-cylinder temperature is lower for SOI_{DIESEL}=TDC in dual-fuel cases, the increased RI can be attributed to a higher pressure rise rate after TDC. Furthermore, gas blends with butane show less propensity to knock as compared to C_1-C_3 blends. Conversely, the blends with more propane show the highest likelihood to knock. The lowest RI for M90B10 and M90E5B5 was the

opposite of the expected maximum based on the propane knock index [116]. This suggests the propane knock index plays a more significant role for dedicated NG engines compared to dual-fuel, or that an increased rate of pressure rise was not directly related to increased knocking in this case. The RI did agree with the pressure knock intensity for M80E10P10 and M90P10. The RI was found to be more sensitive to the rate of pressure rise than maximum temperature or cylinder pressure.

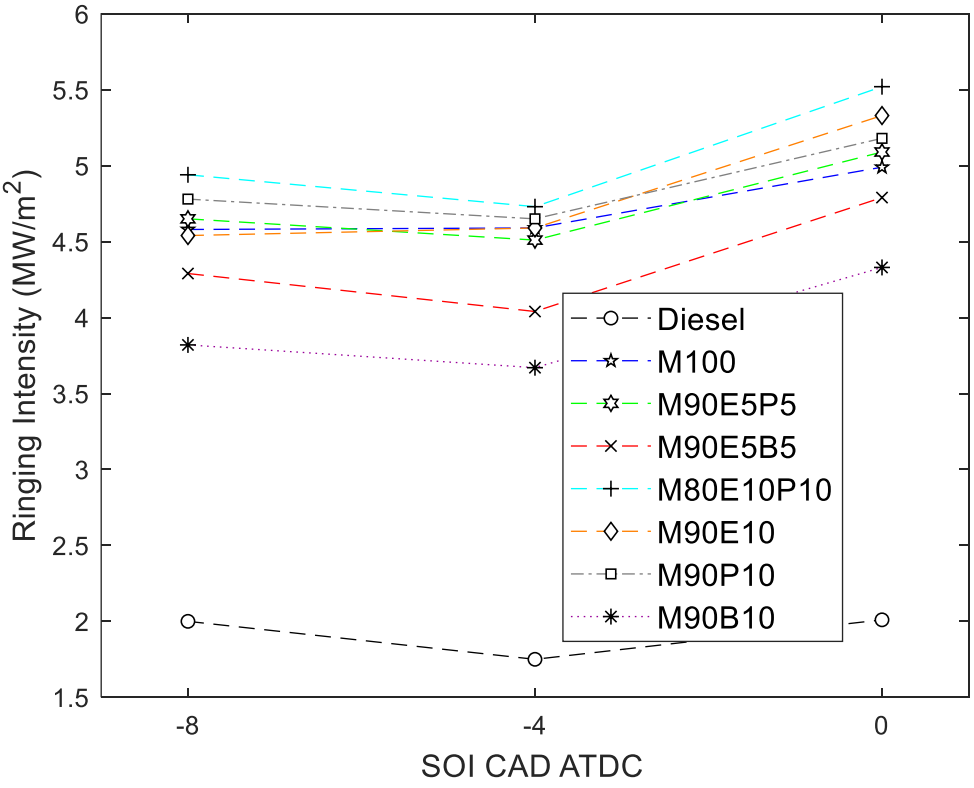

Figure 37- Effect of Gaseous Mixture Composition on Ringing Intensity (Metal Engine, 40% Substitution Rate, 1000 RPM, $P_{inj,diesel}$ = 1000 bar). Error Bars Represent Standard Deviation of the Measurement

4.4: Effect of Natural Gas Composition in Optical Engine Experiments at 63% (by Energy) Diesel Replacement

This section will present and discuss the effect of the main NG components (i.e., methane, ethane, and propane) on dual-fuel engine performance and emissions, as indicated by in-cylinder pressure data and natural luminosity images. For simplicity, the diesel baseline, methane-diesel, ethane-diesel, and propane-diesel cases will be mentioned in the text as diesel, methane, ethane, and propane, respectively. Diesel-only operation at the same diesel mass per cycle as for the dual-fuel

operation (therefore a lower IMEP) is presented to help visualize the effect of adding the gas to the engine performance. To differentiate from RCCI experiments, traditional diesel injection timing (SOI_{DIESEL}=-8 CAD ATDC) will be referred to in this section as MCCI.

SOI_{DIESEL} changes the heat release phasing, which impacts engine performance and emissions. Figure 38 shows the diesel injection duration as a pulse alongside the accompanying heat release rate for RCCI and MCCI for C_1-diesel combustion. While RCCI operation relies on the increasing in-cylinder temperature near TDC to initiate the combustion event, the delay from injection command to combustion event is substantial. Likewise, for MCCI the in-cylinder temperature is already conducive for combustion to begin by the time the diesel injection occurs. MCCI heat release delay is primarily due to fuel atomization delay. Furthermore, the short delay from end of diesel injection to start of combustion results in clear visualization of the diesel spray jets in the resulting combustion imaging.

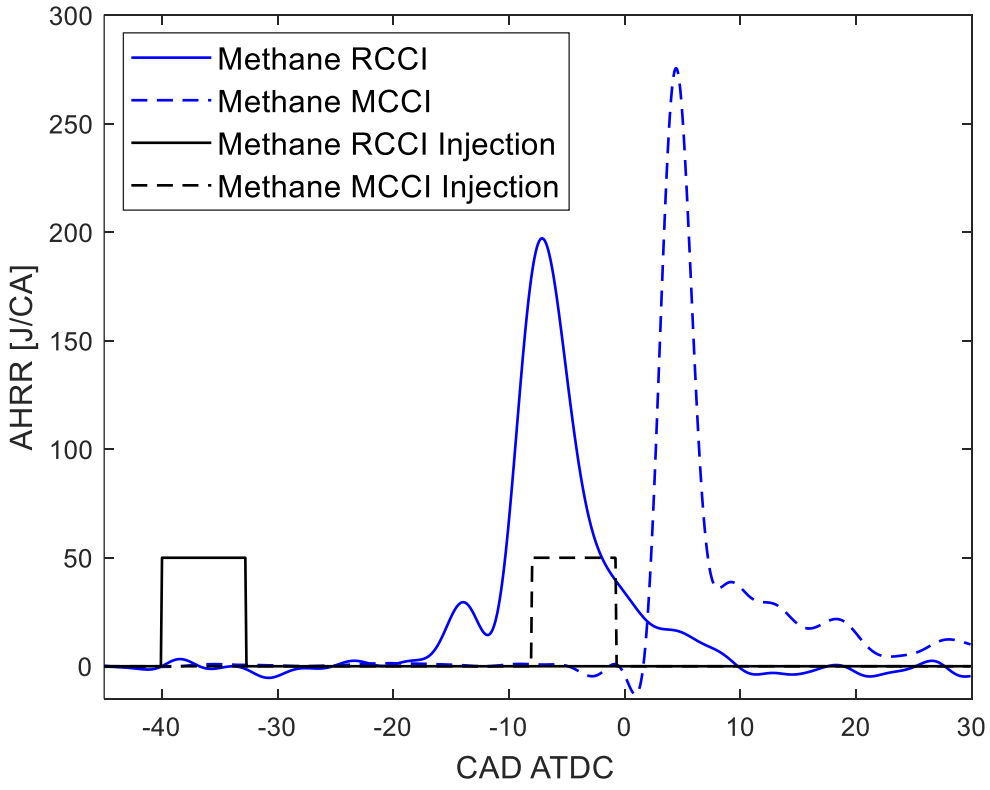

Figure 38- Effect of Diesel Injection Timing on Apparent Heat Release Rate for Methane-Diesel Combustion (Optical Engine, 63% Substitution Rate, 1000 RPM, $P_{inj,diesel}$ = 500 bar).

A primary concern for dual-fuel diesel-NG applications with port fuel gas injection is the gas slip during the valve overlap, especially at high boost pressures as in this study. Therefore, preliminary experiments that measured hydrocarbon emissions under both firing and non-firing conditions determined the number of gas injectors, nozzle diameter, and gas injection timing and duration that would maximize engine output, hence minimize the gas slip. In addition, measurements of delivered air and gas mass matched reasonably in-cylinder mass estimates based on exhaust data, suggesting that mixture slip out during valve overlap did not influence the analysis presented next. However, data showed that the low ϕ for the gaseous mixture (~0.3) resulted in a large fraction of unburned hydrocarbons in the fired cycles, and those hydrocarbons consisted almost exclusively of unburned fuel from the original in-cylinder air-gas mixture, a consequence of the optical piston design (e.g., a larger than normal crevice volume, flat bowl with straight walls, etc.). As a result, the actual mass of gas that combusted in a fired cycle was much lower than the delivered ESR, as it will be shown later.

4.4.1: Effect of Natural Gas Composition in Optical Engine Experiments in RCCI mode (SOI_{DIESEL} = -40 CAD ATDC)

Diesel injection duration in the RCCI Mode was relatively short, at 1.2 ms. The start and end of fuel injection command was -40 CA ATDC and -32.8 CA ATDC, respectively. Based on averaged in-cylinder pressure measurements, Figure 39 shows clear differences in combustion phasing between diesel-only and dual-fuel operation. The diesel pressure trace represents the quantity used as a base for all three dual-fuel conditions. Noticeable differences in the start of combustion can be inferred from the deviation in pressure traces which begins much earlier for the diesel-only case, showing similar ignition delay tendencies for the three NG components compared to diesel-only. The magnitude and location of peak pressure for the propane case was clearly higher (~2-3 bar) and more advanced (~1 CAD) compared to ethane and methane which had overlapping features.

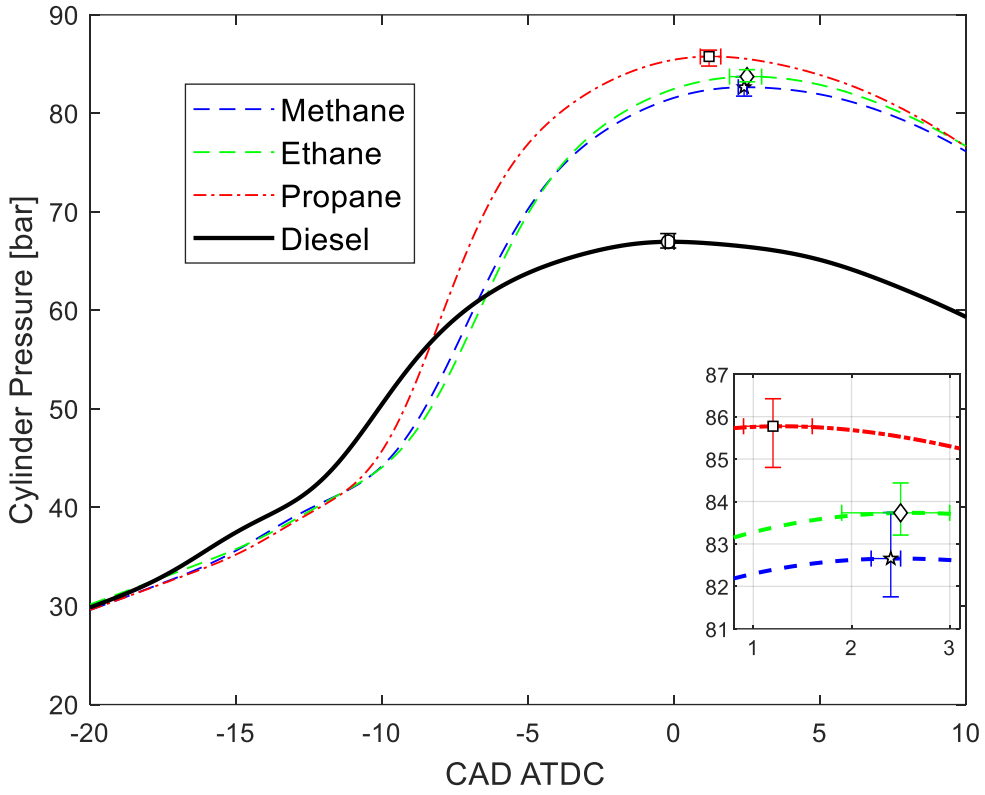

Figure 39- Effect of Gaseous C_1-C_3 Components on In-Cylinder Pressure (Optical Engine, RCCI Mode, 63% Substitution Rate, 1000 RPM, $P_{inj,diesel}$ = 500 bar). Error Bars Represent Standard Deviation of the Measurement

The apparent heat release rate (AHRR) shown in Figure 40 provided more detail on the combustion phasing differences resulting from different NG components. Compared to the diffusion-controlled mode, RCCI is characterized by a larger low temperature heat release (LTHR). The AHRR shows that the diesel-only case LTHR starts at -19 CAD ATDC followed by methane at -17 CAD ATDC, and ethane and propane at ~ -16 CAD ATDC. There is a distinct decrease in heat release rate when transitioning into the high temperature heat release (HTHR) for both diesel and methane cases while there is a more constant HRR for ethane and propane during this transition. The angle of HTHR peak for diesel-only (118 J/CA) occurs at -10 CAD ATDC followed by propane (253 J/CA) at -8 CAD ATDC, methane (197 J/CA) at -7.2 CAD ATDC, and ethane (202 J/CA) at -6.7 CAD ATDC. The ethane case shows the most delay in LTHR of the dual-fuel cases, but a slightly higher peak value as compared to methane.

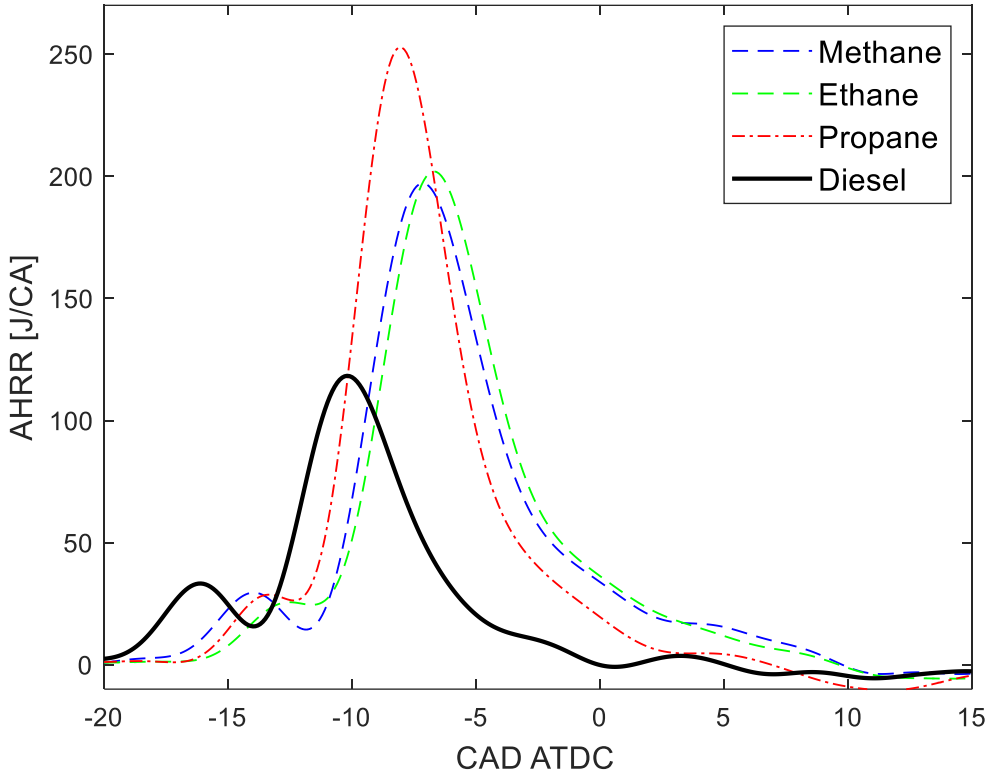

Figure 40- Effect of Gaseous C_1-C_3 Components on Apparent Heat Release Rate (Optical Engine, RCCI Mode, 63% Substitution Rate, 1000 RPM, $P_{inj,diesel}$ = 500 bar)

The cumulative heat release in Figure 41 provides further detail on the differences in LTHR, again with methane having the least delay in start of heat release but propane quickly surpassing it once combustion is initiated. It also suggests an equal contribution of diesel and gas in terms of energy released, which based on the delivered ESR, a larger gas fraction did not participate in the combustion process, and that fraction did not change substantially between the three gases. The total heat release (occurring slightly after the 10 CAD ATDC shown in Figure 40) for diesel, methane, ethane, and propane was 736 J, 1404 J, 1384 J, and 1420 J, respectively. While the rate of energy release was slightly faster for methane RCCI than for ethane RCCI (with negligible differences after TDC), it was considerably faster for propane RCCI once combustion is initiated. It also affected in-cylinder bulk gas temperature, with propane creating a notably hotter in-cylinder environment between -8 CAD and 5 CAD ATDC than methane and ethane.

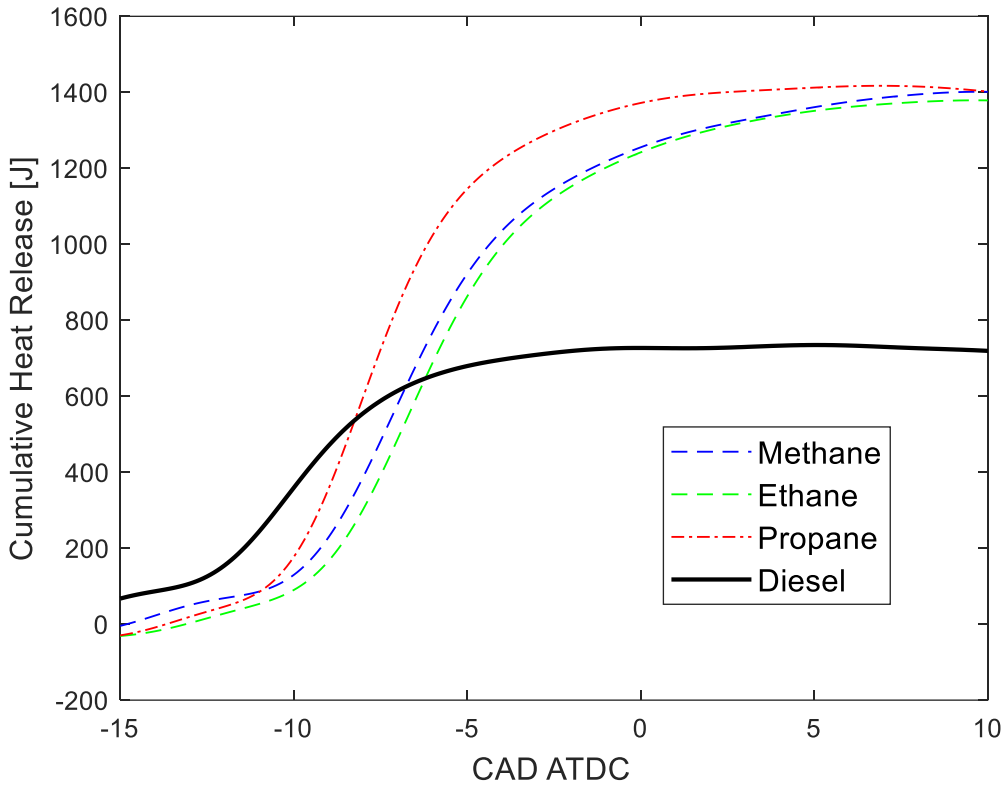

Figure 41- Effect of Gaseous C_1-C_3 Components on Cumulative Heat Release (Optical Engine, RCCI Mode, 63% Substitution Rate, 1000 RPM, $P_{inj,diesel}$ = 500 bar)

The in-cylinder bulk gas temperature was inferred from the cylinder pressure traces and trapped mass in-cylinder at intake valve closing using Van Der Waals equation of state. The impact of the different fuels on in-cylinder bulk gas temperature, Figure 42, shows propane (1608 K) had a slightly higher peak temperature than methane (1565 K) and ethane (1541 K). This could be due to the ranking of adiabatic flame temperature (T_{ad}) between gases ($T_{ad,C3} > T_{ad,C2} > T_{ad,C1}$) [124], or simply the differences in combustion phasing.

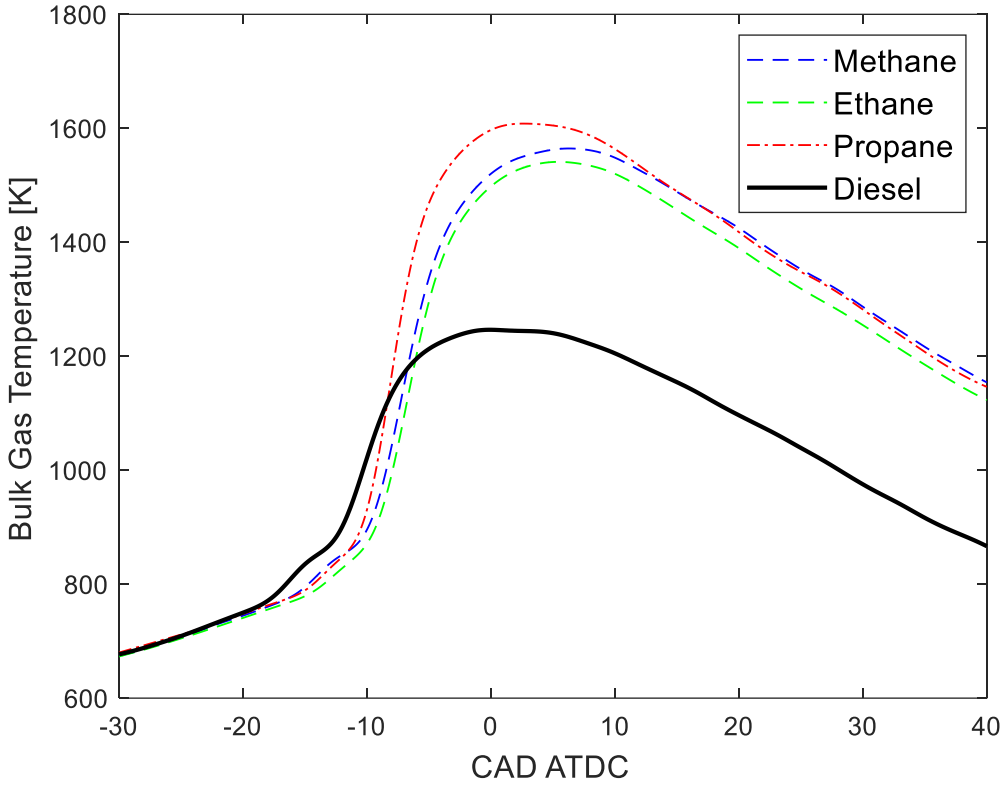

Figure 42- Effect of Gaseous C_1-C_3 Components on Bulk Gas Temperature (Optical Engine, RCCI Mode, 63% Substitution Rate, 1000 RPM, $P_{inj,diesel}$ = 500 bar)

Figure 43 shows indicated pressure analysis results. First, methane, ethane, and propane addition increased IMEP to 6.7, 6.6, and 6.5 bar, respectively, compared to an IMEP of 3 bar for the diesel only operation. The small IMEP differences between the RCCI cases were due to differences in combustion phasing, with methane RCCI having the CA50 closer to TDC than the others, hence a more optimum combustion phasing. Furthermore, the end of combustion (EOC) with earlier CA90 corresponded to lower IMEP. Only methane and propane cases had IMEP values separated outside the standard deviation. The COV of IMEP was high with lower repeatability for the diesel case but remained below 3% for the dual-fuel cases. The COV of IMEP was 5.9%, 2.6%, 2.7,% and 2.9% for diesel, methane, ethane, and propane respectively. The rate of pressure rise ($dP/d\theta$) was 4.5 bar/CAD, 7.0 bar/CAD, 7.6 bar/CAD, and 9.5 bar/CAD for diesel, methane, ethane, and propane, respectively. The higher rates of pressure rise corresponded to lower autoignition temperatures for the dual-fuel cases and earlier combustion phasing. The pressure rise rate for propane also approached the upper allowable limit for experiments of 10 bar/CAD, which was set to avoid destruction of optical components.

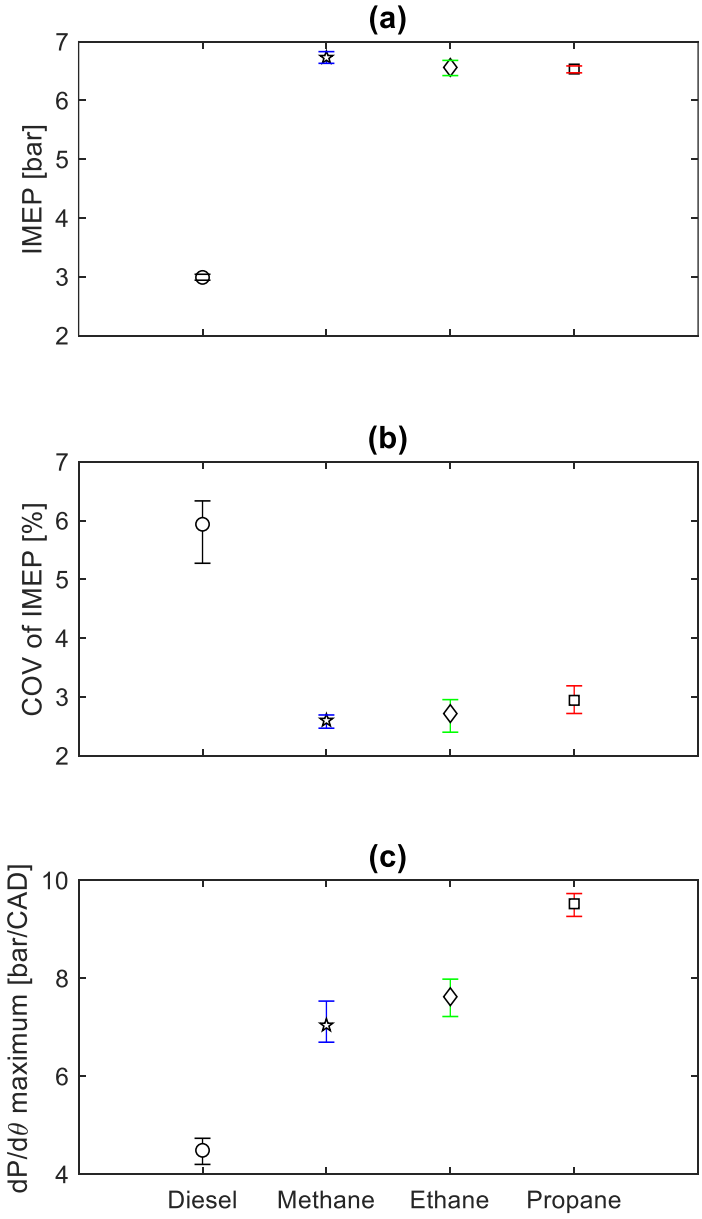

Figure 43- Effect of Gaseous C_1-C_3 Components on (a) IMEP , (b) COV of IMEP, (c) Maximum Pressure Rise Rate (Optical Engine, RCCI Mode, 63% Substitution Rate, 1000 RPM, $P_{inj,diesel}$ = 500 bar). Error Bars Represent Standard Deviation of the Measurement

The differences in combustion phasing are presented in Figure 44. The start of combustion (SOC) indicated by CA10 (associated here with CA10—the crank angle corresponding to 10% cumulative heat release (CHR)) shows the increased ignition delay for diesel only compared to all dual-fuel cases. CA10 was delayed from -14.7 CAD ATDC for the diesel case to -9.8 CAD ATDC, -9.5 CAD ATDC, and -8.8 CAD ATDC for propane, methane, and ethane, respectively. CA50

(50% CHR) followed the same trend as CA10, with diesel the most advanced (-9.8 CAD ATDC) followed by propane (-7.5 CAD ATDC), methane (-6.4 CAD ATDC), and ethane (-6 CAD ATDC). For all three dual-fuel cases the CA10 and CA50 differences remained within repeatability bands as indicated by error bars in the plot. The EOC, specified by CA90 (90% CHR), shows the largest differences in combustion phasing of the three phasing parameters. CA90 shows diesel combustion finished well before TDC (-6.1 CAD ATDC) with propane at -3.3 CAD ATDC, methane at 0.1 CAD ATDC, and ethane at -0.2 CAD ATDC. The differences in EOC between propane and methane/ethane were clearly distinguished from one another and outside the repeatability bands.

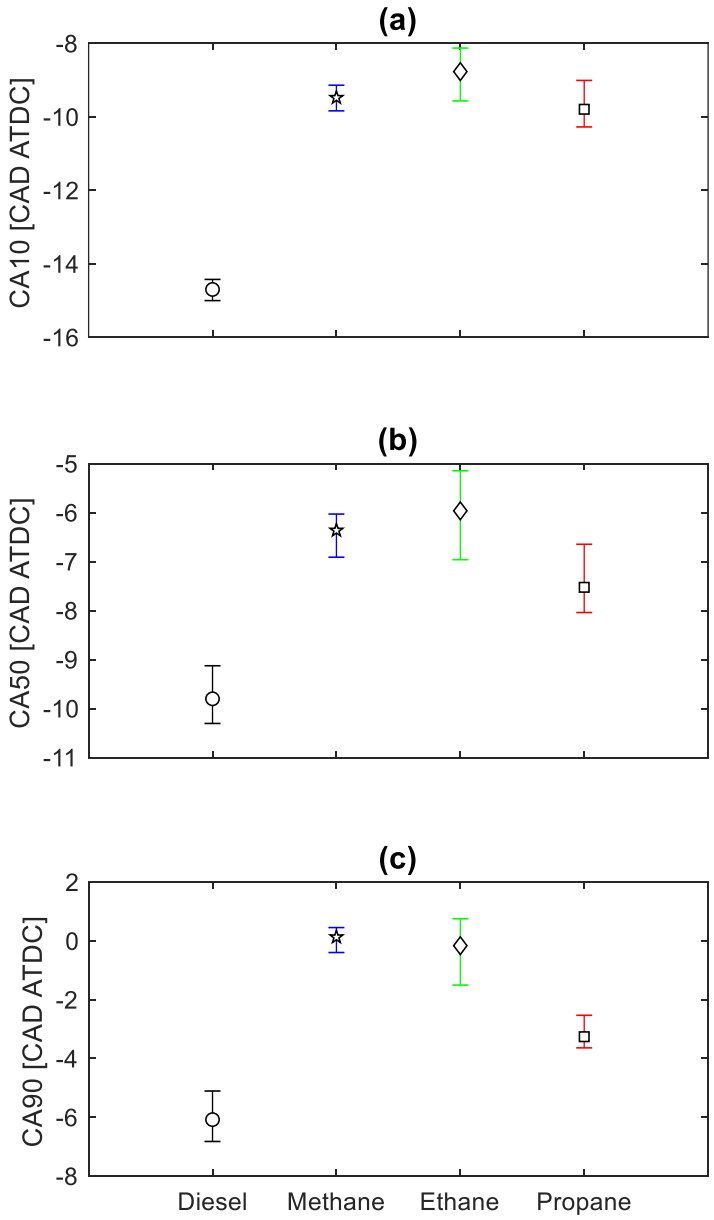

Figure 44- Effect of Gaseous C_1-C_3 Components on (a) CA10, (b) CA50, (c) CA90 (Optical Engine, RCCI Mode, 63% Substitution Rate, 1000 RPM, $P_{inj,diesel}$ = 500 bar). Error Bars Represent Standard Deviation of the Measurement

Figure 45 shows the trapped air mass, peak motoring pressure, and total heat release. The trapped air mass remained at ~2.3-2.4 g/cycle for all tests, with deviations all showing some level of overlap. The same occurred for peak motoring pressure, with an average of ~46.5 bar. The total heat release in J was roughly double for the dual-fuel cases compared to the base diesel 1.2 ms

injection used for all cases. Methane and propane had a slightly higher total heat release as detailed in the Figure 41 discussion.

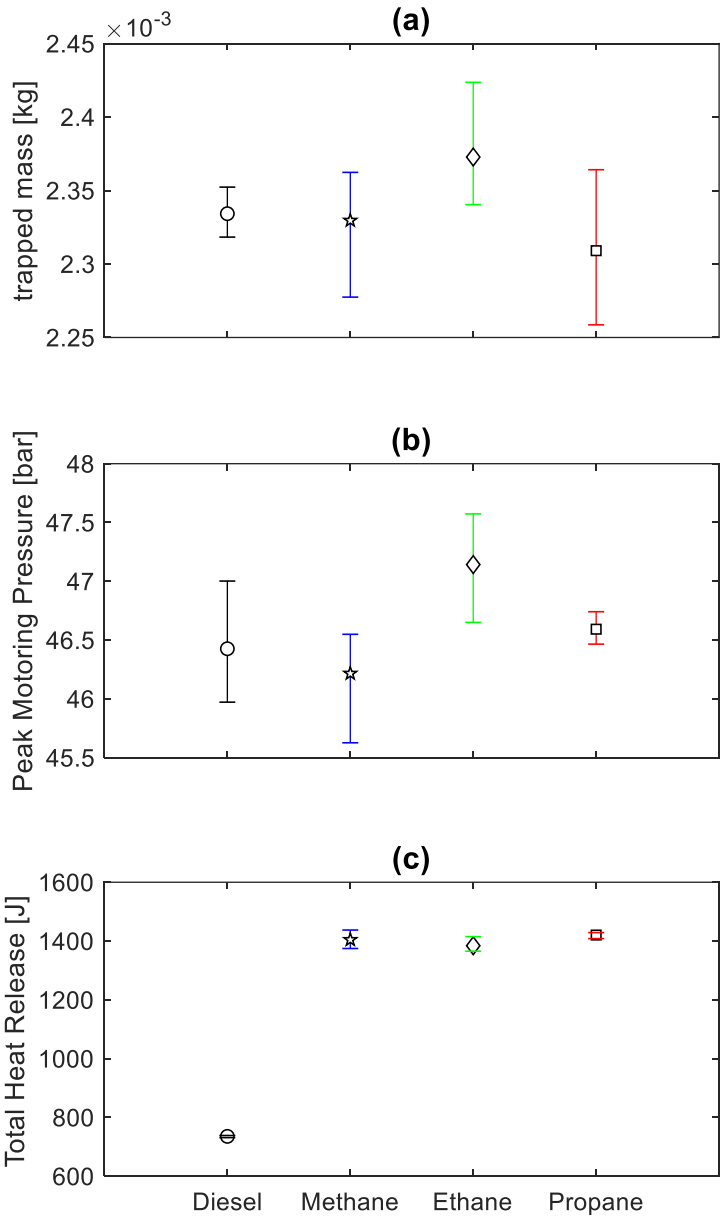

Figure 45- (a) Trapped Mass, (b) Peak Motoring Pressure, (c) Effect of Gaseous C_1-C_3 Components on Total Heat Release (Optical Engine, RCCI Mode, 63% Substitution Rate, 1000 RPM, $P_{inj,diesel}$ = 500 bar). Error Bars Represent Standard Deviation of the Measurement

The ignition delay shown in Figure 46 (defined as SOI_{DIESEL} - CA10, in CAD) was excessive, as expected for RCCI mode. This resulted in an ignition delay of 25.3 CAD, 30.5 CAD, 31.2 CAD, and 30.2 CAD for diesel, methane, ethane, and propane, respectively. The addition of NG

components increased the delay by at least 5 CAD, with propane having slightly less delay than methane and ethane. The combustion duration, CA90-CA10, was 8.6 CAD, 9.6 CAD, 8.6 CAD, and 6.5 CAD for diesel, methane, ethane, and propane, respectively, with higher variability in the diesel and ethane cases. The knocking intensity (PKI for metal engine and not shown here) was 0.94 bar, 1.00 bar, 1.02 bar, and 1.14 bar for diesel, methane, ethane, and propane respectively, which correlated with the rate of pressure rise. In comparison, the RI, another knock intensity metric, did not indicate heavy knocking (RI>5 MW/m^2) [112] but it did show a more substantial increase for the propane case. The RI was 0.70 MW/m^2, 1.56 MW/m^2, 1.79 MW/m^2, and 2.78 MW/m^2 for diesel, methane, ethane, and propane. That relates to a 15% and 78% increase compared to methane for ethane and propane, respectively.

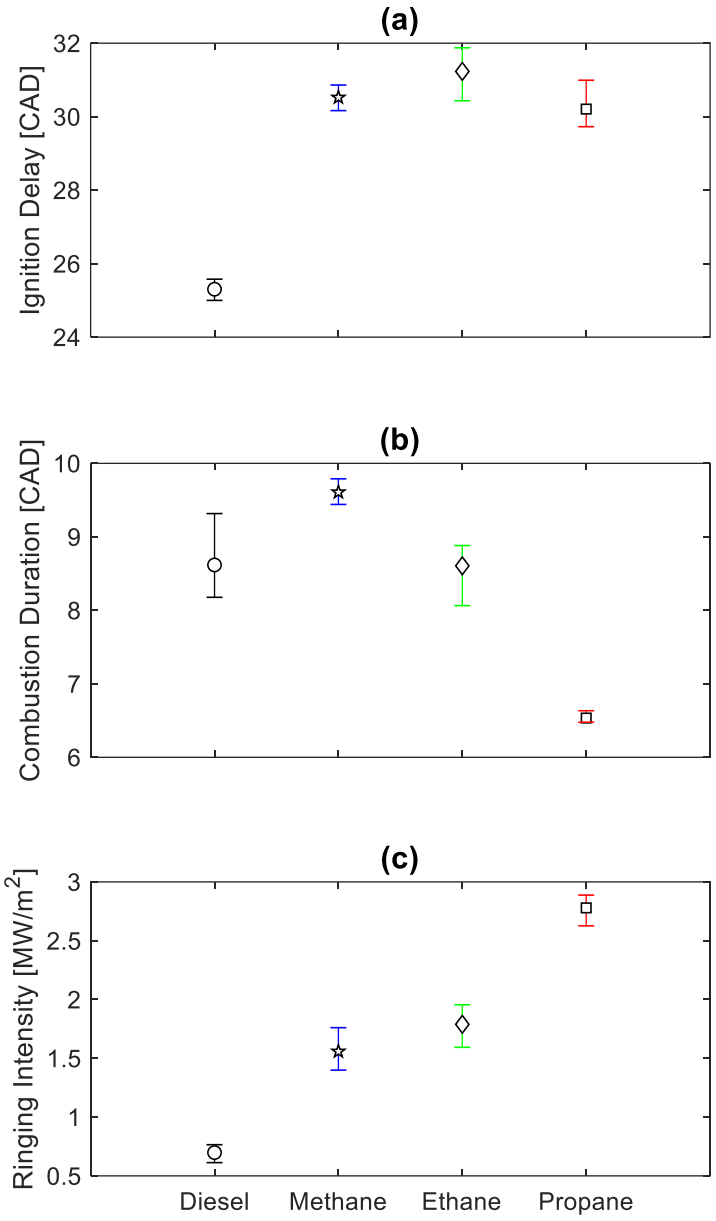

Figure 46- Effect of Gaseous C_1-C_3 Components on (a) Ignition Delay, (b) Combustion Duration, (c) Ringing Intensity (Optical Engine, RCCI Mode, 63% Substitution Rate, 1000 RPM, $P_{inj,diesel}$ = 500 bar). Error Bars Represent Standard Deviation of the Measurement

As previously mentioned, the NG was assumed to have the same slip rate for all three fuels, but clearly the NG emission measurements show a different result. The differences are thought to be attributed to different measurement ranges of the FTIR emission analyzer, (0-3000 ppm for methane, 0-500 ppm for ethane, and 0-200 ppm for propane). Figure 47 details the data used to determine NG MFB in Figure 48. Measurements for non-firing data were 8.5%, 245%, and 546%

over-range for methane, ethane, and propane, respectively; while the firing data was within range for methane, but 50% and 261% over-range for ethane and propane. Equation 30 was used to correct for over-ranged emission samples and was based on experimentally determined calibration curves. As diesel is the ignition source in the dual fuel experiments, the data for non-firing emissions was collected by motoring the engine to 1000 RPM and enabling the gaseous fuel injection prior to commanding the diesel injection. The measured steady-state emissions values corresponded to the maximum background gas emission possible (i.e., completely unburnt gas) for the gas injection duration and timing of interest. This method was also used to determine the best EOI_{NG} for maximum trapping of gas in the cylinder under the high intake boost pressure. EOI_{NG} was selected by comparing the background to minimum combustion data emissions achievable.

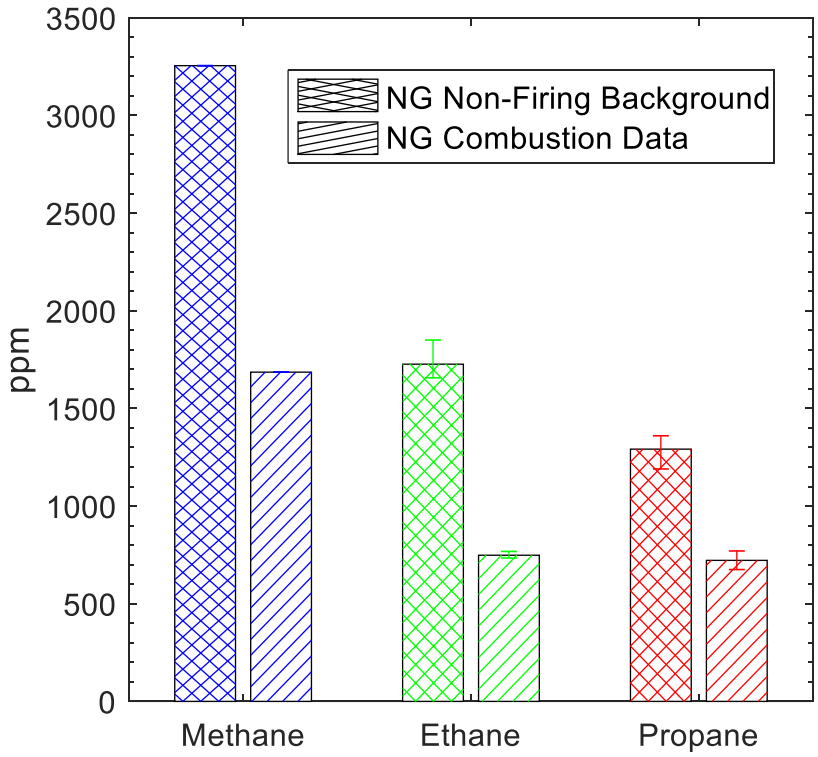

Figure 47- Effect of Gaseous C_1-C_3 Components on Gaseous Fuel Emissions for Firing and Non-Firing Data (Optical Engine, RCCI Mode, 63% Substitution Rate, 1000 RPM, $P_{inj,diesel}$ = 500 bar). Error Bars Represent Standard Deviation of the Measurement

Figure 48 shows fuel conversion metrics as well as emissions and the NG fuel mass delivered per cycle. NG MFB (the reduction in NG emission concentration from non-firing to firing) detailed in

Equation 28 indicated efficiency, and ESR. NG MFB shows the largest reduction in emission concentration for ethane (56.5%), followed by methane (48.2%), and propane (43.8%). The indicated efficiency was similar for the dual-fuel cases but higher for the diesel base, at 28.2%, 23.1%, 22.6%, and 22.2% for diesel, methane, ethane, and propane, respectively. The low dual-fuel efficiency was a consequence of the high boost rate, NG fuel slip, ultra-lean premixed air-fuel ratio, and incomplete combustion. Modified energy substitution (Equation 29) was also shown for dual-fuel cases (45.6%, 49.6%, and 43.6% for methane, ethane, and propane, respectively). Supplied ESR was ~63% for all dual-fuel cases, which represents delivered NG fuel energy in proportion to diesel energy. Modified energy substitution rate, which accounts for fuel slip based on emission measurements, was lower due to fuel slip directly into the exhaust before the exhaust valve closes and the compression stroke begins. This was representative of the 40% ESR used on metal engine experiments, which did not have as much gas slip due to lower boosting pressures. Further, the premixed equivalence ratio corrected by emissions data (NG MFB) was lowered considerably to ~0.14-0.15.

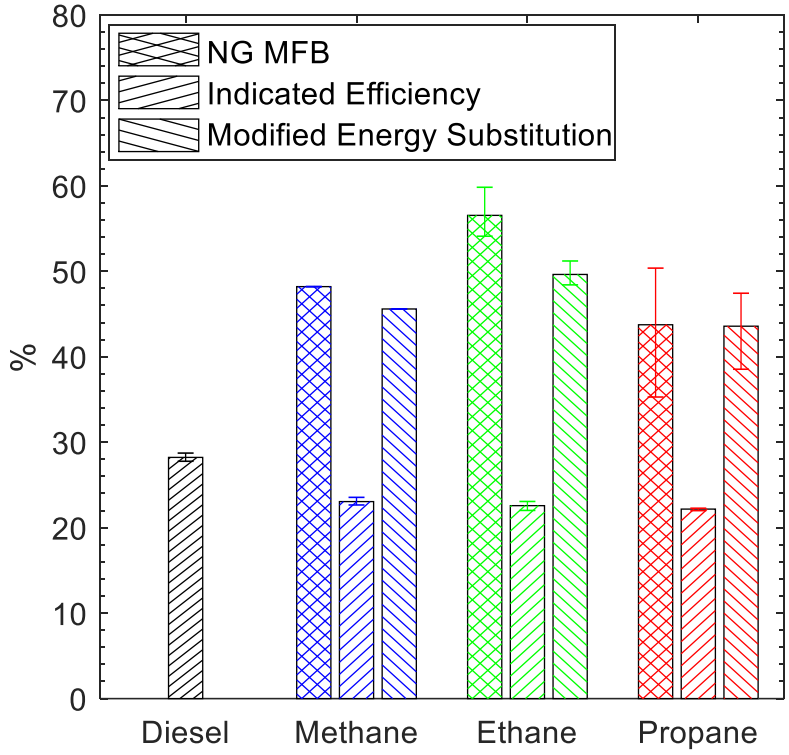

Figure 48- Effect of Gaseous C_1-C_3 Components on Natural Gas MFB, Indicated Efficiency, and Modified Energy Substitution Rate (Optical Engine, RCCI Mode, 63% Substitution Rate, 1000 RPM, $P_{inj,diesel}$ = 500 bar). Error Bars Represent Standard Deviation of the Measurement

Figure 49 shows CO and NO emissions as well as the delivered fuel mass. Diesel-only emissions are discussed first as it can help explain the RCCI emissions trend. CO emissions show the diesel base did not burn completely on its own at the highly advanced injection timing. The low diesel mass flow and advanced SOI_{DIESEL} created a premixed mixture with a low ϕ, hence more incomplete fuel oxidation and higher CO emissions. But the increase in ϕ for the dual-fuel RCCI cases decreased CO emissions substantially, from ~70 g/kWh for diesel-only to ~15 g/kWh for RCCI cases, with propane RCCI having slightly higher CO emissions than the other two RCCI cases. CO emissions were 69 g/kWh, 14.6 g/kWh, 14.6 g/kWh, and 15.4 g/kWh for diesel, methane, ethane, and propane respectively. Due to differences in fuel LHV an increased total mass of NG fuel (41.5 g, 44.0 g, and 45.8 g for methane, ethane, and propane respectively) was required as carbon content increased. NO emissions were 0.78 g/kWh, 6.55 g/kWh, 4.36 g/kWh, 6.16 g/kWh for diesel, methane, ethane, and propane, respectively. No clear trend for the NG fuels was found. As expected, NO emissions for the diesel-only case were low due to significantly lower bulk temperature compared to dual-fuel RCCI cases. However, the gas addition increased NO emissions by almost an order of magnitude. It was surprising to see that methane RCCI had not only the highest NO emissions (6.6 g/kWh), even if its bulk temperature was lower than that of propane RCCI. In addition, NO emissions were ~ 50% higher than those of ethane RCCI, despite a similar bulk temperature. As NO emissions did not follow the T_{ad} trend, it suggests some important combustion differences with respect to location and/or engulfed volume. This could be a result of prompt NO_x forming in the presence of early-stage combustion radicals [125].

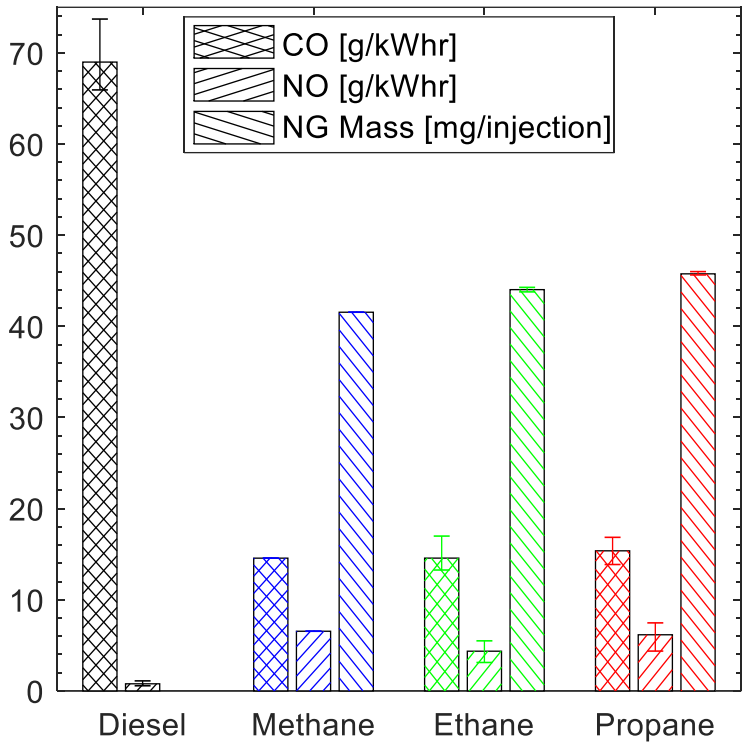

Figure 49- Effect of Gaseous C_1-C_3 Components on CO, NO, and the Respective Delivered NG Mass (Optical Engine, RCCI Mode, 63% Substitution Rate, 1000 RPM, $P_{inj,diesel}$ = 500 bar). Error Bars Represent Standard Deviation of the Measurement

Figure 50 shows CO_2 and NG emissions (methane, ethane, and propane for the given dual-fuel case). CO_2 emissions (910 g/kWh, 705 g/kWh, 862 g/kWh, and 897 g/kWh for diesel, methane, ethane, and propane, respectively), show a clear dependence on IMEP (i.e., indicated power used to normalize the emissions). This was made clear from the diesel case (lower total fuel mass). For the dual-fuel cases, however, it is unlikely that the small variation in IMEP could cause a drastic increase in CO_2 for ethane and propane compared to methane. CO_2 emissions increased with fuel carbon content as expected. It was assumed CO_2 emissions had a high margin of error associated with them due to the magnitude (~0.6%) compared to the FTIR measurement range (0-20%). Indicated NG emissions (over-inflated due to fuel slip) were 105 g/kWh, 90 g/kWh, and 126 g/kWh for methane, ethane, and propane, respectively. This did not show a clear trend with total NG fuel mass or IMEP differences, however increased NG MFB was directly related to lower NG emissions. The magnitude of NG emissions suggests that, irrespective of the RCCI case, only ~50% of the delivered gas participated in the combustion process. In addition, propane RCCI had

the largest NG emissions, which was unexpected when considered that propane is the most reactive of the three gases. Therefore, the results indicate that the non-optimized combustion chamber geometry of the optical engine may have played an important role in both mixture preparation as well as oxidation location and rate. Results also suggest the importance of tailoring the low-high fuel reactivity ratio of the dual-fuel combustion based on the operating condition as, for the diesel-only case, most of the fuel presumably partially oxidized to CO.

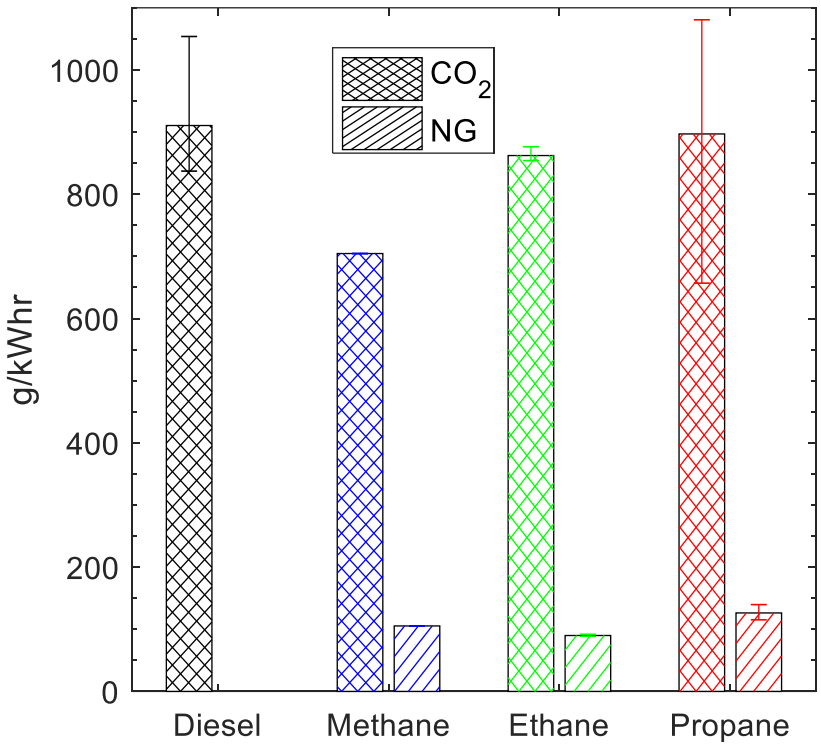

Figure 50- Effect of Gaseous C_1-C_3 Components on CO_2 and NG (Optical Engine, RCCI Mode, 63% Substitution Rate, 1000 RPM, $P_{inj,diesel}$ = 500 bar). Error Bars Represent Standard Deviation of the Measurement

Image analysis shed some light on the results presented above. As a reminder, the combustion event was imaged every 0.2 CAD, starting from the SOI_{DIESEL} of -40 CAD ATDC and beyond the end of combustion. The much earlier injection (at lower in-cylinder temperature and pressure) increased the time available for diesel vaporization. Therefore, due to the long duration between SOI_{DIESEL} and SOC, it was assumed that the diesel was completely vaporized at SOC. The following analysis and discussion will observe in-cylinder natural luminosity evolution, from the

diesel-only case to the three RCCI cases. The AHRR and SINL scales in the next figures were kept the same for all cases to help visualize the case-to-case evolution.

Image analysis starts with the diesel-only case. Figure 51 shows a set of NL images from an actual fired cycle (cycle 9 in this case), at several combustion phasing points of interest from close to SOC (CA30) to EOC (CA95). Each image in Figure 51 shows the frame number and the time when it was acquired with respect to SOI_{DIESEL}, and the frame crank angle location. It also shows the f-number used, in this case f/1.4. Similar to [126], images suggest that combustion started in the squish volume, followed by an inward propagation toward the center of the cylinder. Combustion occurred spatially and not necessarily around the known diesel jet locations, supporting the premixed combustion hypothesis. As indicated by the AHRR, a low temperature heat release (LTHR) occurred for ~ 5 CAD before the main high temperature combustion, peaking at -15 CAD ATDC. The main high temperature heat release (HTHR) started at ~ -14 CAD ATDC. LTHR did not produce any significant natural luminosity and thus was not "seen" by the camera. As a result, the set of images in Figure 51 starts with the frame corresponding to CA30 because this is when some significant combustion activity was detected also supported by the SINL increasing from zero. Images corresponding to CA50 and CA70 suggest that premixed combustion is now taking place almost everywhere inside the bowl (the "whitish" area in the images), also supported by the AHRR peak being between CA50 and CA70. However, SINL barely increased. High intensity "dots" (many consisting of saturated pixels) appeared in CA70 image. As mixing-control signal intensity is degrees of magnitude higher than premixed combustion signal intensity, it suggests that those "dots" were produced by the diffusive combustion of end-of-injection fuel dribble or from fuel that condensed on the bowl window surface and bowl corners due to low turbulence intensity (hence worse air-fuel mixing) in flat bowls with straight walls [127]. CA90 and CA95 images show a large drop in the premixed combustion, which correlated with the drop in the AHRR. SINL was still low, but there was more evidence of isolated droplet-based combustion, now also visible in the bottom left corner of the bowl. The soot radiation increased after CA95 and SINL remained at a maximum for ~15 CAD, but only a small fraction of the heat release occurred, primarily from the droplet diffusion-based combustion. This suggests that the fraction of the diesel that participated in this droplet burning was small. Afterward, the SINL gradually decreases as the cycle progresses further into the expansion stroke where decreasing bulk gas temperature drops the soot temperature and proportionally soot radiation.

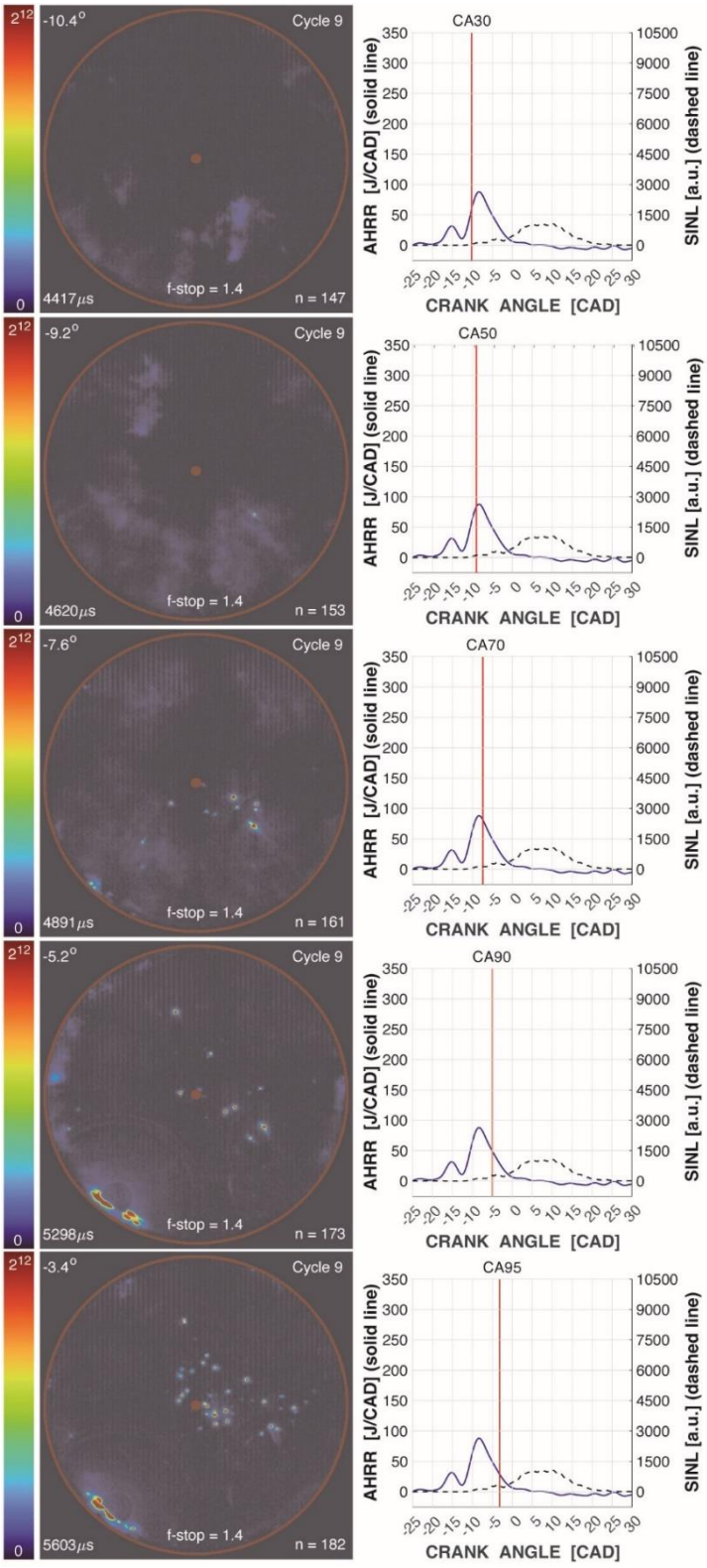

Figure 51- Image Data: In-Cylinder Natural Luminosity for the Diesel-only Case, at Several Combustion Phasing of Interest (SOI_{DIESEL} = -40 CAD ATDC, 63% ESR, 1000 RPM, 3 bar IMEP). The Corresponding Timing on the AHRR and SINL Traces is Also Shown for Clarity.

The gas addition (RCCI cases) produced significant differences in NL images and SINL, as shown in Figure 52 for the methane RCCI case. First, the increase in the total fuel energy (see the two-times-higher AHRR peak) increased the NL signal. For example, peak SINL is around an order of magnitude higher than the diesel-only case. LTHR was relatively similar in terms of magnitude and duration but delayed by several degrees, and, again, was not "seen" by the camera. HTHR started at ~ -12 CAD ATDC and the short combustion duration suggests that premixed combustion was dominant. The first instance of premixed combustion for the methane RCCI case is now seen in the CA10 image (-9.2 CA ATDC), with SINL increasing from zero around the same time. CA50 image (-6 CA ATDC) is now after the AHRR peak and shows that premixed combustion is taking place everywhere inside the bowl. Compared to the diesel-only case, the corresponding SINL was at ~ 10% of its maximum (close to the peak value from diesel-only case), but the CA50 image show that the SINL increase was due to the same droplet-based combustion mentioned before, appearing earlier because the pressure and temperature were higher (Note that ~ 10% of maximum SINL for the methane RCCI case is close to the maximum SINL for the diesel-only case). CA70 image (-4.4 CA ATDC) still shows premixed combustion but with a less intensity, in line with the inflexion point on AHRR, associated, for a similar chamber geometry, with the reduction in burning rate in the squish area due to the higher surface-to-volume ratio as the piston approaches TDC [128] and the end of the premixed burn inside the bowl. This is supported by the CA90 and CA95 images (0.4 CA and 3.4 CA ATDC, respectively), where almost all the NL comes from the diffusive combustion of end-of-injection fuel dribble (see the "dots" in the center of the image) or from fuel that condensed on the bowl window surface (the high signal areas near the edge of the bowl match the direction of the diesel fuel jets shown in Figure 7) and correlates with the lower AHHR at that time. The low heat release rate seen after CA95 for ~ 20 CAD without a clear premixed combustion NL was due to the premixed fuel trapped in the piston crevices coming out to in the main chamber, mixing with the hot combustion products, and partially oxidizing. Again, the higher in-cylinder temperature and pressure increased the soot radiation, hence the much higher SINL from the droplet-based combustion, and, because maximum T_{bulk} was around TDC (see Figure 42), the SINL is near its maximum. SINL then gradually decreases for ~25 CAD into the expansion stroke as bulk gas temperature decreases.

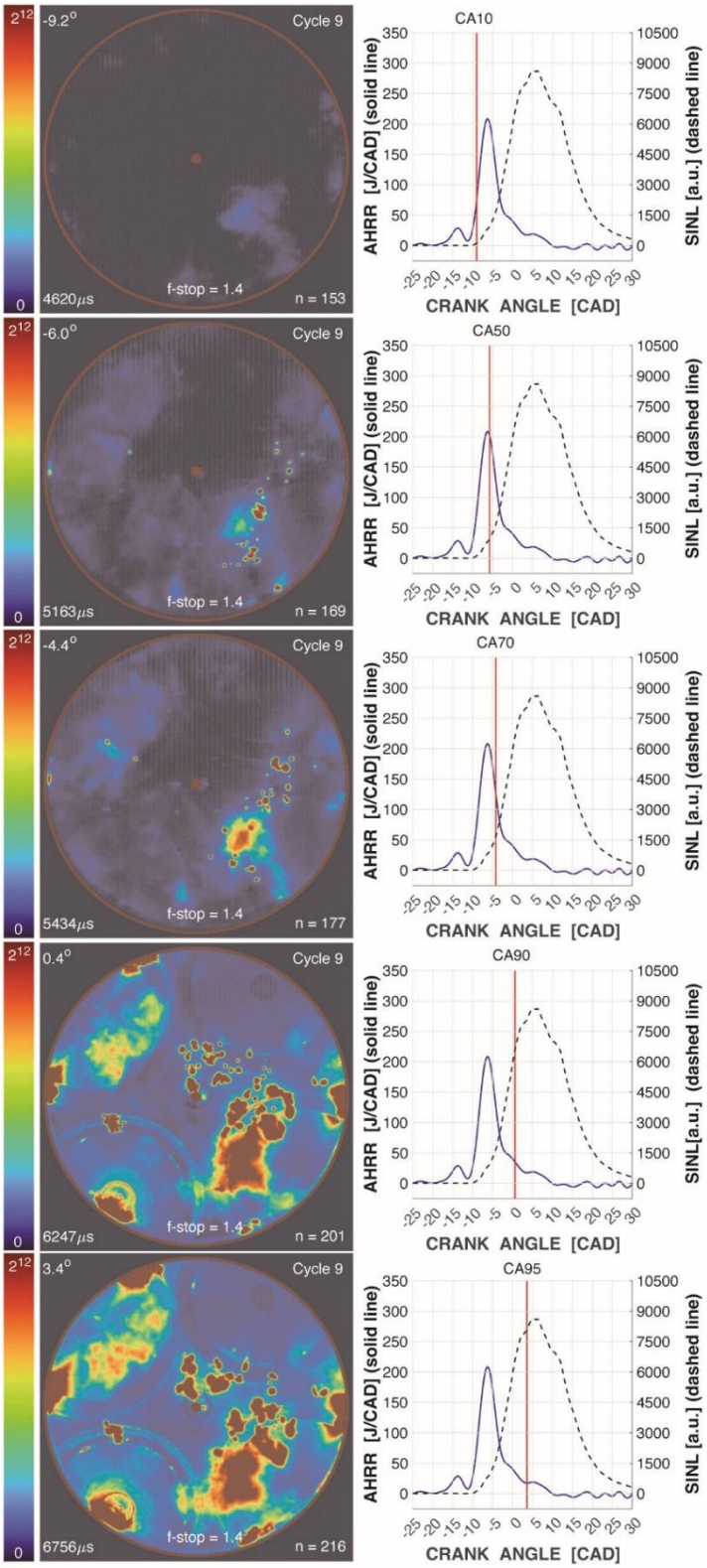

Figure 52- Image Data: In-Cylinder Natural Luminosity for the C_1 RCCI Case, at Several Combustion Phasing of Interest (SOI_{DIESEL} = -40 CAD ATDC, 63% ESR, 1000 RPM, 6.7 bar IMEP). The Corresponding Timing on the AHRR and SINL Traces is Also Shown for Clarity

Figure 53 shows ethane RCCI images. In general, the details presented in each image for a particular combustion phasing are similar to what was seen for methane RCCI. However, there are a few differences. First, the images for ethane RCCI are delayed by ~ 1 CAD for CA10, CA50, and CA70, compared to methane RCCI, with the delay becoming negligible as combustion was near its end. However, the corresponding location of each image on the AHRR or SINL trace was similar. Then, the SINL for ethane RCCI in this cycle was slightly lower, suggesting a gas effect on soot particle excitation. This was surprising when considering the similar AHHR and T_{bulk} in Figure 42 and that it was not expected the gas would have any significant effect on the diesel injection dribble and fraction of diesel that condensed inside the bowl. Subsequently, the SINL for all imaged cycles was averaged and plotted in Figure 54. And now C_1 RCCI and C_2 RCCI have a similar SINL magnitude, albeit a slight delay as NL images suggested. Therefore, it is expected that an increase in C_2 fraction in NG will not significantly affect soot formation if AHRR and T_{bulk} are not affected.

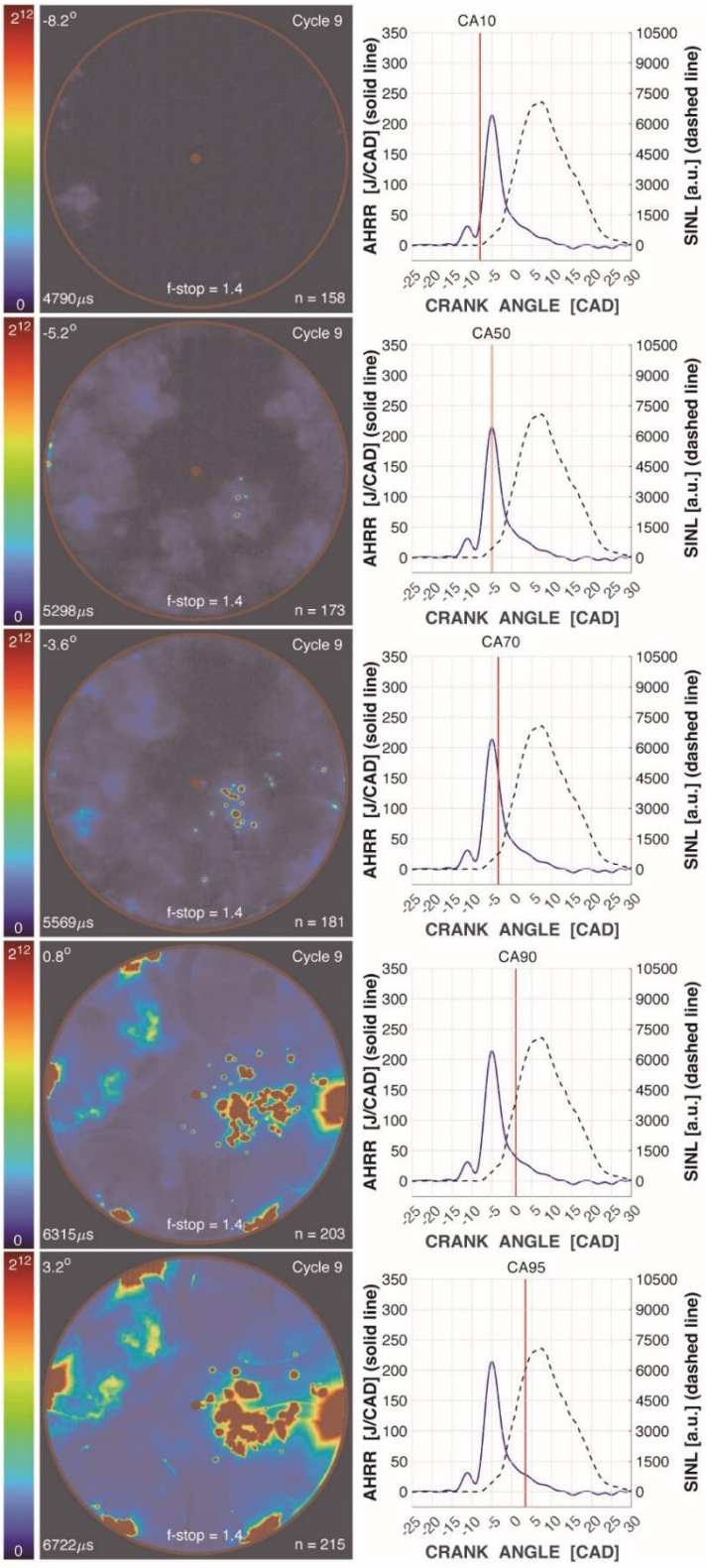

Figure 53- Image Data: In-Cylinder Natural Luminosity for the C_2 RCCI Case, at Several Combustion Phasing of Interest (SOI_{DIESEL} = -40 CAD ATDC, 63% ESR, 1000 RPM, 6.6 bar IMEP). The Corresponding Timing on the AHRR and SINL Traces is Also Shown for Clarity.

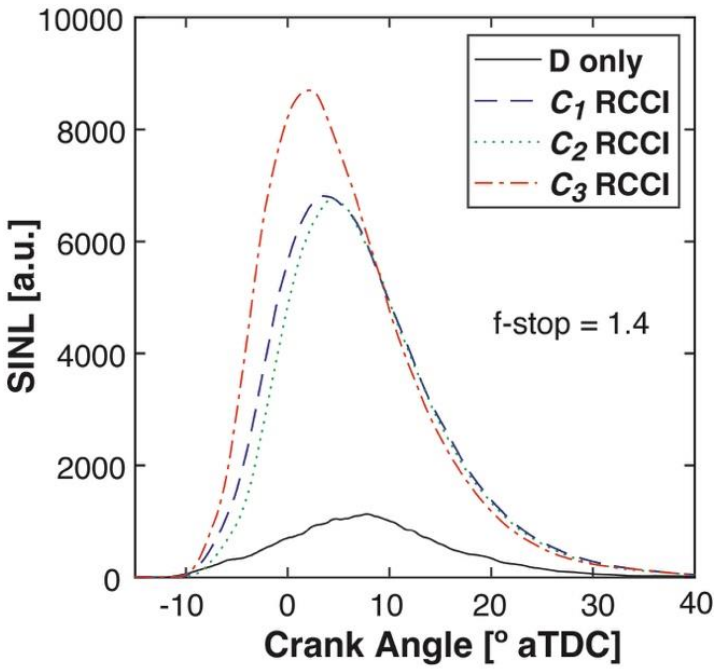

Figure 54- Effect of NL Component on SINL Signal (SOI_{DIESEL} = -40 CAD ATDC, 63% ESR, 1000 RPM).

Figure 55, which shows the C_3 RCCI images, suggests that despite an increased delay in the LTHR, the better oxidation properties of C_3 compared to both C_2 and C_1 affected the RCCI combustion at these low-load conditions and 63% ESR. The first instance of premixed combustion for the C_3 RCCI case is now seen in the CA20 image, but, as C_3 advanced the HTHR by ~ 1 CAD, was taken at same crank angle as the CA10 image for C_2 RCCI (- 8.2 CA ATDC). All this was despite the more than ~ 100 K T_{bulk} and more than double AHRR. This suggests that C_3 RCCI has a more intense burning in the non-visible squish area of the cylinder before propagating inward towards the center of the chamber. Then, the premixed combustion in the CA50 image, which, similar to those for C_1 RCCI and C_2 RCCI, corresponded to peak AHRR, occupied a smaller bowl volume. This suggests that the better oxidation properties of the C_3 decreased the time available for the diesel fuel to properly mixed with the gas mixture before the start of the main combustion, hence a larger fraction of the diesel fuel burning inside the squish area (where most of the diesel resided at such advanced SOI_{DIESEL}) compared to the other cases. Therefore, CA70 image for C_3 RCCI is similar to the CA50 image for C_1 RCCI and C_2 RCCI, and the premixed combustion was finally engulfing the bowl volume in the CA90 image compared to CA70 in the other RCCI cases. The corresponding crank angle for the CA50, CA70, and CA90 images for the for C_3 RCCI is 1 CA to

3 CA more advanced than for the other two RCCI cases. Therefore, the lower NL inside the bowl may be just the result of a slower flame propagation from the squish area towards the center of the bowl, if indeed there was less diesel fuel in the center of the bowl (i.e., lower global ϕ) compared to the squish volume where the combustion started (i.e., higher global ϕ). The faster and more intense combustion up to CA70 also supports a more stratified diesel-gas mixture, with a richer mixture inside the squish volume. Finally, the CA90 image was taken at the same inflexion point on the rapidly decreasing AHRR, so the amount of fuel that burned after the premixed combustion completely engulfed the bowl (as seen in the CA90 and CA95 images) was relatively low compared to fraction of the fuel that burned before it. Similar to the other cases, the diesel injection dribble and the fraction of diesel that condensed inside the bowl started combusting in late-phasing images, in the same locations as in the other diesel-only or RCCI cases, albeit with a lower intensity as the images were taken earlier, as mentioned before. Then, as expected, Figure 54 shows that, overall, the maximum SINL in was the highest for the C_3 RCCI, considering that a higher T_{bulk} (see Figure 42) will increase the radiation of the burning diesel droplets). An interesting final observation is that while the SINL magnitude was different between the investigated cases, the time it took for the SINL to decrease from its maximum to its minimum was similar for all four cases, suggesting that the gas addition did not change the fraction of the diesel fuel that participated in the diffusion-controlled combustion.

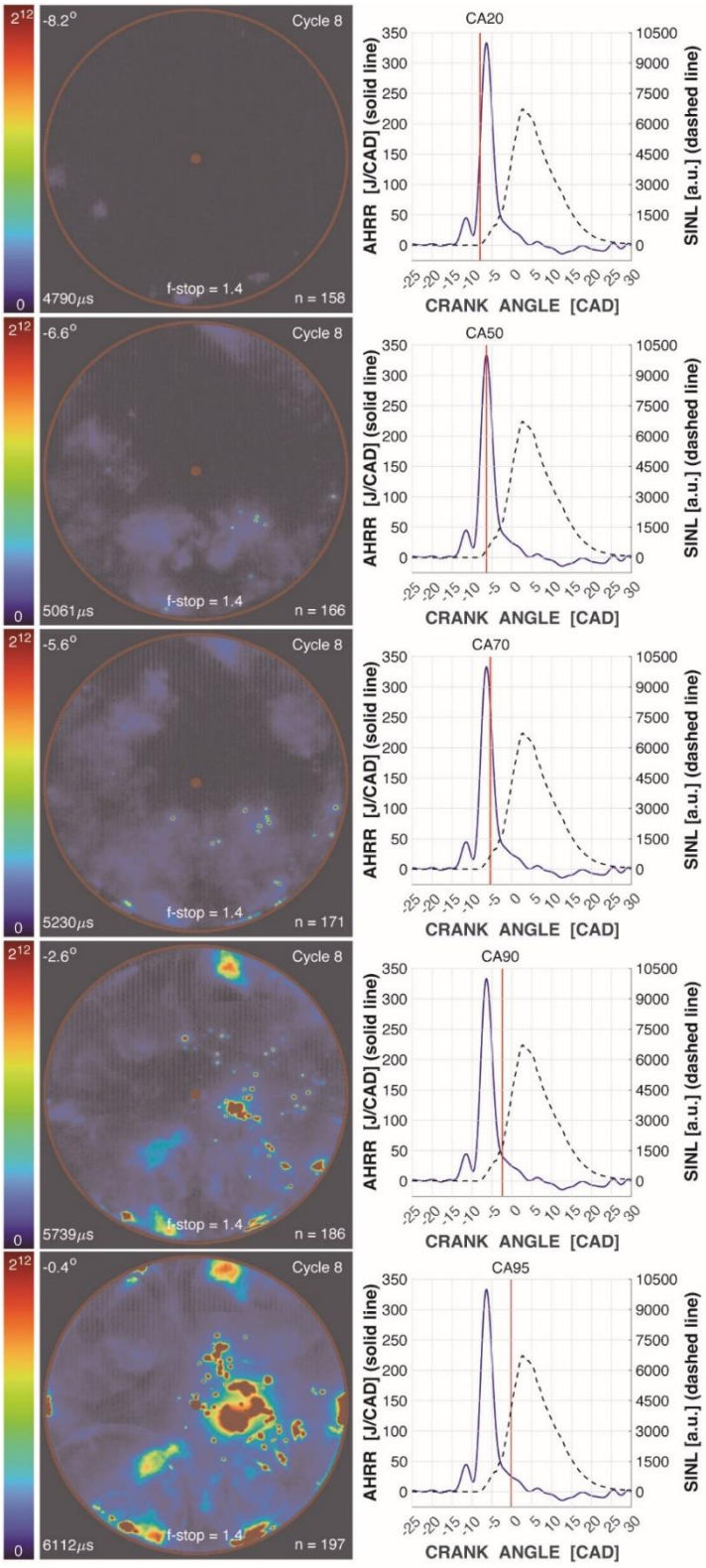

Figure 55- Image Data: In-cylinder Natural Luminosity for the C_3 RCCI Case, at Several Combustion Phasing of Interest (SOI_{DIESEL} = -40 CAD ATDC, 63% ESR, 1000 RPM, 6.5 bar IMEP). The Corresponding Timing on the AHRR and SINL Traces is Also Shown for Clarity.

4.4.2: Effect of Natural Gas Composition in Optical Engine Experiments in MCCI mode (SOI_{DIESEL} = -8 CAD ATDC)

Figure 56 shows the effect of major NG components on the averaged in-cylinder pressure traces, under MCCI conditions (SOI_{DIESEL} = -8 CAD ATDC). The peak pressure was marginally higher for ethane but with more delay and variability in location compared to propane and methane. Also, the pressure rise occurs earlier for methane than ethane and propane, which was unexpected based on the previous results. This may be due to the slightly higher pressure observed during compression at the time of SOI_{DIESEL}. As compared to the diesel case, propane was 0.6 bar lower pressure, ethane 0.3 bar lower, and methane only 0.1 bar lower. In general, the dual-fuel cases had a ~1-2 CAD delay to the start of pressure rise compared to the diesel base. For diesel, methane, ethane, and propane the net work was 414 J/cycle, 749 J/cycle, 727 J/cycle, and 744 J/cycle, respectively. This was a substantial increase for the diesel base (23%), slight decrease for methane (1%) and ethane (1.5%), and slight increase for propane (1%) compared to RCCI mode.

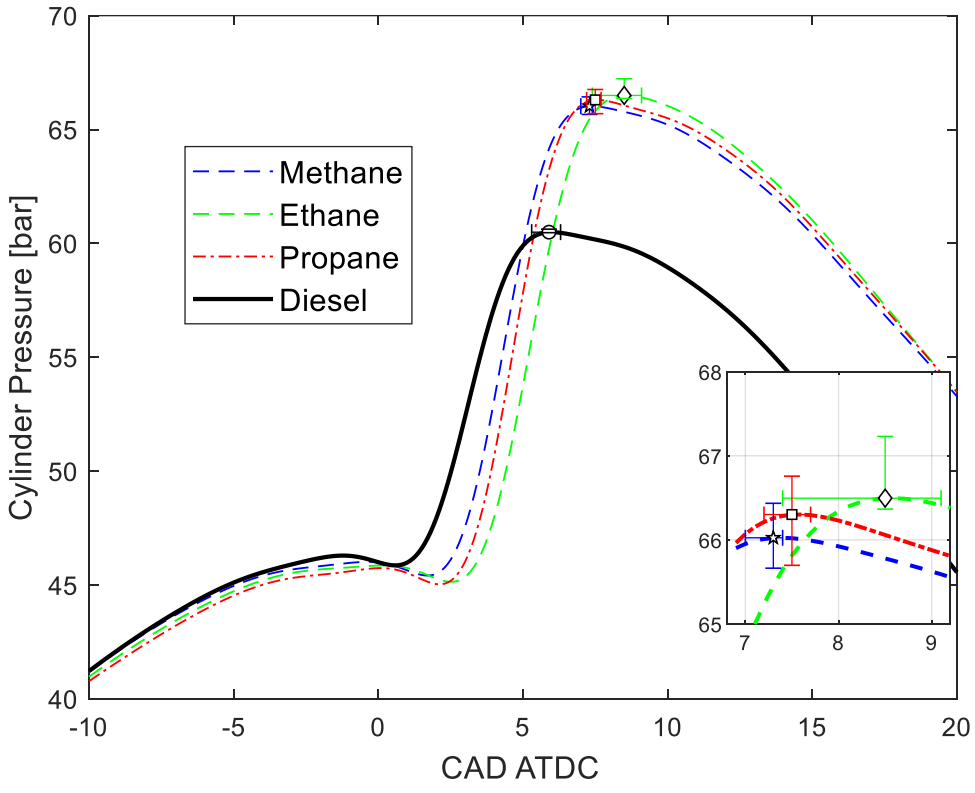

Figure 56- Effect of Gaseous C_1-C_3 Components on In-Cylinder Pressure (Optical Engine, MCCI Mode, 63% Substitution Rate, 1000 RPM, $P_{inj,diesel}$ = 500 bar). Error Bars Represent Standard Deviation of the Measurement

The AHRR shown in Figure 57 provides further detail on the combustion phasing differences. The dual-fuel cases LTHR all start roughly 2 CAD later than the diesel case, but all with significantly lower magnitude compared to RCCI mode. The HTHR starts more advanced for methane than propane or ethane, but propane exhibits a higher peak heat release rate. The peak heat release for diesel (200 J/CA) occurred at 3.2 CAD ATDC, followed by methane (276 J/CA) at 4.4, propane (293 J/CA) at 4.8, and ethane (277 J/CA) at 5.3. It should be mentioned that the AHRR magnitude was nearly identical for methane and ethane but ~1 CAD delayed for ethane. Furthermore, the end of HTHR also occurs in the same order as the start.

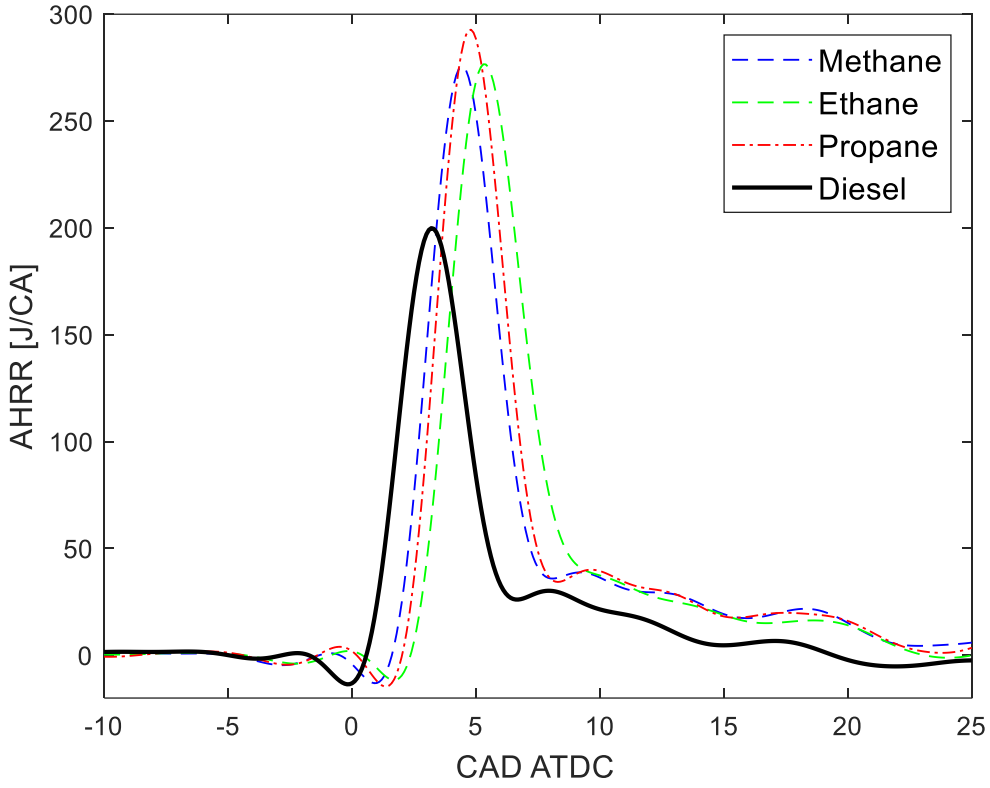

Figure 57- Effect of Gaseous C_1-C_3 Components on Apparent Heat Release Rate (Optical Engine, MCCI Mode, 63% Substitution Rate, 1000 RPM, $P_{inj,diesel}$ = 500 bar)

Figure 58 shows the cumulative heat release rate for diesel (800 J), methane (1351 J), ethane (1297 J), and propane (1331 J). It is also noted some of the heat release occurs after the angle displayed in the figure. This suggests methane exhibited more of a slow burn later into the expansion stroke compared to ethane and propane, while the diesel only case combustion was nearly complete at by 25 CAD ATDC.

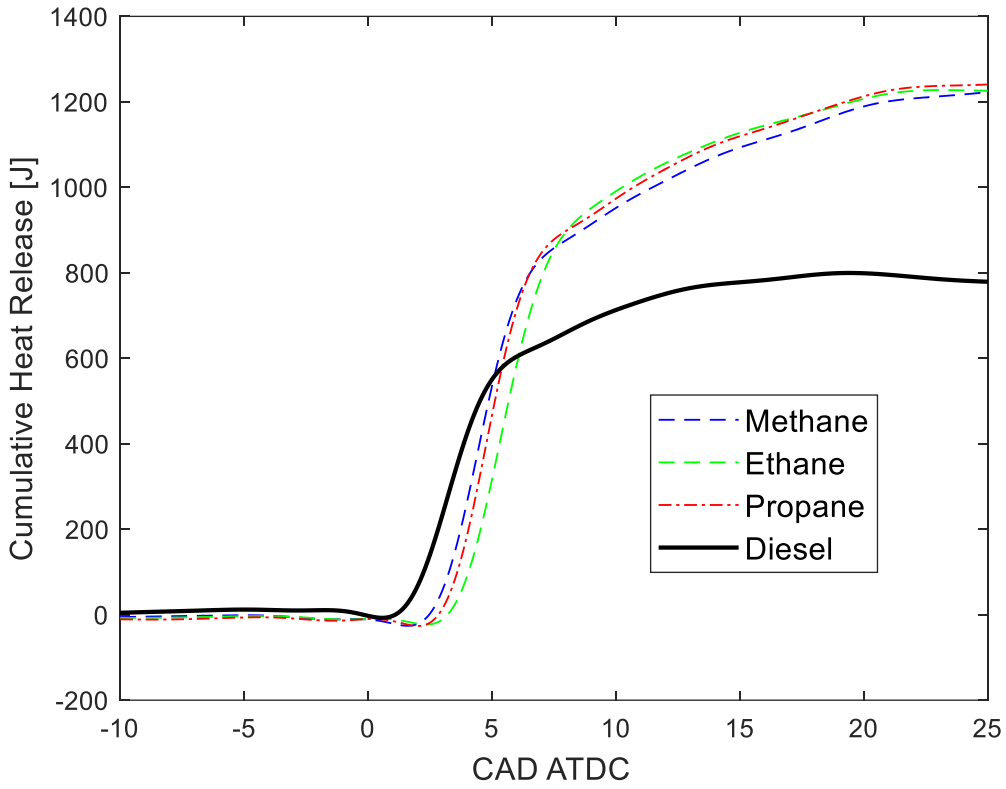

Figure 58- Effect of Gaseous C_1-C_3 Components on Cumulative Heat Release (Optical Engine, MCCI Mode, 63% Substitution Rate, 1000 RPM, $P_{inj,diesel}$ = 500 bar)

The bulk gas temperature shown in Figure 59 indicates once again the propane case had the highest peak temperature (1370 K). The peak temperatures for ethane (1348 K) and methane (1332 K) differed from the trend in RCCI mode and did not correspond to higher adiabatic flame temperature of the respective fuels. All peak temperatures were substantially lower than those observed in RCCI mode, which would be expected to have an impact on thermal NO formation.

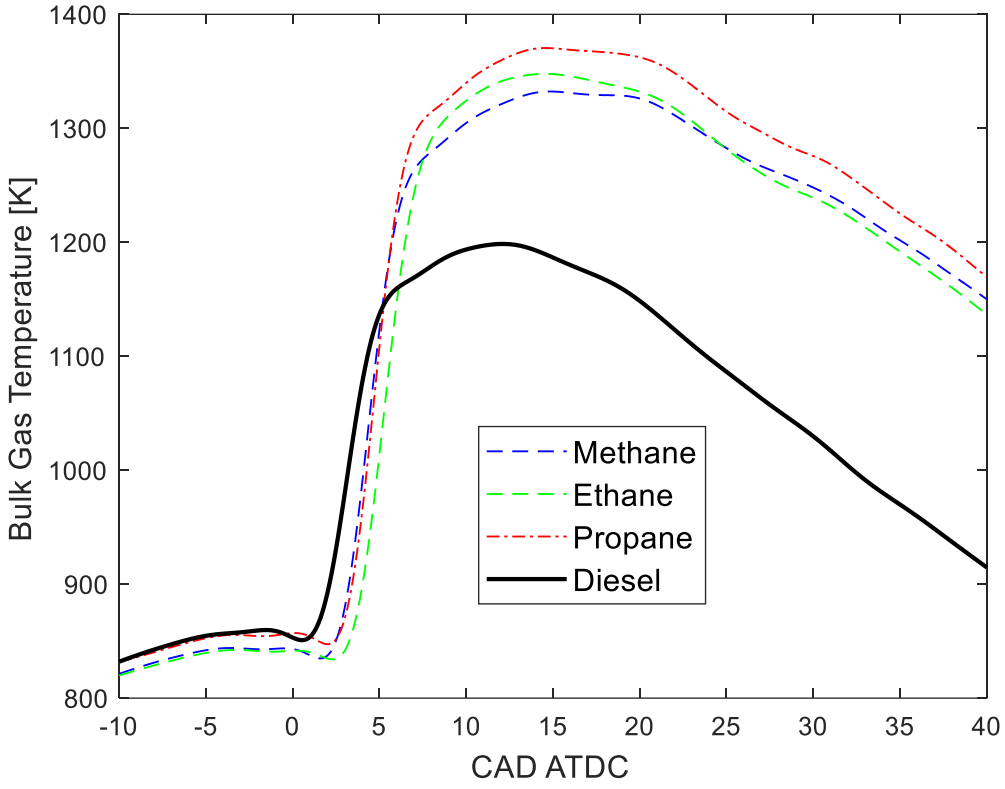

Figure 59- Effect of Gaseous C_1-C_3 Components on Bulk Gas Temperature (Optical Engine, MCCI Mode, 63% Substitution Rate, 1000 RPM, $P_{inj,diesel}$ = 500 bar)

Figure 60 shows the IMEP, COV of IMEP, and rate of pressure rise. IMEP was 3.7, 6.7, 6.5, and 6.6 bar for diesel, methane, ethane, and propane, respectively. This shows IMEP for dual-fuel conditions was similar to RCCI mode, while IMEP for diesel was higher indicating a better in-cylinder condition for the diesel combustion. The COV of IMEP was relatively stable (slightly above 3%) with 3.2%, 3.5%, 3.6%, and 3.6% for diesel, methane, ethane, and propane respectively. This indicated less combustion stability for the dual-fuel cases compared to RCCI, but higher stability for the diesel only base quantity of fuel. The dP/dθ 5.7 bar/CAD, 7.6 bar/CAD, 8.3 bar/CAD, and 8.1 bar/CAD for diesel, methane, ethane, and propane, respectively. These data show a faster pressure rise for diesel, methane, and ethane compared to RCCI mode but lower for propane. This suggests propane had a lower degree of premixed gas and diesel autoignition based on later combustion phasing compared to RCCI, while the highest dual-fuel pressure rise rate for ethane also corresponded to shortest combustion duration (as did propane RCCI).

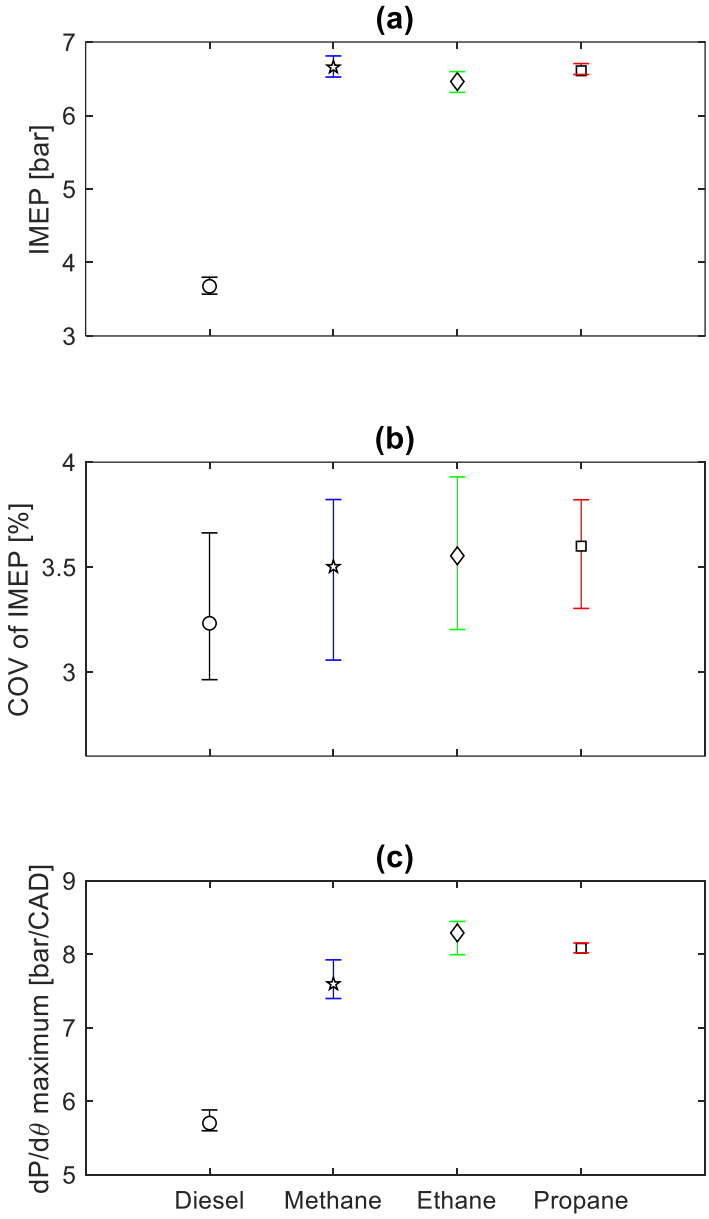

Figure 60- Effect of Gaseous C_1-C_3 Components on (a) IMEP, (b) COV of IMEP, (c) Maximum Pressure Rise Rate (Optical Engine, MCCI Mode, 63% Substitution Rate, 1000 RPM, $P_{inj,diesel}$ = 500 bar). Error Bars Represent Standard Deviation of the Measurement

The combustion phasing differences are detailed in Figure 61. CA10 occurred shortly after TDC for all cases, with diesel occurring first at 2.2 CAD ATDC, methane at 3.5 CAD ATDC, ethane at 4.4 CAD ATDC, and propane at 3.8 CAD ATDC. CA50 followed the same trend as CA10, with 3.8 CAD ATDC, 5.6 CAD ATDC, 6.1 CAD ATDC, and 5.7 CAD ATDC for diesel, methane, ethane, and propane respectively. However, from CA90 data a clear change in combustion characteristic can be observed. The CA90 values for diesel, methane, ethane, and propane

(10.3 CAD ATDC, 23.2 CAD ATDC, 17.3 CAD ATDC, and 19.2 CAD ATDC, respectively) show methane indeed continued the combustion process further into the expansion stroke compared to the other fuels.

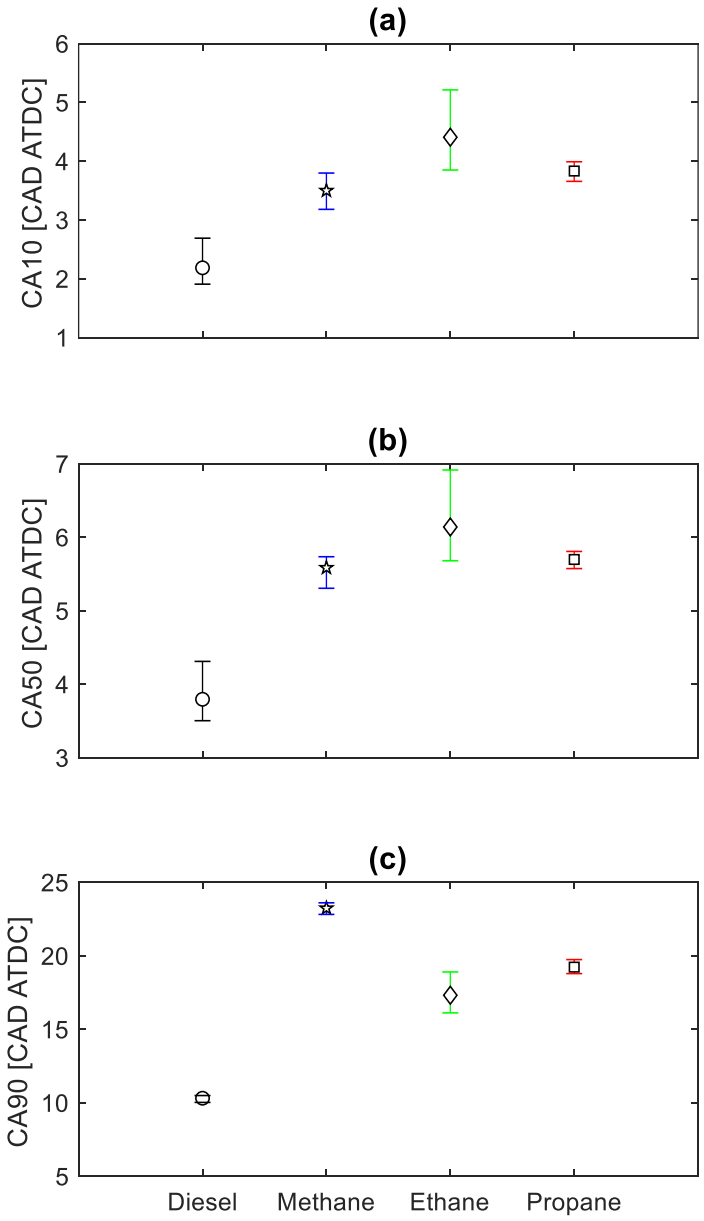

Figure 61 - Effect of Gaseous C_1-C_3 Components on (a) CA10, (b) CA50, (c) CA90 (Optical Engine, MCCI Mode, 63% Substitution Rate, 1000 RPM, $P_{inj,diesel}$ = 500 bar). Error Bars Represent Standard Deviation of the Measurement

Figure 62 displays the trapped air mass (again ~2.3-2.4 g/cycle), peak motoring pressure (~46.6 bar), and total heat release. The trapped mass and peak motoring pressure show consistency

between RCCI and MCCI experimental conditions. Methane and propane had a slightly higher total heat (30-50 J), which was also observed for RCCI combustion. This was a result of more late cycle heat release occurring for methane and propane, which is not clearly shown in Figure 58.

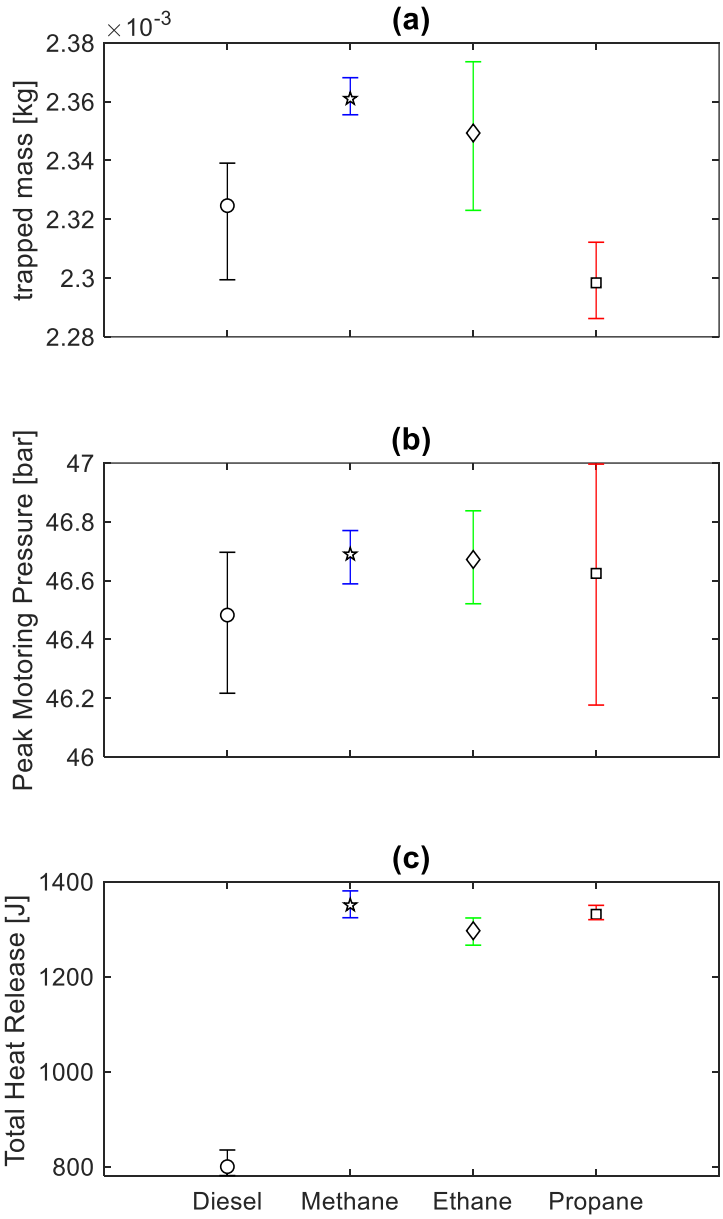

Figure 62- (a) Trapped Mass, (b) Peak Motoring Pressure, (c) Effect of Gaseous C_1-C_3 Components on Total Heat Release (Optical Engine, MCCI Mode, 63% Substitution Rate, 1000 RPM, $P_{inj,diesel}$ = 500 bar). Error Bars Represent Standard Deviation of the Measurement

Figure 63 shows less delay in ignition for MCCI compared to RCCI mode, as expected due to the more ideal in-cylinder conditions at SOI_{DIESEL}. This resulted in an ignition delay of 10.2 CAD, 11.5 CAD, 12.4 CAD, and 11.8 CAD for diesel, methane, ethane, and propane, respectively. Unlike the RCCI mode the ignition delay for methane was shorter than propane, but ethane was still the most delayed. The combustion duration, 8.1 CAD, 19.7 CAD, 12.9 CAD, and 15.4 CAD for diesel, methane, ethane, and propane respectively, shows the fastest dual-fuel combustion process under diffusion combustion mode shifts to ethane rather than propane in RCCI. This could be attributed to the slightly later combustion phasing of ethane coupled with lower bulk gas temperature leading to increased flame quenching. Knocking analysis was also conducted. Knocking intensity (not shown in the figure) was higher compared to RCCI (1.59 bar, 1.65 bar, 1.89 bar, 1.82 bar for diesel, methane, ethane, and propane, respectively), with ethane having the highest. Similarly, RI (1.22 MW/m^2, 2.09 MW/m^2, 2.48 MW/m^2, 2.39 MW/m^2 for diesel, methane, ethane, and propane, respectively) was generally higher compared to RCCI except for the propane case. This was primarily a result of higher pressure rise rate (except for propane) coupled with a lower maximum cylinder pressure, despite the lower gas temperatures. The fuel with the highest RI, ethane, also corresponded to the highest $dP/d\theta$ and knocking intensity as well as lowest IMEP and shortest combustion duration.

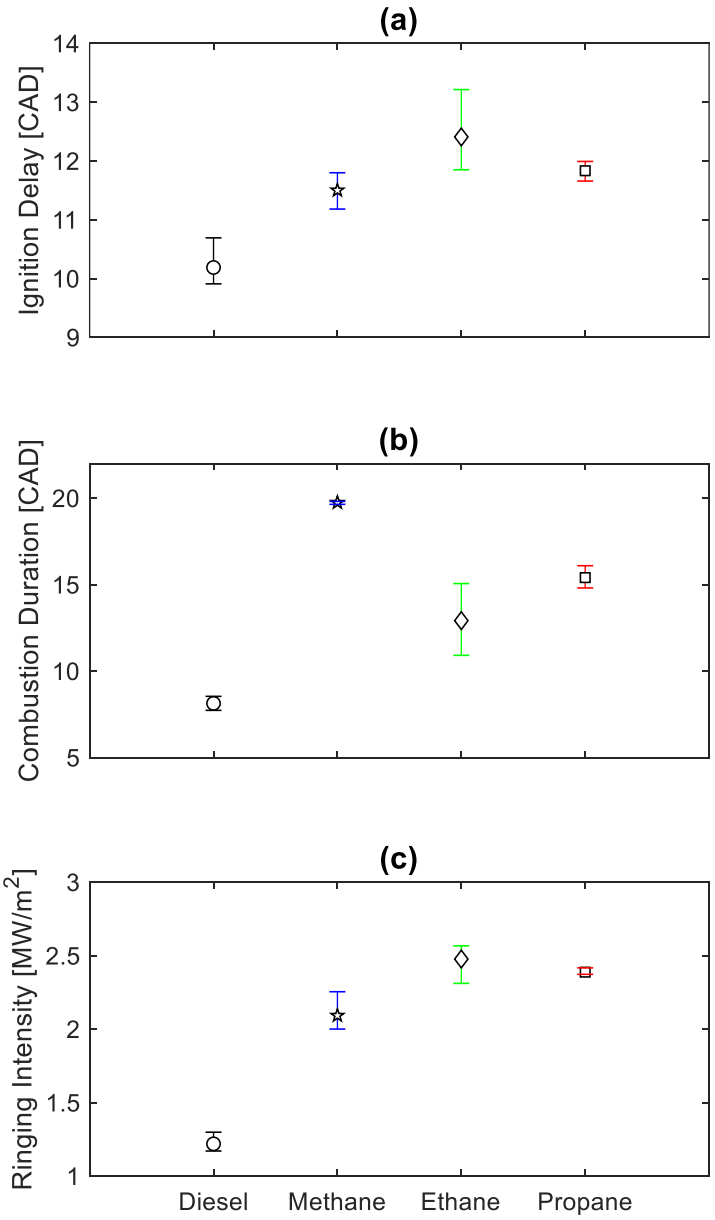

Figure 63- Effect of Gaseous C_1-C_3 Components on (a) Ignition Delay, (b) Combustion Duration, (c) Ringing Intensity (Optical Engine, MCCI Mode, 63% Substitution Rate, 1000 RPM, $P_{inj,diesel}$ = 500 bar). Error Bars Represent Standard Deviation of the Measurement

Figure 64 shows the sampled methane, ethane, and propane emission data for dual-fuel operation with SOI_{DIESEL} -8 CAD ATDC. The emission measurements for non-firing data were 8.1%, 236%, and 570% over-range for methane, ethane, and propane, respectively, while firing data were within range for methane but 67% and 278% over-range for ethane and propane. The non-firing background was 12 ppm lower for methane, 47 ppm lower for ethane, but 46 ppm higher for

propane compared to RCCI mode. Firing emissions data was 218 ppm, 85 ppm, and 34 ppm higher (12.9%, 11.4%, 4.7%) for methane, ethane, and propane, respectively, compared to RCCI mode. The same over-range sample correction (Equation 30) was applied to the results based on known error associated with excessive background emission values.

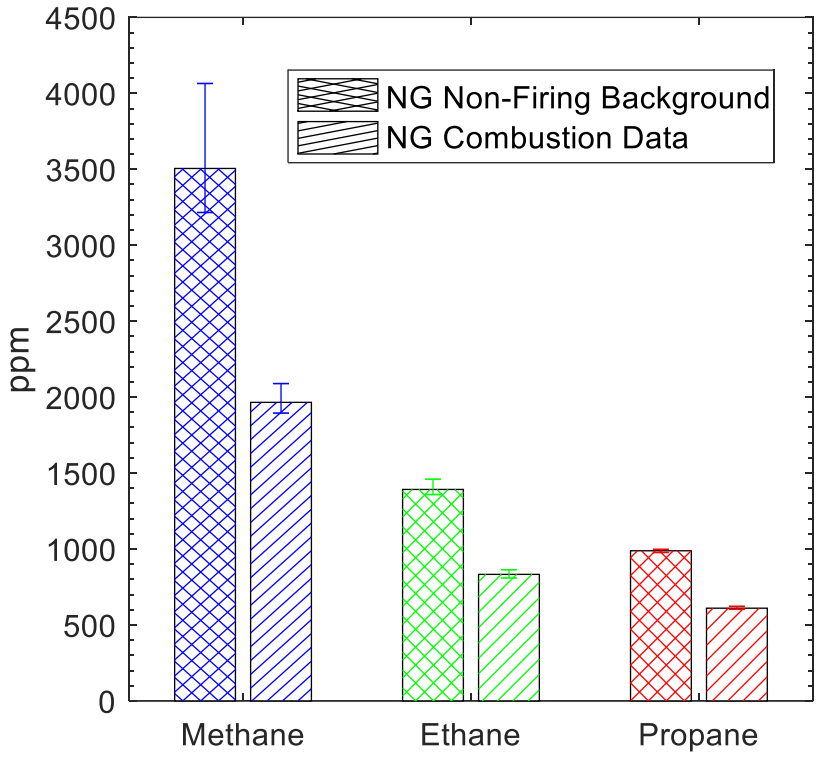

Figure 64- Effect of Gaseous C_1-C_3 Components on Gaseous Fuel Emissions for Firing and Non-Firing Data (Optical Engine, MCCI Mode, 63% Substitution Rate, 1000 RPM, $P_{inj,diesel}$ = 500 bar). Error Bars Represent Standard Deviation of the Measurement

Figure 65 shows the NG MFB had less change among fuels for later SOI_{DIESEL}, with 41.3%, 50.3%, and 43.4% reduction for methane, ethane, and propane, respectively. The NG MFB was lower for both methane and ethane, however almost identical for propane as compared to RCCI. The indicated efficiency shows diesel at levels expected for an optical engine configuration with a lower compression ratio than the original production engine. Indicated efficiency was 34.7%, 23.0%, 22.4%, and 22.5% for diesel, methane, ethane, and propane respectively. For the dual-fuel cases there was not much change in efficiency from RCCI mode (at most 0.3%), but the diesel efficiency improved by 6.5%. The modified energy substitution rate (41.7%, 46.4%, and 43.5% for methane, ethane, and propane) was 3-4% lower for methane and ethane compared to the RCCI

case, but the same for propane. This contrasts with the actual delivered energy substitution rate of 63%.

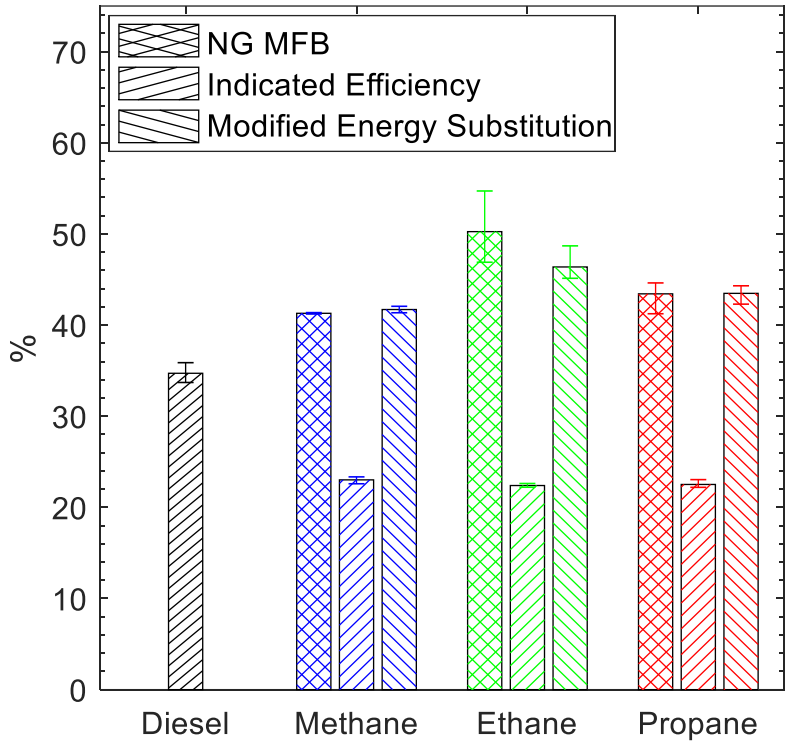

Figure 65- Effect of Gaseous C_1-C_3 Components on Natural Gas MFB, Indicated Efficiency, and Modified Energy Substitution Rate (Optical Engine, MCCI Mode, 63% Substitution Rate, 1000 RPM, $P_{inj,diesel}$ = 500 bar). Error Bars Represent Standard Deviation of the Measurement

Figure 66 shows CO and NO emissions follow an opposite pattern compared to RCCI, with the diesel base condition now having the highest NO and lowest CO. Specifically, CO emissions were 4.35 g/kWh, 26.8 g/kWh, 27.3 g/kWh, and 31.9 g/kWh and NO emissions 7.23, 5.02, 5.30, and 4.46 g/kWh for diesel, methane, ethane, and propane, respectively. CO emissions were nearly double that of RCCI operation for the dual-fuel cases, while NO emissions saw a 23% and 28% decrease for methane and propane but 22% increase for ethane. The higher CO emissions for propane was also coupled with a reduction in NO emissions. Also, for both the RCCI and MCCI modes, higher NO emissions under dual-fuel conditions were not directly related to higher in-cylinder bulk gas temperature as expected. This suggests that combustion phasing was the primary difference. The elevated NO emissions for the diesel base were also a result of lower indicated power by which specific emission values are normalized. The increasing mass of NG delivered

(41.4 mg/injection, 43.5 mg/injection, and 45.5 mg/injection for methane, ethane, and propane) may have partially contributed to the increasing CO_2 levels as shown in Figure 67.

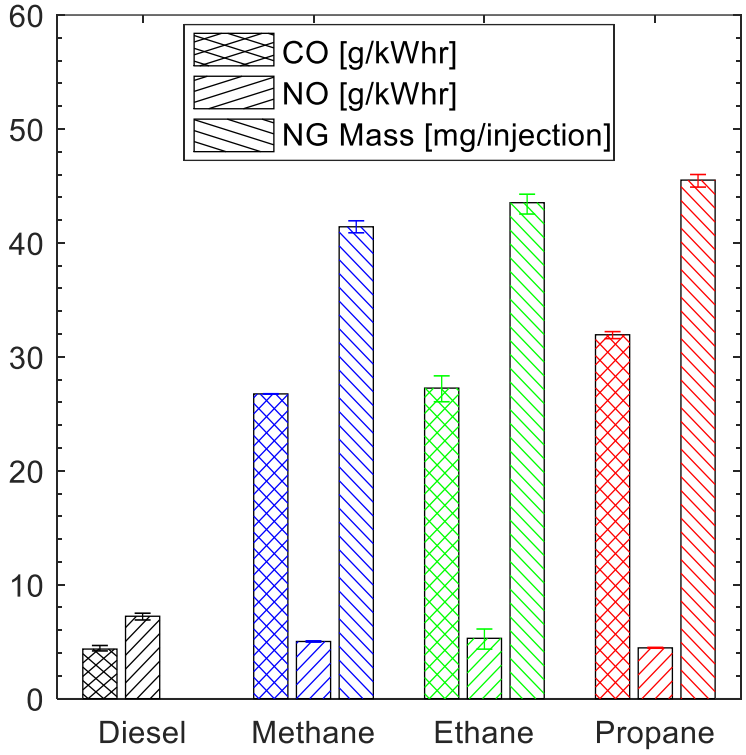

Figure 66- Effect of Gaseous C_1-C_3 Components on CO, NO, and the Respective Delivered NG Mass (Optical Engine, MCCI Mode, 63% Substitution Rate, 1000 RPM, $P_{inj,diesel}$ = 500 bar). Error Bars Represent Standard Deviation of the Measurement

Figure 67 shows the indicated specific CO_2 emissions were 686 g/kWh, 771 g/kWh, 898 g/kWh, and 973 g/kWh for diesel, methane, ethane, and propane, respectively. This equated to a 25% decrease for diesel-only case, and 9.4%, 4.2%, and 8.5% increase for methane, ethane, and propane respectively compared to RCCI mode. NO, CO, and CO_2 emissions show that the traditional SOI_{DIESEL} benefitted combustion of the diesel proportion of the dual-fuel mixture but adversely affected the gaseous portion. This can also be concluded from the NG fuel component emissions, 121 g/kWh, 102 g/kWh, and 129 g/kWh for methane, ethane, and propane, respectively; a 15%, 13%, and 2% increase from RCCI mode. However, the similarity in propane emissions along with slightly higher IMEP and efficiency suggests propane combustion may be better suited for the traditional SOI_{DIESEL} due to lower auto-ignition temperatures. Alternatively, the propane may require more delayed diesel injection timing under RCCI mode to improve combustion phasing.

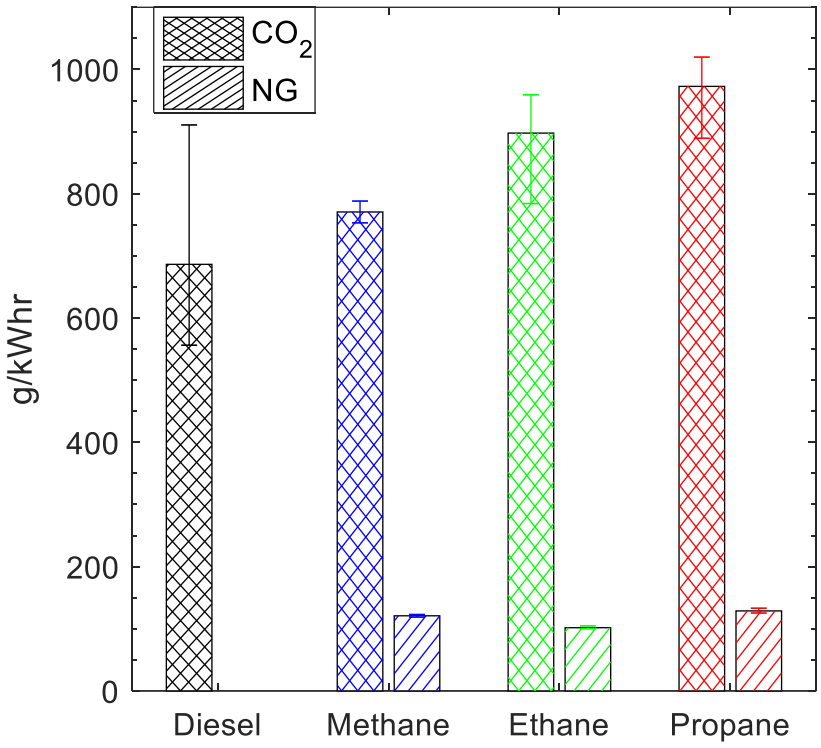

Figure 67- Effect of Gaseous C_1-C_3 Components on CO_2 and NG (Optical Engine, MCCI Mode, 63% Substitution Rate, 1000 RPM, $P_{inj,diesel}$ = 500 bar). Error Bars Represent Standard Deviation of the Measurement

Image analysis for the diesel base combustion in MCCI mode is presented in Figure 68. The injection duration was short (1.2 ms) for the diesel base combustion, as this was the same injection duration when NG was added. The start and end of fuel injection electronic command was -8.5 CAD ATDC and -1.3 CAD ATDC, respectively. AHRR data suggest that the electronical and mechanical injection system components delayed the actual start and end of in-cylinder fuel injection to ~ -3 CAD ATDC and ~ 4.5 CAD ATDC, respectively. In addition, AHRR data suggests that the ignition delay was ~ 2 CAD. For the injection pressure and duration used in this study, NL images suggest there were some differences between nozzles with respect to the mass flow rate through each one of them and different end of injection phenomena with respect to end-of-injection fuel penetration and fuel dribble after injection ended. The lean mixtures which appear near the injector after the end of injection, “dribbles”, are a contributor to the diesel related unburnt hydrocarbon emissions [129]. Combustion analysis indicated the CA5 to CA50 duration was ~ 2.7

CAD, the CA50 to CA90 duration was ~ 5.9 CAD, and CA50 to CA95 duration was ~ 8.5 CAD. Combustion specifics from both image and pressure data analysis are presented next.

Images show all six fuel jets albeit the jet at '7 o'clock' produced less soot; therefore, it was less visible than the other jets, in this specific cycle. This was a result of normal cycle-to-cycle variation. The first significant combustion luminosity is seen at CA30, when soot formation was large enough to start radiating inside the bowl. In this cycle, CA30 was slightly advanced from the crank angle associated to peak AHRR. Therefore, it suggests that a significant premixed burn inside the piston bowl happening at the same time but camera settings (i.e., a larger f-stop was used to avoid image saturation when soot radiation was significant) made it "invisible" in this case. CA50 image was taken just 0.8 CAD after CA30. SINL intensity in the CA50 image is ~ 50% of the maximum SINL in this cycle, suggesting that combustion started transitioning from the premixed to the mixing-controlled phase. In-cylinder fuel injection ended just 0.2 CAD later, slightly before CA60. The maximum SINL occurs just after CA70 at ~6.3 CAD ATDC. It then takes 5 CA from CA70 to CA90 and 7 CA from CA70 to CA95 to complete the combustion process, with AHRR suggesting it was a predominantly mixing-controlled process. SINL at CA95 is still at 70% of the SINL maximum. The intense soot radiation inside the piston bowl captured in CA95 image suggests that the soot mass was significant. However, the soot radiation was visible for additional ~ 10 CA after CA95 but with no significant energy released. This also suggests that the soot seen in the image is mostly the soot at the (flat) bottom of the bowl, which, due to the reduced flow turbulence near the 90-degree corners [127] experienced reduced oxidation after CA95, hence the low heat release. As a result, the decrease in SINL after CA95 was due to the decrease in bulk temperature during the expansion stroke, therefore a lower soot temperature and continuously decreasing SINL, rather than a reduction in soot fraction. Therefore, the images aligned with the phenomena seen in conventional diesel combustion.

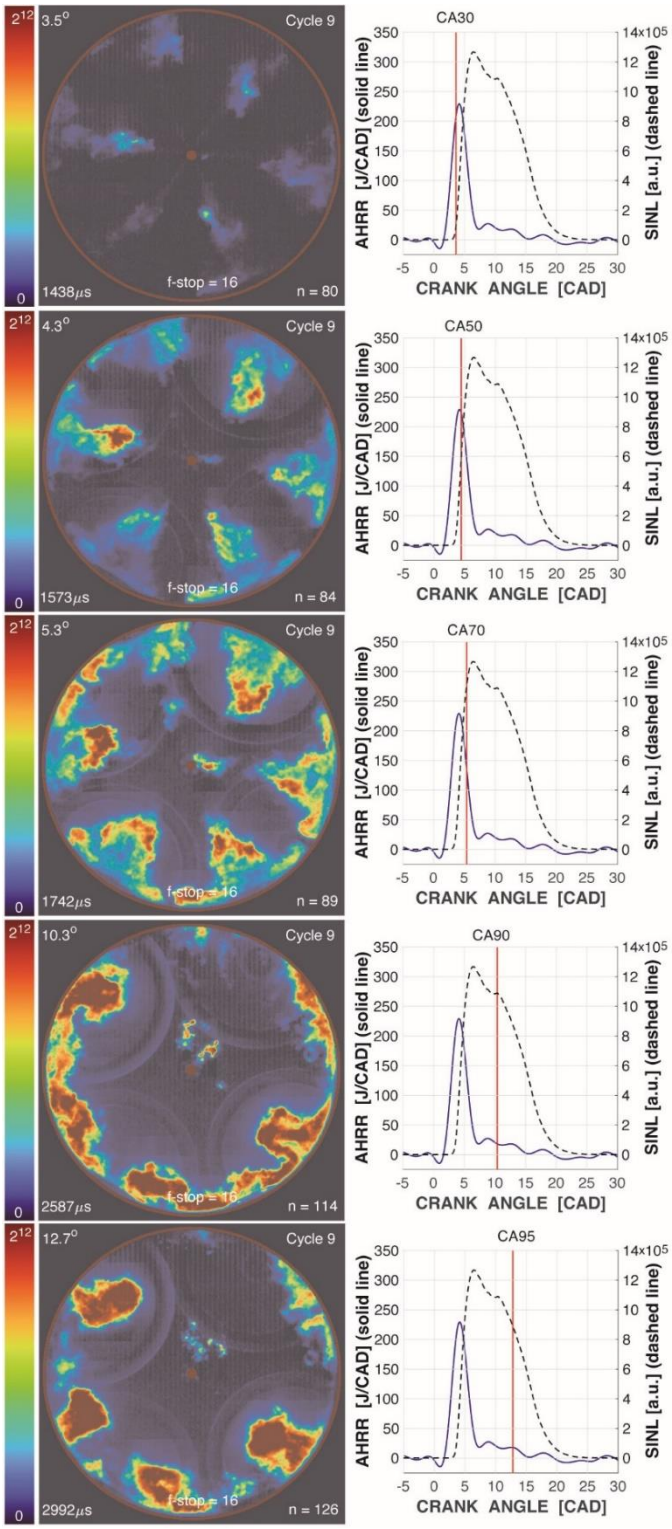

Figure 68- Image Data: In-Cylinder Natural Luminosity for the Diesel-only MCCI Case, at Several Combustion Phasing of Interest (SOI_{DIESEL} = -8 CAD ATDC, 63% ESR, 1000 RPM, 3.7 bar IMEP). The Corresponding Timing on the AHRR and SINL Traces is Also Shown for Clarity.

Image analysis of diesel-methane dual-fuel combustion in MCCI mode is presented in Figure 69. The same diesel injection duration was maintained (1.2 ms or 1190 J) with the addition of 2100 J/cycle methane delivered. As previously discussed, a moderate portion of the methane inevitably slipped directly into the exhaust due to excessive intake boosting coupled with using a port fuel injection strategy. The addition of methane delayed the mean CA5 by ~1.2 CAD compared to the diesel base for the cycle shown. The AHRR data suggests that the ignition delay was increased to ~ 2.6 CAD and that the same mechanical start of injection was maintained, however the end of injection was not visible due to lower soot reflective luminosity. Combustion analysis indicated the CA5 to CA50 duration was ~ 2.5 CAD, the CA50 to CA90 duration was ~ 17.5 CAD, and CA50 to CA95 duration was ~ 25.9 CAD. It is also noted CA95 was too delayed (~31.3 CAD ATDC) which resulted in a low intensity signal so only 4 representative images are shown. Combustion specifics from both image and pressure data analysis are presented next.

The added ignition delay from methane resulted loss of fuel jet visibility near the injector at CA20 due to a less luminous early premixed heat release for this cycle. CA20 still coincided with the earliest noticeable luminosity, around the '11 o'clock' jet, and occurred slightly before the peak of the AHRR. This suggests the early combustion was dominated by premixed burn even more so than diesel only case, especially considering a lower f-stop value. The diesel injection should have ended slightly before CA40 considering the same injection command was used for the dual-fuel case as the diesel base condition. The CA50 image occurred 1.6 CAD after CA20 and shows significant progression into simultaneous mixing-controlled and premixed combustion. This corresponded to ~50% of the maximum SINL value. The maximum SINL value occurs at ~6.7 CAD ATDC which also aligned with CA60. It then takes 13.1 CA from CA70 to CA90 and 21.6 CA from CA70 to CA95 to complete the combustion process, with AHRR and imaging suggesting it was a combined premixed and mixing-controlled process. SINL at CA90 was close to zero. The low soot radiation inside the piston bowl captured in CA90 image suggests that the soot mass was too low in temperature to be visible even though a small amount of heat was still being released. Late-stage combustion (CA70) fuel dribbles near the injector became sootier compared to the diesel base condition due to increased ignition delay with methane addition.

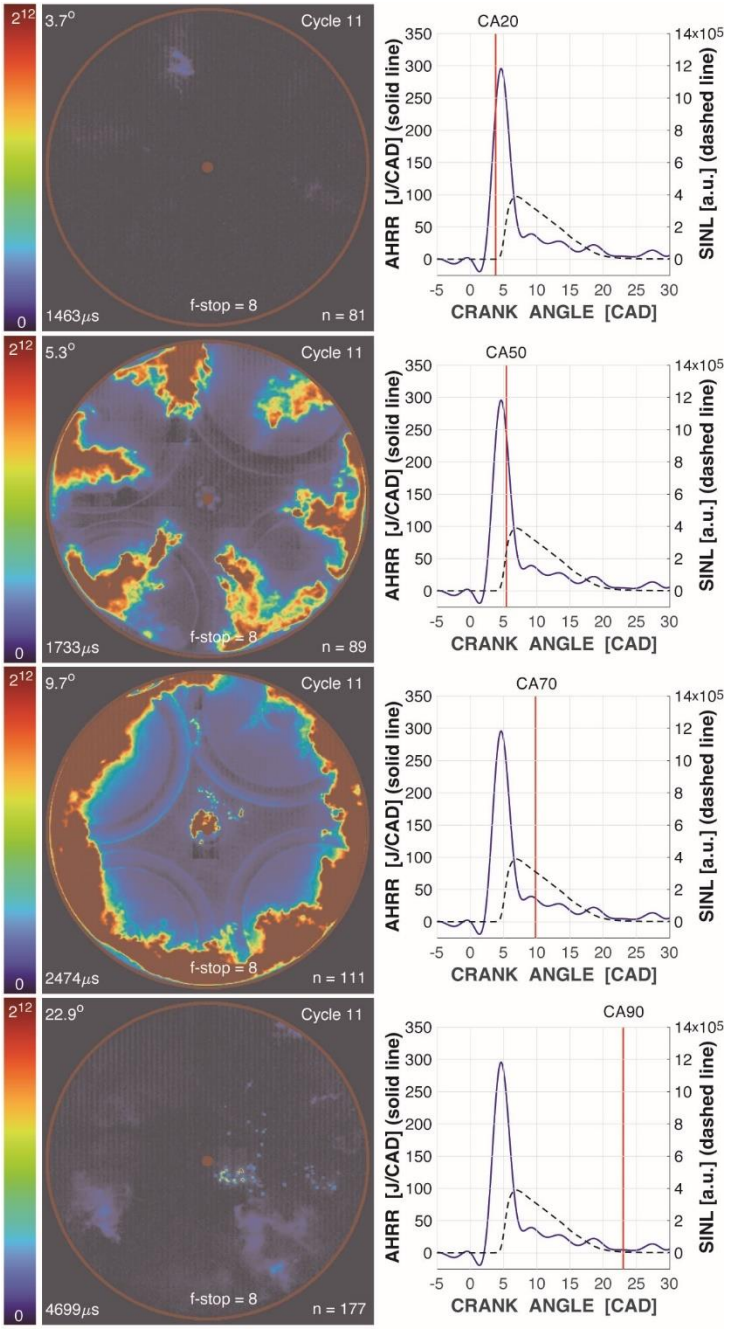

Figure 69- Image Data: In-Cylinder Natural Luminosity for the C_1 MCCI Case, at Several Combustion Phasing of Interest (SOI_{DIESEL} = -8 CAD ATDC, 63% ESR, 1000 RPM, 6.7 bar IMEP). The Corresponding Timing on the AHRR and SINL Traces is Also Shown for Clarity

Image analysis of diesel-ethane dual-fuel combustion in MCCI mode is presented in Figure 70. The same diesel injection duration and gaseous fuel energy delivery was maintained and assumed to be subjected to the same slip rate. The addition of ethane delayed the mean CA5 by ~1.9 CAD compared to the diesel base for the cycle shown, also a 0.7 CA increase compared to methane. The

AHRR data suggests that the ignition delay was the same as methane (~ 2.6 CAD) but with delayed phasing and that the same mechanical start of injection was maintained, however the end of injection was again not visible due to lower soot reflective luminosity. Combustion analysis indicated the CA5 to CA50 duration was ~ 2.1 CAD, the CA50 to CA90 duration was ~ 13.2 CAD, and CA50 to CA95 duration was ~ 21.8 CAD. This marked a faster overall combustion process compared to methane addition. Combustion specifics from both image and pressure data analysis are presented next.

The even longer ignition delay from ethane addition also resulted loss of fuel jet visibility. CA10 now coincided with the earliest noticeable luminosity, but at multiple jet locations, again slightly before the peak of the AHRR. As with methane addition this suggests the early combustion was dominated by premixed burn. The diesel injection should have ended between CA20 and CA30 considering the same injection command was used for the dual-fuel case as the diesel base condition. The CA50 image occurred 1.8 CAD after CA10 and shows simultaneous mixing-controlled and premixed combustion, like methane. This was slightly before the maximum SINL value. The maximum SINL value occurs at ~6.5 CAD ATDC which was slightly after CA60. It then takes 10.3 CA from CA70 to CA90 and 18.8 CA from CA70 to CA95 to complete the combustion process, with AHRR and imaging suggesting it was a combined premixed and mixing-controlled process. SINL at CA95 was close to zero. The lack of soot radiation inside the piston bowl captured in CA95 image suggests the cycle finished with premixed combustion at low temperature. Late-stage combustion (CA70) fuel dribbles near the injector were more dispersed compared to methane case with slightly more premixed flame area visible at CA90.

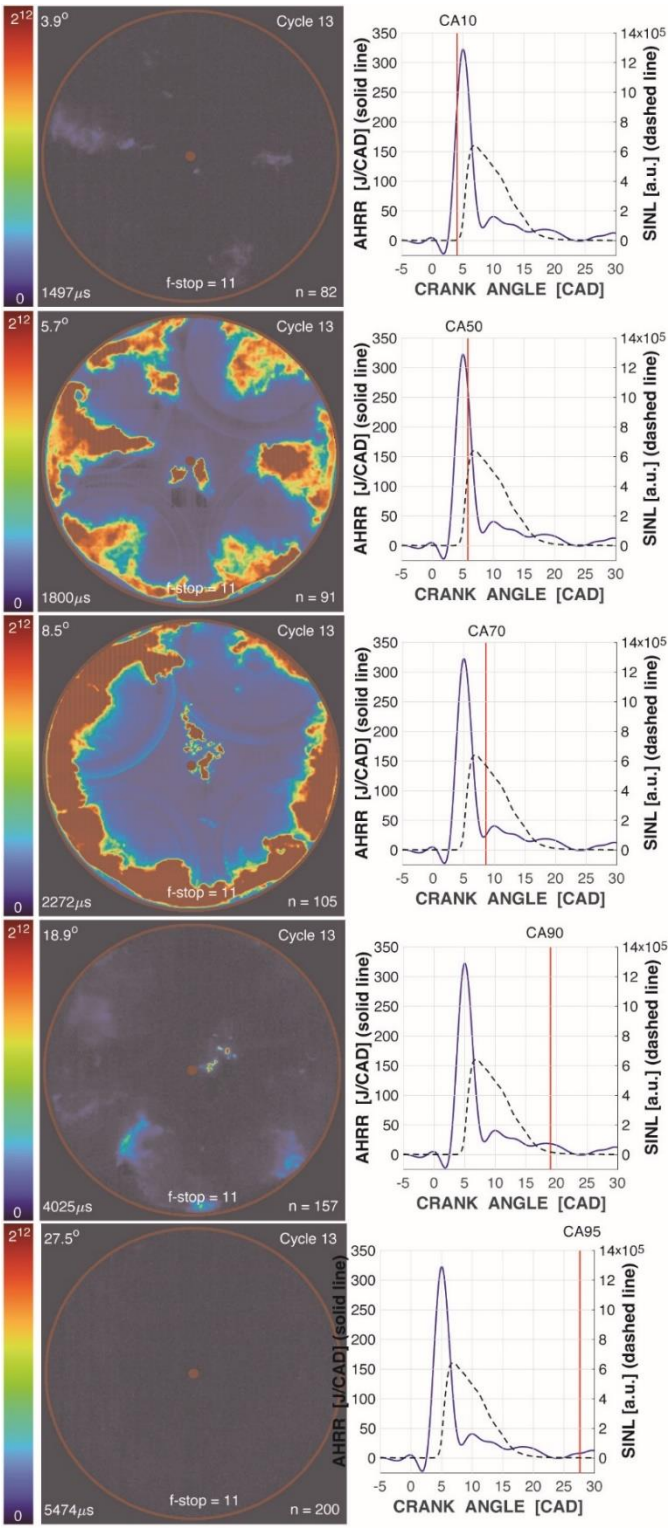

Figure 70-Image Data: In-Cylinder Natural Luminosity for the C_2 MCCI Case, at Several Combustion Phasing of Interest (SOI_{DIESEL} = -8 CAD ATDC, 63% ESR, 1000 RPM, 6.5 bar IMEP). The Corresponding Timing on the AHRR and SINL Traces is Also Shown for Clarity

Image analysis of diesel-propane dual-fuel combustion in MCCI mode is presented in Figure 71, subject to the same fueling process as methane and ethane cases. The addition of propane delayed the mean CA5 by ~1.7 CAD compared to the diesel base for the cycle shown, more than methane but less than ethane. The AHRR data suggests that the ignition delay was shortened compared to methane and ethane to ~ 2.2 CAD but was delayed in phasing like ethane. Combustion analysis indicated the CA5 to CA50 duration was ~ 2.3 CAD, the CA50 to CA90 duration was ~ 14.2 CAD, and CA50 to CA95 duration was ~ 22.2 CAD. Combustion specifics from both image and pressure data analysis are presented next.

The diesel jets again were not clearly visible for propane addition. Like methane, CA20 coincided with the earliest noticeable luminosity, at three jet locations, and occurred slightly before the peak of the AHRR. Once again, early combustion heat release was dominated by premixed combustion. At the time the diesel injection ended the combustion process progressed to CA30. The CA50 image occurred 1.4 CAD after CA20, faster than methane, and shows early signs of a two-stage combustion process. The CA50 image was slightly before the SINL peak (~70% of the maximum). Like methane, but not ethane, fuel dribbles were not present at CA50. The maximum SINL value occurs at ~6.8 CAD ATDC which was just after CA60. It then takes 10.6 CA from CA70 to CA90 and 18.6 CA from CA70 to CA95 to complete the combustion process, again a combined premixed and mixing-controlled process. SINL at CA90 also was close to zero, as was the methane case. The CA90 image had even lower intensity than methane or ethane, with some pockets of soot lightly visible. Late-stage combustion (CA70) injector dribble was more spread out than methane but less than ethane.

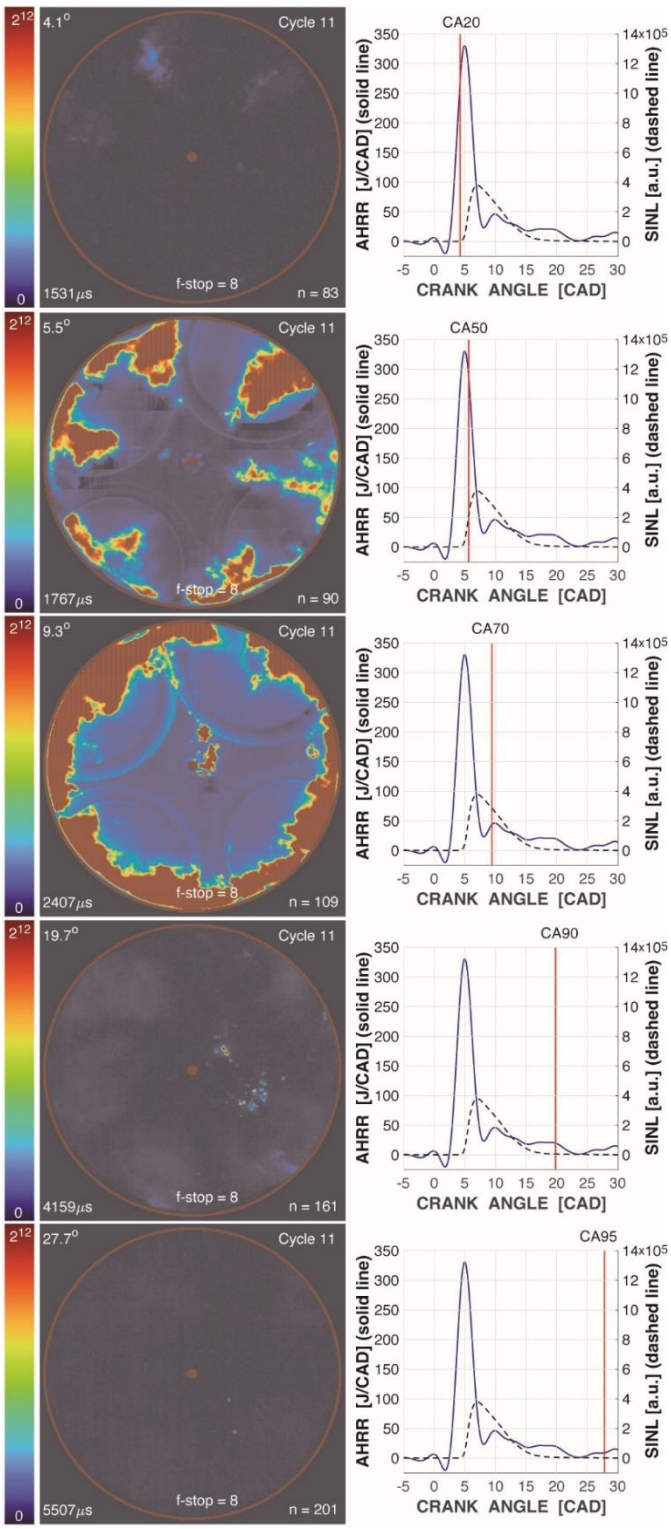

Figure 71-Image Data: In-Cylinder Natural Luminosity for the C_3 MCCI Case, at Several Combustion Phasing of Interest (SOI_{DIESEL} = -8 CAD ATDC, 63% ESR, 1000 RPM, 6.6 bar IMEP). The Corresponding Timing on the AHRR and SINL Traces is Also Shown for Clarity

5 Conclusions

This study presents a three-part investigation on the effects of natural gas (NG) major components (i.e., methane, ethane, propane, and butane, or C_1-C_4) fraction on the combustion phenomena inside a dual-fuel diesel-NG engine operating at low-load conditions. The objective was to improve the understanding of NG composition effects at low-load dual-fuel operation in terms maximum diesel substitution rate, engine efficiency, and engine-out emissions. Experimental platforms consisted of (i) a conventional metal diesel engine operating at 40% diesel energy substitution rate (ESR), (ii) an optically accessible single cylinder version of the same metal diesel engine operating at 63% ESR under both mixing-controlled compression ignition (MCCI) and reactivity-controlled compression ignition (RCCI) conditions, and (iii) a laminar flame burner that measured laminar flame speeds of the C_1-C_4 gas mixtures used in engine experiments. Engine experiments were performed at a constant engine speed of 1000 RPM at 1000 bar and 500 bar diesel injection pressure for the metal engine and optical engine, respectively. This resulted in an engine load of ~6.6 bar indicated mean effective pressure (IMEP) for optical engine experiments and ~6.15 bar brake mean effective pressure (BMEP) for metal engine experiments. Optical engine experiments provided insight into the mixture mixing and stratification of different gas components interacting with the diesel spray.

Metal engine experiments replaced part of the diesel fuel with seven different gas blends containing methane (M), ethane (E), propane (P), and butane (B): M100, M90E5P5, M90E5B5, M80E10P10, M90E10, M90P10, and M90B10, where the numbers represent the volumetric percentage of the species in that gaseous mixture. In-cylinder pressure rise rate limited the diesel substitution rate to 40% for engine operation without EGR. The decision to not use EGR was taken to avoid EGR interference with the evaluation of the effects of each individual fuel component and to better compare with optical engine results. The total fuel energy (diesel or diesel plus C_1-C_4 blends) was held constant. C_1-C_4 blend was injected inside the intake manifold just before the intake valve using low-pressure gas injectors. Three different diesel injection timings around the pure-diesel maximum brake torque (MBT) timing were used. Therefore, the ignition timing was similar to the one in a conventional diesel engine. The main conclusions of the metal engine experiments at low-load conditions were:

- Dual-fuel operation reduced BMEP compared to the diesel baseline, but the gas composition effect was limited. Up to 80% higher rates of pressure rise compared to the diesel baseline limited the substitution rate to 40% ESR without EGR, irrespective of the injection timing. Engine operation was robust for all gas compositions, evidenced by a COV_{IMEP} below 3%. Most stable operation was achieved with pure methane (M100).
- The dual-fuel combustion process was a two-stage heat release for all gas blends, separated by a burn inside the piston bowl before TDC and a burn in the squish region after TDC. M90B10 had some degree of merging between the two heat release stages in the two regions, suggesting a stronger flame propagation. M90B10 also produced the highest peak pressure and more advanced CA50 at all SOI_{DIESEL}; however, M90P10 had the highest BMEP, hence the best BSFC and thermal efficiency. Surprisingly M90E5B5 had the worst BSFC, followed by M90E10, suggesting fuel component combination effects were more complex than just the addition of their physical or chemical properties.
- M100 had the longest diesel fuel vaporization and ignition delay. The most noticeable differences between gas blends occurred during the late-stage fuel oxidation for early SOI_{DIESEL}. M100 had the largest increase in the ignition delay (~1 CAD at SOI_{DIESEL} = TDC), the largest CA50 delay (~2 CAD), and largest increase in the combustion duration (2-3 CAD) compared to the baseline diesel, roughly double the increase experienced by the other gas mixtures.
- In-cylinder pressure correlated with the gas mixture autoignition temperature (i.e., the order was M90B10 > M90P10 > M90E10 > M100). M90B10 and M90P10 generally had a higher and more advanced location of maximum cylinder pressure compared to other blends, however the location delayed for M90B10 at TDC. As a result, the mixtures with a higher carbon content had the best performance, with M100 being the worst. This would suggest it is beneficial from a combustion perspective to maintain a higher NGL fraction in the NG for low-load dual-fuel operation.
- Dual-fuel operation reduced $BSCO_2$ and $BSNO_x$ emissions up to 6.6% and 20%, respectively. However, it was offset by the large increase in BSCO and BSHC emissions, which could require after-treatment modifications. $BSCO_{2,eq}$ was sensitive to methane content and generally reduced for gas blends with lower methane content. Specifically,

M80E10P10 reduced $BSCO_{2,eq}$ by ~50 g/kWh, while among the M90 blends butane addition had the largest reduction followed by propane then ethane.

Laminar flame burner experiments were conducted to evaluate differences between the seven C_1-C_4 gas blends. The results for pure methane were compared to existing literature to validate the evaluation method, with maximum deviation of ~11%. The same method employed on other blends. Data from laminar flame speed measurements was deemed too similar and inconsistent to make any reasonable conclusions on performance difference at the low equivalence ratios, higher pressures and temperatures, and turbulent environment tested under dual-fuel engine operation.

As combustion differences between different gas compositions tended to be small during metal engine experiments, optical engine experiments operated with pure NG components to observe the maximum possible difference. A separate case in which the engine was operated using just low-sulfur diesel fuel at the same diesel mass per cycle as for the MCCI and RCCI operation helped to visualize the effect of adding the gas to the engine. Natural luminosity (NL) images of the combustion phenomena (including calculations of the spatially integrated NL, SINL) complemented the traditional engine performance analysis based on the in-cylinder pressure data and engine-out emissions. The operating mode had a substantial impact on the timing of the SINL signal with relation to the heat release location. The main conclusions were:

- NL images confirmed the premixed nature of the combustion for RCCI mode (SOI_{DIESEL} = -40 CAD ATDC). The combustion started inside the squish area and propagated towards the center of the combustion chamber. The high intensity NL regions that appeared towards the end of the premixed combustion were the result of the diffusive combustion of end-of-injection fuel dribble or of the diesel fuel that condensed on the bowl window surface or accumulated in the bowl straight corners (typical of an optical engine piston).
- Differences in oxidation properties between NG components affected the RCCI combustion at these low load conditions. Propane RCCI was characterized by 1 CA to 3 CA more advanced combustion phasing (despite an increased ignition delay) and higher SINL compared to methane and ethane RCCI. However, as NL for the propane RCCI was lower at similar combustion phasing, it suggests that propane addition created a more

stratified diesel-gas mixture, with a richer mixture inside the squish volume, supported by faster and more intense combustion compared to the other two RCCI cases. As a result, the flame speed slowed as it progressed from the squish volume towards the center of the combustion chamber, therefore the delay in capturing the premixed combustion in the NL images. However, the differences between methane RCCI and ethane RCCI were negligible, at least for these operating conditions.

- For RCCI, the amount of fuel that burned after the premixed combustion completely engulfed the piston bowl was relatively low compared to the fraction of the fuel that burned before it. RCCI results suggest the importance of tailoring the low-high fuel reactivity ratio (i.e., ESR) of the dual-fuel combustion based on the operating condition.
- AHRR data under MCCI mode (SOI_{DIESEL} = -8 CAD ATDC) suggested a significant premixed burn inside the bowl region early in the combustion process, which was masked by the higher filter requirements used to see the later stage combustion. The combustion process subsequently proceeds into a mixing-controlled combustion mode after the initial premixed diesel spray and NG mixture is consumed. MCCI with ethane had the highest ignition delay and shortest combustion duration of the pure components, which resulted in a slightly lower total heat release. Methane had a later CA90 and longest combustion duration as a result and continued to burn late into the expansion stroke as compared to ethane and propane.
- For MCCI the SINL max for diesel (~6.3 CAD ATDC) occurs slightly before dual-fuel cases (~6.7 CAD ATDC, ~6.5 CAD ATDC, ~6.8 CAD ATDC) for methane, ethane, and propane, respectively. The bulk of the mixing-controlled process visible combustion occurs at CA50 and CA70. The addition of NG components (higher energy content) clearly increases the NL (soot) in the fuel jet plumes compared to the diesel base injection quantity.

Engine data provided a high level of detail into fuel compositional effects on combustion characteristics relevant to diesel-NG dual-fuel engines. Results suggest that conventional diesel engines converted to diesel-NG dual-fuel operation can tolerate larger changes in NG composition, even pure components, with no MN limitations at substitution rates less than or equal to 40% by energy. While high energy substitution rates may be considered for high-load conditions (albeit with significant engine modifications), it may be more beneficial in terms of engine efficiency,

emissions, and number of modifications required to use lower energy substitution rates at low load conditions. Moreover, the use of lower substitution rate offers an economical solution for recovering the energy of available NG components with limited effects on combustion characteristics and no limit on NG fuel composition. Finally, data and findings presented in this study complement future dual-fuel modeling with C_1-C_4 gas blends and can help direct industry in utilizing fuels with higher C_2-C_4 content more efficiently.

6 Recommendations for Future Work

Based on the findings of this work, future experiments should be conducted to better analyze the effects of NG fuel composition at different load and speed, utilizing both the metal and optical engine platforms. Metal engine data already collected during the experimental campaign will be used to present the effects of different ESR from 0-80% at low load and low speed in future publications. The low load and low speed ESR data needs complimentary optical engine experiments to accommodate the results to give a broader sense of fuel stratification and premixing effects on combustion. Also, metal engine experiments looking at NG composition effects with EGR should be conducted. Sensors for measuring the intake and exhaust CO_2 were purchased for the research but the time required for optical engine experiments did not allow for re-examination of EGR operation on the metal engine. The EGR experiments can be re-created in the optical engine by using CO_2 cylinders and gas heaters to provide a mimicking effect of the EGR inert gas. The feasibility of pentane mixtures should be re-examined. The delivery of pentane in gaseous state to the engine could be possible with the proper fuel heating mechanism placed near the engine intake. Another possibility for delivery would be a liquid drip system placed near the engine intake port with fuel consumption measured by a fuel scale.

Optical engine experiments conducted using NG fuel blends should be performed to determine if any distinguishable features are present at low load and low speed. The data presented in this work will provide a baseline for result expectations. Also, the optical engine laboratory setup requires modification to conduct experiments using laser sheet illumination for radical excitation at the OH wavelength. This will provide more information on the combustion characteristics observed in this work.

The engine testbeds can be used to support future student research on numerous topics, suggested topics include diesel-hydrogen and diesel-ammonia dual fuel experiments. Also, experiments could analyze different renewable synthetic diesel fuels and bio-diesel effects. All experiment can be complimented by optical engine investigations to provide high fidelity combustion data.

7 References

[1] K. Tsai and N. Ameen, "Today in energy: EIA expects 2018 and 1029 natural gas prices to remain relatively flat," U.S. Energy Information Administration, 25 Jan 2018. [Online]. Available: https://www.eia.gov/todayinenergy/detail.php?id=34672. [Accessed 22 Oct 2018].

[2] T. Hodge, "Today in energy," U.S.. Energy Information Administration , 22 January 2018. [Online]. Available: https://www.eia.gov/todayinenergy/detail.php?id=34612. [Accessed 6 June 2018].

[3] "How much carbon dioxide is produced when different fuels are burned?," U.S. Energy Information Administration , 8 June 2018. [Online]. Available: https://www.eia.gov/tools/faqs/faq.php?id=73&t=11. [Accessed 13 June 2018].

[4] "Monthly energy review," U.S. Energy Information Administration, 26 August 2021. [Online]. Available: https://www.eia.gov/totalenergy/data/monthly. [Accessed 2 September 2021].

[5] "Weekly retail gasoline and diesel prices," U.S. Energy Information Administartion, 23 May 2022. [Online]. Available: https://www.eia.gov/dnav/pet/pet_pri_gnd_dcus_nus_w.htm. [Accessed 27 May 2022].

[6] M. Foss, J. Wardzinski and F. Delano, "Interstate natural gas - Quality specifications & interchangeability," Center for Energy Economics, Austin Texas, 2004.

[7] Reuters, [Online]. Available: https://www.reuters.com/business/energy/us-heating-oil-diesel-stocks-dwindle-demand-rises-2022-02-04/. [Accessed 12 February 2022].

[8] M. Muralidharan, A. Srivastava and M. Subramanian, "A technical review on performance and emissions of compressed natural gas-diesel dual fuel engine," *SAE International*, 2019.

[9] C. Guido, P. Napolitano, V. Fraioli, C. Beatrice and N. D. Giacomo, "Assessment of engine control parameters effect to minimize GHG emissions in a dual fuel NG/diesel light duty engine," *SAE International*, no. doi:10.4271/2018-01-0266, 2018.

[10] R. Robbio, M. Cameretti, E. Mancaruso, R. Tuccillo and B. Vaglieco, "Combined CFD-experimental analysis of the in-cylinder combustion phenomena in a dual-fuel optical compression ignition engine," *SAE International*, no. doi:10.4271/2021-24-0012, 2021.

[11] J. B. Heywood, Internal Combustion Engine Fundamentals- Indian Edition, New Delhi : McGraw Hill, 1988.

[12] J. Lui and C. Dumitrescu, "Flame development analysis in a diesel optical engine converted to spark ignition natural gas operation," *Applied Energy,* vol. 230, no. doi:10.1016/2018.09.059, pp. 1205-1217, 2018.

[13] A. Boretti, "Advantages and disadvantages of diesel single and dual-fuel engines," *Frontiers in Mechanical Engineering,* no. doi:10.3389/fmech.2019.00064, 2019.

[14] Y. Suzuki and T. Tsujimura, "The combustion improvements of hydrogen/ diesel dual fuel engine," *SAE International,* no. doi:10.4271/2015-01-1939, 2015.

[15] C. Nilson, D. Biles, B. Yraguen and C. Mueller, "Ducted fuel injection versus conventional diesel combustion: An operating-parameter sensitivity study conducted in an optical engine with a four-orifice fuel injector," *SAE Int. J. Engines,* no. doi:10.4271/03-13-03-0023, 2020.

[16] C. Nilson, D. Biles, B. Yraguen and C. Mueller, "Ducted fuel injection vs. conventional diesel combustion: Extending the load range in an optical engine with a four-orifice injector," *SAE Int. J. Engines,* no. doi:10.4271/03-14-01-0004, 2021.

[17] M. Palanisamy, J. Lorch, R. Truemner and B. Baldwin, "Combustion characteristics of a 3000 bar diesel fuel injection system on a single cylinder research engine," *SAE International,* no. doi:10.4271/2015-01-2798, 2015.

[18] Y. Suzuki, T. Tsujimura and T. Mita, "The performance of multi-cylinder hydrogen/diesel dual fuel engine," *SAE International,* no. doi:10.4271/2015-24-2458, 2015.

[19] R. Gehmlich, C. Dumitrescu, Y. Wang and C. Mueller, "Leaner lifted-flame combustion enabled by the use of an oxygenated fuel in an optical CI engine," *SAE International,* no. doi:10.4271/2016-01-0730, 2016.

[20] "Cooperative patent classification," USPTO, January 2018. [Online]. Available: https://www.uspto.gov/web/patents/classification/cpc/html/cpc-F02D.html. [Accessed 9 January 2018].

[21] "Dual fuel conversions," PENN Power Group, 2021. [Online]. Available: https://pennpowergroup.com/solutions/dual-fuel-conversions/#. [Accessed 23 July 2021].

[22] X. Yang, V. Vinhaes, M. Turcios, J. Huang and J. Naber, "Process for study of micro-pilot diesel-NG dual fuel combustion in a constant volume combustion vessel utilizing

the pre-mixed pre-burn procedure," *SAE International,* no. doi:10.4271/2019-01-1160, 2019.

[23] "Hydrocarbons- Autoignition temperatures and flash points," Engineering Toolbox, 2017. [Online]. Available: https://www.engineeringtoolbox.com/flash-point-autoignition-temperature-kindling-hydrocarbons-alkane-alkene-d_1941.html. [Accessed 25 May 2022].

[24] I. Glassman, R. Yetter and N. Glumac, Combustion (Fifth Edition) :Appendix F-Laminar flame speeds, Academic Press, 2015.

[25] K. Aung, L. Tseng, M. Ismail and G. Faeth, *Combustion and Flame,* p. 526, 1995.

[26] M. Hassan, K. Aung and G. Faeth, "Measured and predicted properties of laminar premixed methane/air flames at various pressures," *Combustion and Flame,* vol. 115, pp. 539-550, 1998.

[27] C. Vagelopoulos, F. Egolfopoulos and C. Law, *Proc. Combust. Inst. ,* 1994.

[28] C. K. Law, Combustion Physics, New York: Cambridge University Press, 2006.

[29] J. G. Speight, The Chemistry and Technology of Petroleum: Fourth Edition, Boca Raton, F.L.: Taylor & Francis Group, LLC., 2007.

[30] U. Dengel, S. Karode and Y. Ding, "Streamlined natural gas treatment by membranes only," in *Offshore Technology Conference,* Houston, Texas, 2019.

[31] BP, "BP aims for zero routine flaring in US onshore operations by 2025," BP, 18 April 2021. [Online]. Available: https://www.bp.com/en_us/united-states/home/news/features-and-highlights/bp-aims-for-zero-routine-flaring-in-us-onshore-operations-by-2025.html. [Accessed 25 May 2022].

[32] "Emissions Study: Electra Therm Power+ Generator compared to open flaring," Texas A&M, 2015.

[33] "TCG 2020," Caterpiller Energy Solutions GMBH, 2021. [Online]. Available: https://www.mwm.net/en/gas-engines-gensets/gas-engine-tcg-2020/. [Accessed 16 June 2021].

[34] "Electronic Code of Federal Regulations," e-CFR, 5 January 2018. [Online]. Available: https://www.ecfr.gov/cgi-bin/text-idx?SID=fc799a21d4ca6f413913715af7c09e88&mc=true&node=pt40.36.1054&rgn=div5. [Accessed 9 January 2018].

[35] "EPA Tier 5: What we know so far," Woodstock Power Compay, 2021. [Online]. Available: https://woodstockpower.com/blog/epa-tier-5-what-we-know-so-far/. [Accessed 18 Oct 2021].

[36] "Ground-level ozone basics," US EPA, 31 Oct. 2018. [Online]. Available: https://www.epa.gov/ground-level-ozone-pollution/ground-level-ozone-basics#formation. [Accessed 8 Aug. 2018].

[37] "Technical overview of volatile organic compounds," US EPA, 12 April 2017. [Online]. Available: https://www.epa.gov/indoor-air-quality-iaq/technical-overview-volatile-organic-compounds. [Accessed 8 August 2018].

[38] "NAAQS Table," US EPA, 20 Dec 2016. [Online]. Available: https://www.epa.gov/criteria-air-pollutants/naaqs-table. [Accessed 8 Aug 2018].

[39] "Understanding global warming potentials," EPA, 9 September 2020. [Online]. Available: epa.gov/ghgemissions. [Accessed 2 August 2021].

[40] "Hydrocarbon GWPs and indirect GWPs," European FluoroCarbos Technical Committee, [Online]. Available: https://www.fluorocarbons.org/environment/climate-change/hydrocarbon-gwps-and-indirect-gwps/. [Accessed 30 March 2022].

[41] P. K. Karra, "Parametric study and optimization of diesel engine operation for low emissions using different injectors," Iowa State University, Ames, Iowa, 2009.

[42] J. Weber, O. Herrmann, R. Puts, J. Kawamure, Y. Tomida and M. Mashida, "Next improvement potentials for heavy-duty diesel engine- Tailor the fuel injection system to the combustion needs," *SAE International,* no. doi:10.4271/2017-01-0705, 2017.

[43] M. Darzi, D. Johnson and C. Ulishney, "Gaseous fuels variation effects on first and second law analyses of a small direct injection engine for micro-CHP systems," *Energy Conversion and Management ,* 2018 (pending publication).

[44] H. Bommisetty, J. Liu, Kooragayala, R and C. Dumitrescu, "Fuel composition effects in a CI engine conveted to SI natural gas operation," *SAE International,* no. doi:10.4271/2018-01-, 2018.

[45] L. Ambrogi, J. Liu, M. Battistoni, C. Dumitrescu and L. Gasbarro, "CFD investigation of the effects of gas' methane number on the performance of a heavy-duty natural-gas spark-ignition engine," *SAE International,* no. doi:10.4271/2019-24-0008, 2019.

[46] "ISL G Near Zero," Cummins Westport, [Online]. Available: http://www.cumminswestport.com/models/isl-g-near-zero. [Accessed 13 June 2018].

[47] "G3616 A4," Caterpillar, 2021. [Online]. Available: https://www.cat.com/en_US/products/new/power-systems/oil-and-gas/gas-compression-engines/1000000845.html. [Accessed 16 June 2021].

[48] M. Feist, M. Landau and E. Harte, "The effect of fuel composition on performance and emissions of a variety of natural gas engines," *SAE International* , no. 2010-01-1476, 2010.

[49] S. Thipse, A. Kulkarni and S. Vispute, "Development of dual fuel (diesel-CNG) engine for SUV application in India," *SAE International*, no. doi:10.1472/2015-26-0058, 2015.

[50] A. Magno, E. Mancaruso and B. Vaglieco, "Combustion analysis of dual fuel operation in single cylinder research engine fueled with methane and diesel," *SAE International*, no. doi:10.4271/2015-24-2461, 2015.

[51] H. Ogawa, P. Zhao, T. Kato and G. Shibata, "Improvement of combustion and emissions in a dual fuel compression ignition engine with natural gas as the main fuel," *SAE International*, no. doi:10.4271/2015-01-0863, 2015.

[52] F. Konigsson, H. Dembinski and H. Angstrom, "The influence of in-cylinder flows on emissions and heat transfer from methane-diesel dual fuel combustion," *SAE Int. J. Engines*, no. doi10.4271/2013-01-2509, 2013.

[53] S. Ouchikh, M. Lounici, K. Loubar, L. Tarabet, Tazerout and M, "Effect of diesel injection strategy on performance and emissions of CH4/diesel dual-fuel engine," *Fuel* , no. doi:10.1016/j.fuel.2021.121911, 2021.

[54] M. Besch, J. Israel, A. Thiruvengadam, H. Kappanna and D. Carder, "Emissions characterization from different technology heavy-duty engines retrofitted for CNG/diesel dual-fuel operation," *SAE International*, no. doi:10.4271/2015-01-1085, 2015.

[55] M. Gopalakrishnan and F. Tischer, "Torque model for a dual fuel engine," *SAE International*, no. doi:10.4271/2014-01-2417, 2014.

[56] B. Zhang, S. Mazlan, S. Jiang and A. Boretti, "Numerical investigation of dual fuel diesel-CNG combustion on engine performance and emissions," *SAE International*, no. doi:10.4271/2015-01-0009, 2015.

[57] C. Lee, Y. Pang, H. Wu, J. Hernandez, S. Zhang and F. Liu, "The optical investigation of hydrogen enrichment effects on combustion and soot emission characteristics of CNG/diesel dual fuel engine," *Fuel*, no. doi:10.1016/j.fuel.2020.11839, 2020.

[58] M. Karimi, X. Wang, J. Hamilton and M. Negnevitsky, "Status, challenges and opertunities of dual fuel hybrid approaches- a review," *International Journal of Hydrogen Energy,* no. doi:10.1016/j.ijhydene.2021.08.008, 2021.

[59] D. Healy, D. Kalitan, C. Aul, E. Peterson, G. Bourque and H. Curran, "Oxidation of C1-C5 alkane quinternary natural gas mixtures at high pressures," *Energy Fuels,* vol. 24, pp. 1521-1528, 2010.

[60] G. Bourque, D. Healy, H. Curran, C. Zinner, D. Kalitan, J. Vries, C. Aul and E. Peterson, "Ignition and flame speed of two natural gas blends with high levels of Heavier hydrocarbons," *Journal of Engineering for Gas Turbones and Power,* vhl. 132, 2010.

[61] S. Krishnan, K. Srinivasan and M. Raihan, "The effect of injection parameters and boost pressure on diesel-propane dual fuel low temperature combustion in a single cylinder research engine," *Fuel,* vol. 184, pp. 490-502, 2016.

[62] A. Polk, C. Gibson, M. Shoemaker, K. Srinivasan and S. Krishnan, "Analysis of ignition behavior in a dual fuel turbocharged direct injection engine using propane and methane as primary fuels," *ASME J. Energy Res. Tech.,* vol. 135, no. 3, 2013.

[63] A. Yousefi, M. Birouk and H. Guo, "An experimental and numerical study of the effect of diesel injection timing on natural gas/ diesel dual-fuel combustion at low load," *Fuel,* vol. 203, pp. 642-657, 2017.

[64] Z. Wang, M. Shao, M. Li, D. Wang and Z. Liu, "Effect of pilot diesel multiple injections on the performance and emissions of a diesel/natural gas dual fuel heavy-duty engine," *SAE International,* no. doi:10.4271/2017-01-2271, 2017.

[65] W. Kim, C. Park and C. Bae, "Combustion phenomena and emissions in a dual-fuel optical engine fueled with diesel and natural gas," *SAE International,* pp. 502-513, 2021.

[66] A. Yousefi, H. Guo, M. Birouk, B. Liko and S. Lafrance, "Effect of post-injection startegy on grenhouse gas emissions of natural gas / diesel dual-fuel engine at high load conditions," *Fuel,* no. doi:10.1016/j.fuel.2020.120071, 2020.

[67] A. Yousefi, H. Guo, S. Dev, B. Liko and S. Lafrance, "Effect of pre-main-post diesel injection strategy on greenhouse gas and nitrogen oxide emissions of natural gas/diesel dual-fuel engine at high loads," *Fuel,* no. doi:10.1016/j.fuel.2021.121110, 2021.

[68] F. Felayati, Semin, B. Cahyono, R. Bakar and M. Birouk, "Performance and emissions of natural gas/diesel dual-fuel engine at low load conditions: Effect of natural gas split injection strategy," *Fuel,* no. doi:10.1016/j.fuel.2020.121012, 2021.

[69] M. Cameretti, R. Robbio and R. Tuccillo, "Performance improvement and emission control of a dual fuel operated diesel engine," *SAE International,* no. doi:10.4271/2017-24-0066, 2017.

[70] X. Liu, H. Wang, Z. Zheng and M. Yao, "Numerical investigation on the combustion and emission characteristics of a heavy-duty natural gas-diesel dual-fuel engine," *Fuel,* no. doi:10.1016/j.fuel.2021.120998, 2021.

[71] J. Liu, Q. Guo, J. Guo and F. Wang, "Optimization of a diesel/natural gas dual fuel engine under different diesel substitution ratios," *Fuel,* no. doi:10.1016/j.fuel.2021.121522, 2021.

[72] D. Kozarac, M. Sremec, M. Bozic and A. Vucetic, "The performance and emissions of a conventional natural gas/diesel dual fuel engine at various operating conditions," *SAE International,* no. doi:10.4271/2019-01-1158, 2019.

[73] A. Yousefi, H. Guo, M. Birouk and B. Liko, "On greenhouse gas emissions and thermal efficiency of natural gas /diesel dual-fuel engine at low load conditions: Coupled effect of injector rail pressure and split injection," *Applied Energy,* vol. 242, pp. 216-231, 2019.

[74] D. Hariharan, S. Krishnan and K. Srinivasan, "Multiple injection strategies for reducing HC and CO emissions in diesel-methane dual-fuel low temperature combustion," *Fuel,* no. doi:10.1016/j.fuel.2021.121372, 2021.

[75] Z. Wang, Z. Zhao, D. Wang, M. Tan, Y. Han, Z. Liu and H. Dou, "Impact of pilot diesel ignition mode on combustion and emissions characteristcs of a diesel/ natural gas dual fuel heavy-duty engine," *Fuel,* vol. 167, pp. 248-256, 2016.

[76] H. Guo, B. Liko, L. Luque and J. Littlejohns, "Combustion performance and unburned hydrocarbon emissions of a natural gas-diesel dual fuel engine at low load condition," *J Eng. Gas Turbines Power,* no. doi:10.1115/1.4039758, 2018.

[77] S. Dev, H. Guo, S. Lafrance and B. Liko, "An experimental study on the effect of exhaust gas recirculation on a natural gas-diesel dual-fuel engine," *SAE International,* 2020.

[78] J. You, Z. Liu, Z. Wang, D. Wang, Y. Xu, G. Du and X. Fu, "The exhausted gas recirculation improved brake thermal efficency and combustion characteristics under different intake throttling conditions of a diesel/natural gas dual fuel engine at low loads," *Fuel,* no. doi:10.1016/j.fuel.2020.117035, 2020.

[79] W. Zhang, T. Feng, Z. Li, Z. Chen and J. Zhao, "EGR thermal and chemcial effects on combustion and emission of diesel/ natural gas duel-fuel engine," *Fuel,* no. doi:10.1016/j.fuel.2021.121161, 2021.

[80] A. Raj, V. Nagarajan, J. Nissangi and V. Elango, "Development of an all speed governed diesel-CNG dual fuel engine for farm applications," *SAE International,* no. doi:10.4271/2021-26-0101, 2021.

[81] H. Manns, M. Brauer, H. Dyja, H. Beier and A. Lasch, "Diesel CNG: The potential of a dual fuel combustion concept for lower CO2 and emissions," *SAE International,* no. doi:10.4271/2015-26-0048, 2015.

[82] Z. Wang, X. Fu, D. Wang, Y. Xu, G. Du and J. You, "A mulitlevel study on the influence of natural gas substitution rate on combustion mode and cyclic variation in a diesel/natural gas dual fuel engine," *Fuel,* no. doi:10.1016/j.fuel.2021.120499, 2021.

[83] R. Papagiannakis, D. Hountalas, S. Krishnan, K. Srinivasan, D. Rakopoulous and C. Rakopoulous, "Numerical evaluation of the effects of compression ratio and diesel fuel injection timing on the performance and emissions of a fumigated natural gas-diesel dual-fuel engine," *J. Energy Eng.,* 2016.

[84] D. Clemens, D. Renner and K. Masser, "Dual fuel- Potential of combined combustion of CNG and diesel fuel," *SAE International,* no. doi:10.4271/2013-36-0133, 2013.

[85] A. Talekar, M. Lai, E. Tomita, N. Kawahara, Zeng and Yang, "Numerical investigation of natural gas-diesel dual fuel engine with end gas ignition," *SAE International,* no. doi:10.4271/2018-01-0199, 2018.

[86] Y. Li, H. Guo and H. Li, "Evaluation of kinetic process in CFD model and its application in ignition process analysis of a natural gas-diesel dual fuel engine," *SAE International,* no. doi:10.4271/2017-01-0554, 2017.

[87] Y. Yoshimoto, E. Kinoshita, S. Luge and T. Ohmura, "Combustion characteristics of a dual fuel diesel engine with natural gas (lower limit of cetane number for ignition of the fuel)," *SAE International,* no. doi:10.4271/2012-01-1690, 2012.

[88] Z. Ahmad, O. Kaario, C. Qiang and M. Larmi, "Effect of pilot fuel properties on lean dual-fuel combustion and emission characteristics in a heavy-duty engine," *Applied Energy,* no. doi:10.1016/j.apenergy.2020.116134, 2020.

[89] Z. Zhu, Y. Li and C. Shi, "Effects of natural gas energy fractions on combustion performance and emission characteristics in an optical CI engine fueled with natural gas/diesel dual-fuel," *Fuel,* no. doi:10.1016/j.fuel.2021.121842, 2021.

[90] P. Garcia and P. Tunestal, "Experimental investigation on CNG-diesel combustion modes under highly diluted conditions on a light-duty diesel engine with focus on injection strategy," *SAE International,* no. doi:10.4271/2015-24-2439, 2015.

[91] W. Kim, C. Park and C. Bae, "Characterization of combustion process and emissions in a natual gas/ diesel dual-fuel compression-ignition engine," *Fuel*, no. doi:10.1016/j.fuel.2020.120043, 2020.

[92] C. Lee, Y. Pang, H. Wu, K. Nithyanandan and F. Liu, "An optical investigation of substitution rates on natural gas/diesel dual-fuel combustion in a diesel engine," *Applied Energy*, no. doi:10.1016/j.apenergy.2019.114455, 2019.

[93] Z. Wang, F. Zhang, Y. Xia, D. Wang, Y. Xu and G. Du, "Combustion phase of a diesel/natural gas dual fuel engine under various pilot diesel injection timings," *Fuel*, no. doi:10.1016/j.fuel.2020.119869, 2020.

[94] S. Lee, C. Kim, S. Lee, S. Oh, J. Kim and J. Lee, "Characteristics of non-methane hydrocarbons and methane emissions in exhaust gas under atural-gas/diesel dual fuel combustion," *Fuel*, no. doi:10.1016/j.fuel.2020.120009, 2020.

[95] M. Selim and H. Saleh, "Performance and noise of dual fuel engine running on cottonseed, soybean raw oils and their methyl esters as pilot fuels," *SAE International*, no. doi:10.4271/2020-01-0811, 2020.

[96] R. Mitchell and D. Olsen, "Extending substitution limits of a diesel-natural gas dual fuel engine," *J Energy Resour. Technol*, no. doi:10.1115/1.4038625, 2018.

[97] S. Pasunurthi, R. Jupudi, S. Wijeyakulasuriya and S. Gubba, "Cycle to cycle variation study in a dual fuel operated engine," *SAE International* , no. doi:10.4271/2017-01-0772, 2017.

[98] F. Koningsson, J. Kuyper, P. Stalhammer and H. Angstrom, "The influence of crevices on hydrocarbon emissions from a diesel-methane dual fuel engine," *SAE International*, no. doi:10.4271/2013-01-0848, 2013.

[99] T. Donateo, L. Strafella and D. Laforgia, "Effect of the shape of the combustion chamber on dual fuel combustion," *SAE International*, no. doi:10.4271/2013-24-0115, 2013.

[100] M. Kassa, C. Hall, A. Ickes and T. Wallner, "Cylinder-to-cylinder variations in power production in a dual fuel internal combustion engine leveraging late intake valve closings," *SAE International*, no. doi:10.4271/2016-01-0776, 2016.

[101] K. Takizawa, H. Tanaka, N. Horibe, T. Ishiyama and T. Sako, "Effects of piston bowl diameter on combustion characteristics of a natural gas/diesel dual fuel engine," no. doi:10.4271/2019-01-2173, 2019.

[102] D. Kozorac, M. Bozic, A. Vucetic, J. Krajnovik and M. Sjeric, "Experimental and numerical analysis of a dual fuel operation of turbocharged engine at mid-high load," *SAE International,* no. doi:10.4271/2019-24-0122, 2019.

[103] P. Napolitano, C. Guido, C. Beatrice and N. Giacomo, "Application of a dual fuel diesel-CNG configuration in a Euro 5 automotive diesel engine," *SAE International,* no. doi:10.4271/2017-01-0769, 2017.

[104] B. Yang, L. Ning, B. Liu, G. Huang, Y. Cui and K. Zeng, "Comparison study the particulate matter characteristics in a diesel/natural gas dual-fuel engine under different natural gas-air mixing operation conditions," *Fuel,* no. doi:10.1016/j.fuel.2020.119721, 2020.

[105] C. Ma, E.-Z. Song, C. Yao, Y. Long, S. Ding and D. Xu, "Analysis of PCCI mode and multi-objective comprehensive optimization for a dual-fuel engine," *Fuel,* no. doi:10.1016/j.fuel.2021.121296, 2021.

[106] K. Wannatong, T. Tepimonrat and S. Kongviwattanakul, "Cylinder selective combustion, the new diesel dual fuel combustion control concept for low load operating conditions," *SAE International,* no. doi:10.4271/2018-01-1733, 2018.

[107] T. Lind, Z. Li, C. Mico, N. Olofsson, P. Bengtsson, M. Richter and O. Andersson, "Simultaneous PLIF imaging of OH and PLII imaging of soot for studying the late-cycle soot oxidation in an optical heavy-duty diesel engine," *SAE International,* no. doi:10.4271/2016-01-0723, 2016.

[108] E. Mancaruso, M. Todino and B. Vaglieco, "Analysis of dual fuel combustion in single cylinder research engine fueled with methane and diesel by IR diagnostics," *SAE International,* no. doi:10.4271/2019-01-1165, 2019.

[109] Q. Cheng, Z. Ahmad, O. Kaario and M. Larmi, "Simultaneous visualization of natural luminosity and chemiluminescense of dual fuel combustion in an optically accessible engine," *SAE International,* no. doi:10.4271/2020-01-0309, 2020.

[110] F. Unfug, "Investigation on dual fuel engine gas combustion using tomographic in-cylinder measurement technique and simultaneous high speed chemoluminescence visualization," *SAE International,* no. doi:10.4271/2016-01-2308, 2016.

[111] C. Mueller and G. Martin, "Effects of oxygenated compounds on combustion and soot evolution in a DI diesel engine: Broadband natural luminosity imaging," *SAE,* vol. 4, no. 111, pp. 518-537, 2002.

[112] J. Dernotte, J. Dec and C. Ji, "Investigation of the sources of combustion noise in HCCI engines," *SAE International,* vol. 7, no. 2, pp. 730-761, 2014.

[113] "Technical data for Alicat M-Series mass flow meters," Alicat Scientific , 2019. [Online]. Available: https://documents.alicat.com/specifications/Alicat_Mass_Meter_Specs.pdf.

[114] Photron, "Photron Fastcam SA5," 7 Oct 2019. [Online]. Available: https://photron.com/fastcam-SA5.

[115] H. Pitsch, "Laminar premixed flames: Kinematics and burning velocity," CEFRC Combustion Summer School, Princeton, 2014.

[116] "Fuel quality calculator," Cummins Westport , [Online]. Available: https://www.cumminswestport.com/fuel-quality-calculator. [Accessed 19 June 2021].

[117] G. Smith, D. Golden, M. Frenklach, N. Moriarty, B. Eiteneer, M. Goldenberg, T. Bowman and R. Hanson, "GRI-Mech 3.0," Berkeley, [Online]. Available: http://combustion.berkeley.edu/gri-mech/version30/text30.html#cite. [Accessed 8 January 2022].

[118] J. Deere, "PowerTech PWL 4045HFC04 diesel engine," 2016. [Online]. Available: https://jdauth.deere.com/en_US/docs/engines_and_drivetrain/specsheet/IND/4045HFC04_PWL.pdf. [Accessed 16 June 2021].

[119] C. Hall and M. Kassa, "Advances in combustion control for natural gas-diesel dual fuel compression ignition engines in automotive applications: A review," *Renewable and Sustainable Energy Reviews,* no. doi:10.1016/j.rser.2021.111291, 2021.

[120] J. Liu and C. Dumitrescu, "Lean-burn characteristcs of a heavy-duty diesel engine retrofitted to natural-gas spark ignition," *J. Eng Gas Turbines Power,* vol. 071013, no. doi.10.1115/1.4042501, p. 141(7), 2019.

[121] C. Ulishney, J. Liu, C. Dumitrescu and A. Sivri, "Effect of bowl-in-piston chamber on the combustion process in a stoichiometric natural-gas spark-ignition engine," in *International Conference on Applied Energy*, Vasteras, Sweeden, 2019.

[122] J. Liu, C. Ulishney and C. Dumitrescu, "Characterizing two-stage combustion process in a natural gas spark ignition engine based on mulit-Weibe function model," *Journal of Energy Resources Technology,* vol. 142(10), no. doi.10.1115/1.4046793, p. 102302, 2020.

[123] M. Choi, K. Mohiuddin and S. Park, "Effects of methane ratio on MPDF (micro-pilot dual-fuel) combustion characteristics in a heavy-duty single cylinder engine," *Sci Rep,* vol. 11, no. 9740, 2021.

[124] "Adiabatic flame temperatures," Engineering Toolbox, 2005. [Online]. Available: https://www.engineeringtoolbox.com/adiabatic-flame-temperature-d_996.html. [Accessed 27 February 2023].

[125] "Prompt NOx, fuel NOx and thermal NOx: The DLE strategy," Turbomachinery International, 24 February 2020. [Online]. Available: https://www.turbomachinerymag.com/view/prompt-nox-fuel-nox-and-thermal-nox-the-dle-strategy. [Accessed 26 July 2023].

[126] C. Lee, Y. Pang, H. Wu, K. Nithyanandan and F. Liu, "An optical investigation of substitution rates on natural gas/diesel dual-fuel combustion in a diesel engine," *Applied Energy,* vol. 261, 2020.

[127] J. Liu and C. Dumitrescu, "CFD simulation of metal and optical configuration of a heavy-duty CI engine converted to SI natural gas. Part 2: In-cylinder flow and emissions," *SAE International,* no. doi:10.4271/2019-01-0003, 2019.

[128] J. Liu, C. Ulishney and C. Dumitrescu, "Experimental investigation of a heavy-duty natural gas engine performance operated at stoichiometric and lean operations," *Energy Conversion and Management,* no. 243, 2021.

[129] M. Musculus, T. Lachaux, L. Pickett and C. Idicheria, "End-of-injection over-mixing and unburned hydrocarbon emissions in low-temperature-combustion diesel engines," *SAE International,* 2007.

8 Appendix A

Table 9- Metal Engine Sensor Details

Measurement Parameter	Sensor Type	Range	Accuracy('+/-')	Uncertainty (max)
Load	Lebow Load Cell	1000 lb	0.25%	2.5 lb
Speed	Bei XH25D-SS-1800	0-12,000 RPM, 1800 bits/rev	0.06%	0.2 CAD
C1 Flow	AliCat MCP-100 SLPM	0-100 slpm	0.8% reading +/-0.2% Full Scale	1 slpm
C2 Flow	AliCat MC-5 SLPM	0-5 slpm	0.8% reading +/-0.2% Full Scale	0.05 slpm
C3 Flow	AliCat MC-5 SLPM	0-5 slpm	0.8% reading +/-0.2% Full Scale	0.05 slpm
C4 Flow	AliCat MC-5 SLPM	0-5 slpm	0.8% reading +/-0.2% Full Scale	0.05 slpm
C5 Flow	AliCat MC-5 SLPM	0-5 slpm	0.8% reading +/-0.2% Full Scale	0.05 slpm
Diesel Mass	Brecknell MBS-6000	0-6000 grams	0.02%	1 gram
Intake Air Flow	Meriam 4 inch LFE	0-400 SCFM	0.64%	2.56 SCFM
Intake Pressure (slow, LFE)	Omega PX277-05D5V	0-5 inch WC	1.00%	0.05 inch WC
Intake Pressure (fast, Pegging)	Kulite HEM-375-100A	0-100 PSIA	0.50%	0.5 PSIA
Exhaust Pressure (fast)	Kulite EWCTV-312M-100A	0-100 PSIA	0.50%	0.5 PSIA
Cylinder Pressure (fast)	Kistler 6056A	0-250 bar	0.20%	0.5 bar
Diesel Injection Pressure	OEM SCV pump	setpoint 1000 bar	+50/-10 bar'	6%

Table 9 above details the main laboratory equipment used for metal engine experiments along with the associated accuracy and uncertainty. The flow controller and flow meters were purchased to be used near the mid-range of the design flow to minimize the flow uncertainty. Table 10 below lists the equipment used for optical engine experiments. Some of the sensors, such as the encoder, were used on both experimental setups. The optical engine relied upon proprietary OEM diesel injector data to determine the mass of diesel per injection at the 500 bar injection pressure setpoint. Unlike the metal engine, the air flow for the optical engine was measured with a critical flow venturi which provides a higher degree of accuracy.

Table 10- Optical Engine Sensor Details

Measurement Parameter	Sensor Type	Range	Accuracy	Uncertainty (max)
Speed	Bei XH25D-SS-1800	0-12,000 RPM, 1800 bits/rev	± 0.06%	0.2 CAD
Gas Flow (C_1-C_3)	AliCat MC-5 SLPM	0-5 slpm	0.8% reading ± 0.2% Full Scale	0.05 slpm
Diesel Mass	OEM proprietary look-up table	0-130 mg/inj	NA	NA
Intake Air Flow	Flow Systems Inc, Critical Flow Venturi, d=0.167 inch	2.3 g/s	± 0.32%	0.01 g/s
Critical Flow Venturi Pressure	Omega PX277-05D5V	0-7 bar	< ± 0.5% BFSL	0.03 bar
Intake Pressure (fast, Pegging)	Kulite HEM-375-100A	0-100 psia	± 0.50%	0.5 psia
Exhaust Pressure (fast)	Kulite EWCTV-312M-100A	0-100 psia	± 0.50%	0.5 psia
Cylinder Pressure (fast)	Kistler 6056A	0-250 bar	± 0.20%	0.5 bar
Diesel Injection Pressure	OEM SCV pump	setpoint 500 bar	± 5%	25 bar

Figure 72 shows an example of how the metal engine steady-state diesel fuel consumption rate was measured using the fuel scale listed in Table 9. The actual diesel fuel scale reading is shown in blue while the linear fit to the data is displayed in red. The experimental data used the rate determined by the linear fit for analysis purposes related to efficiency and fuel consumption. An automatic fuel scale refill pump was controlled by LabVIEW and a solid-state relay to refill the measurement tank in between data test points.

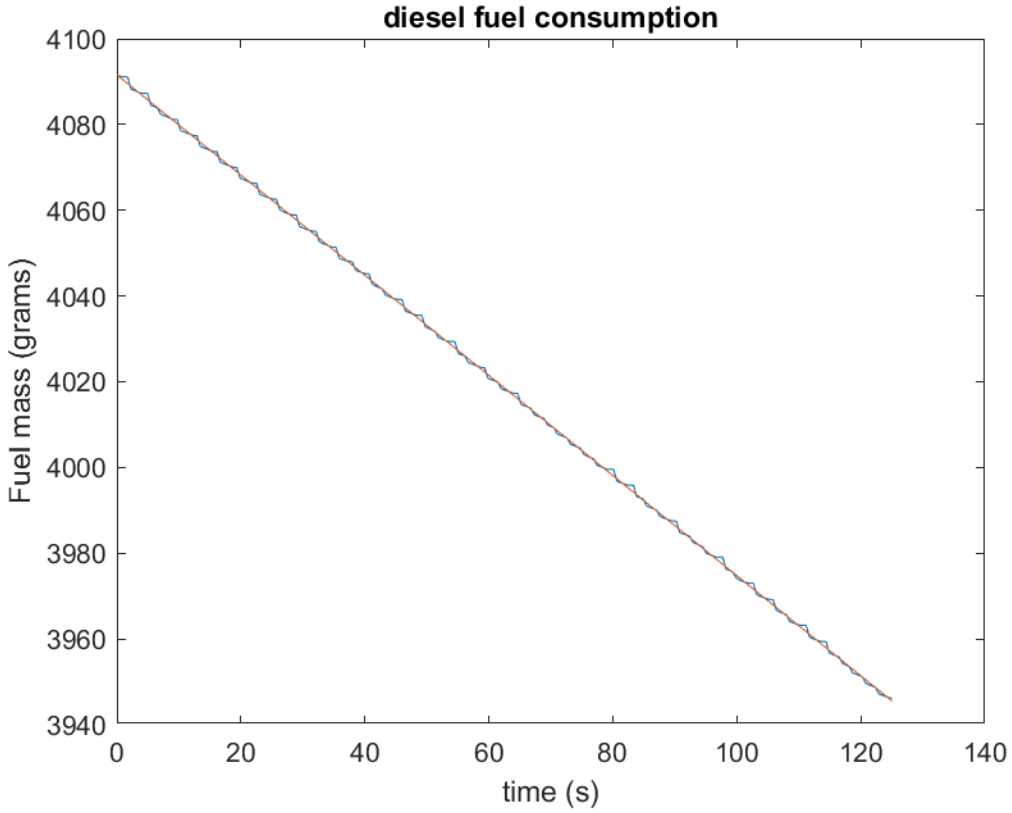

Figure 72- Example of Diesel Fuel Scale Interpolation for Fuel Consumption Rate

The LabVIEW code used to determine at equivalence ratio for burner experiments is shown in Figure 73. It took in the instantaneous gas flow rates as an input, performed a chemistry balance, and determined the current fuel composition AFR stoichiometric value. This value was then compared in the LabVIEW program to current air and gas flows in order to provide real-time equivalence ratios for the given fuel composition data points.

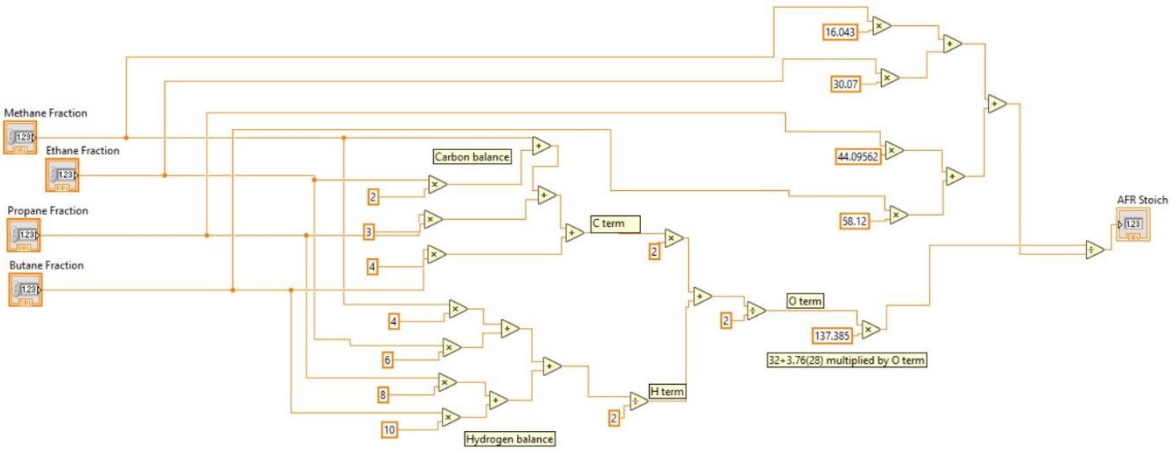

Figure 73- Chemical Balance for Fuel Mixture Stoichiometric Air-Fuel Ratio

The skip-fire control logic for optical engine experiments implemented in LabVIEW FPGA code is displayed in Figure 74. The counter toggled the injection enable command for the Drivven engine control program to allow for user interface control of the fired to non-fired cycle ratio. It also enables a shut-off of the firing command at a user input limit to total firing cycles in order to protect the optical engine components.

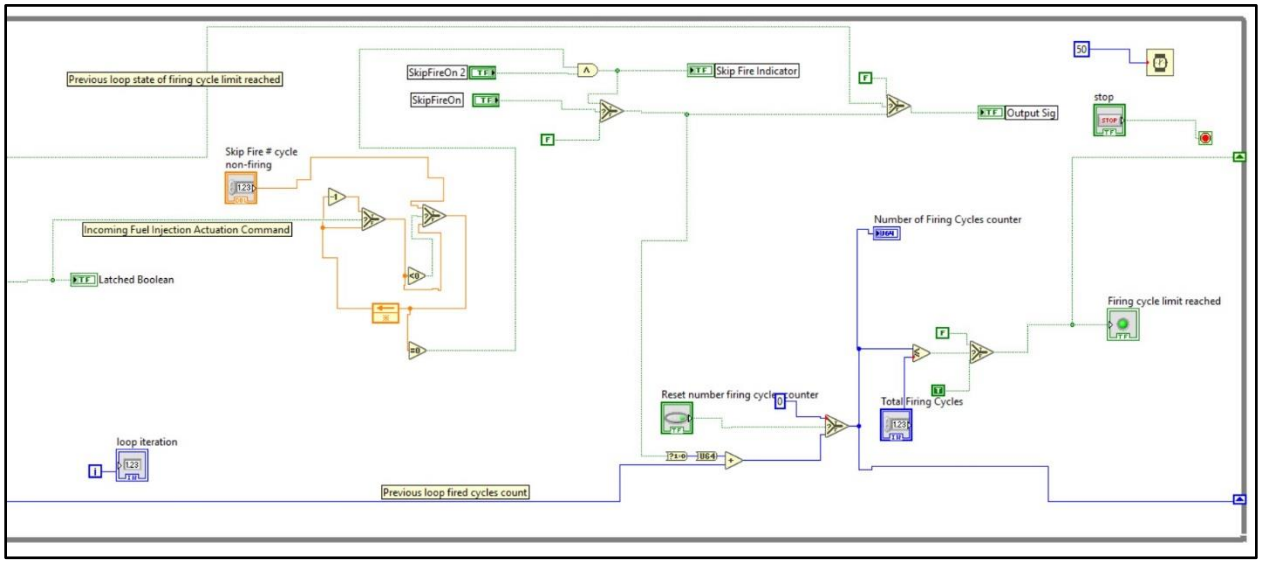

Figure 74- Skip-Fire Logic (LabView)